ULTRAFAST CARRIER DYNAMICS IN HIGHLY

EXCITED GAN EPILAYER, INGAN/GAN

DOUBLE HETEROSTRUCTURE, AND

INGAN/GAN MULTIPLE QUANTUM

WELL STRUCTURES

By

CHANKYUNG CHOI

Bachelor of Science
Seoul National University
Seoul, Republic of Korea
1990

Master of Science
Seoul National University
Seoul, Republic of Korea
1997

Submitted to the Faculty of the
Graduate College of the
Oklahoma State University
in partial fulfillment of
the requirements for
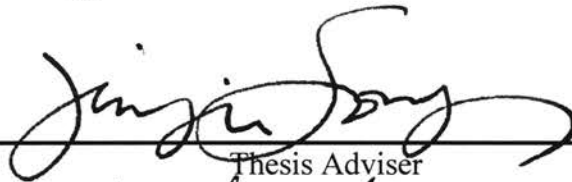the Degree of
DOCTOR OF PHILOSOPHY
August, 2001

ULTRAFAST CARRIER DYNAMICS IN HIGHLY

EXCITED GAN EPILAYER, INGAN/GAN

DOUBLE HETEROSTRUCTURE, AND

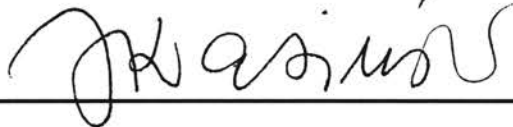INGAN/GAN MULTIPLE QUANTUM

WELL STRUCTURES

Thesis Approved:

Thesis Adviser

Dean of the Graduate College

ACKNOWLEDGEMENTS

TABLE OF CONTENTS

LIST OF FIGURES

CHAPTER I

INTRODUCTION

Optical spectroscopy is a powerful technique for investigating electronic and vibrational properties of a variety of system and it has provided extensive information and insights into the properties of atoms, molecules, and solids. In semiconductors, the techniques of absorption, reflection, luminescence, and light-scattering spectroscopies have provided invaluable information about such diverse aspects as the electronic band structure, phonons, coupled phonon-plasma modes, single-particle excitation spectra of electrons and holes, and properties of defects, surfaces, and interfaces. These are essential contributions to our understanding of semiconductors, but optical spectroscopy can do much more. Optical spectroscopy has additional unique strengths which make it capable of providing fundamental information about *nonequilibrium, nonlinear, and transport properties of semiconductors*. These strengths, which have been exploited since the 1960s and have been combined with the picosecond and femtosecond laser pulses to provide new insights into completely different aspects of semiconductors, can be classified into four groups: (1) photo-excitation generates excitations (electrons, holes, excitons, phonons, etc.) with non-equilibrium distribution functions, (2) optical spectroscopy provides the best means of determining the distribution functions of these excitations, and hence determining the dynamics of the relaxation of these excitations, (3) combined with spatial imaging and specially designed structures, optical spectroscopy provides the ability to investigate the transport of excitations and the dynamics of the transport in semiconductors and their nanostructures, and (4) optical techniques provide the ability to investigate the nonlinear properties including coherent effects in

semiconductors and thus provide insights into yet different aspects of semiconductors, such as many-body effects, coherent effects, and dephasing phenomena.

This chapter provides basic concepts in the interpretation of data obtained by ultrafast spectroscopy to be discussed in chapters III-VI.

Pump-probe spectroscopy

The dynamics in a pump-probe transmission experiment is determined by coherent and incoherent response of the system. If the time scale is comparable to or shorter than the interband polarization dephasing times of the system, one must use the semiconductor Bloch equation (SBE) to calculate the third-order nonlinear polarization in the appropriate direction. As the four-wave mixing signal corresponds to the third-order polarization radiating in the diffracted direction, the pump-probe signal corresponds to the third-order polarization radiating in the probe direction. The pump-probe signal can be viewed as the diffraction of the pump beam in the probe direction ($q_d = q_1 + q_2 - q_1 = q_2$). However, if the time scale of the experiment is long compared to the dephasing times, it may be possible to achieve great simplification by ignoring the coherent effects, i.e., by ignoring the off-diagonal components of the density matrix and considering only the diagonal components corresponding to the population of various states.

The effects in this incoherent regime can be qualitatively divided into two general classes: the first class encompasses *many-body effects* which result, for example, in a change of the energy band structure (e.g., band-gap renormalization or a change in the exciton binding energy), broadening of energy levels, or a change of the various matrix elements. The second class encompasses *phase-space filling effects*, or changes in the optical properties or transition rates caused by the nonequilibrium occupation of certain states (e.g., the interband absorption at a given photon energy is reduced if the final state is partially occupied by electrons). In general, these two effects are coupled because the many-body effects depend not only on the total density of the photoexcited carriers or excitons but also on their distribution functions.

The many-body effects depend strongly on the photoexcited density and the nature of the system being investigated (e.g., excitons vs. free carriers). For excitons, many-body effects, such as energy shifts, broadening, and bleaching induced by screening and phase-space filling, dominate even at moderate densities. For free carriers, on the other hand, other effects, such as band-gap renormalization and changes in the optical matrix elements, become important only at relatively high excitation density. If the density is high enough, both the many-body effects and the occupation effects must be considered.

Under certain experimental conditions, it may be a good approximation to assume that the many-body effects depend only on the photo-excitation density and are independent of time for the time scale of interest. Furthermore, for certain spectral regions, the change in the matrix elements for interband transitions may be small enough to be neglected. Under these conditions, the analysis of experiments is considerably simplified. If $f_e(E_e)$ and $f_h(E_h)$ are the photoexcited electron and hole distribution functions at energies E_e and E_h coupled by a photon of energy hv, then the change in the absorption coefficient at photon energy hv is given by

$$\Delta\alpha(hv) = [1 - f_e(E_e) - f_h(E_h)]\, \alpha_0(hv),$$

where $\alpha_0(hv)$ is the absorption coefficient of the unexcited semiconductor at $hv = E_e + E_h$. This is valid in a direct-gap semiconductor such as GaAs for free carriers with kinetic energies larger than the plasma frequency where $\alpha_0(hv)$ does not change significantly with photo-excitation. For sufficiently small $\Delta\alpha(hv)d$, where d is the thickness of sample over which the change in absorption is induced,

$$\mathrm{DTS}(hv) = [T(hv) - T_0(hv)]/T_0(hv) = \Delta\alpha(hv)d,$$

where T and T_0 are the transmitted intensities at hv with and without photo-excitation respectively, and DTS is the differential transmission spectrum. With these simplifications, the results can simply be related to the distribution of functions of electrons and holes as a function of time. It should be emphasized that the full complexity of the SBE and distribution function-dependent many-body effects must be considered in the general case, and the conditions for the validity of the simplified approach must be carefully scrutinized before applying it to a specific experiment.

Spectral properties of an electron-hole plasma due to intraband

Coulomb scattering

A. Screening

The most important physical effects in a plasma are the screening of the Coulomb potential $V_s(\mathbf{q}, \omega)=V_q/\epsilon(\mathbf{q}, \omega)$, where V_q is the unscreened Coulomb potential and $\epsilon(\mathbf{q}, \omega)$ is the longitudinal dielectric function, and the development of a collective plasma mode with the frequency ω_{pl}. Within the random-phase approximation (RPA) the density-dependent function is given by the Lindhard formula

$$\epsilon(\mathbf{q}, \omega)= 1-[V_q/V] \sum_{i=e,h;\mathbf{k}} \frac{f_{i,\mathbf{k}} - f_{i,\mathbf{k}+\mathbf{q}}}{\hbar\omega + \iota\delta - \varepsilon_{i,\mathbf{k}+\mathbf{q}} + \varepsilon_{i,\mathbf{k}}},\tag{1}$$

$\varepsilon_{i,\mathbf{k}}$ and $f_{i,\mathbf{k}}$ are the e and h energies and distribution functions, respectively. Note that the summation over the spin states is included in the $\mathbf{k}$ summation. If electrons and holes are within their band in a quasithermal equilibrium, their distribution functions are given by the Fermi distribution

$$f_{i,\mathbf{k}}= 1/[\exp\{(\varepsilon_{i,\mathbf{k}}-\mu_i)/k_BT\}+1],$$

where μ_i is the corresponding quasichemical potential.

Since, in general, Eq. (1) can only be evaluated numerically, one obtains a considerable simplification if one replaces the multiples in Eq. (1) by a single effective plasmon pole. If one further disregards the dynamical aspect of screening contained in the frequency dependence of Eq. (1), one obtains the much simpler static plasmon-pole approximation,[1,2] which will be used throughout this chapter,

$$[\epsilon(\omega)]^{-1}= [1-(\omega_{pl}^2/\omega_q^2)],\tag{2}$$

where ω_q is the dispersion of the effective plasmon mode.

1. 3D plasmon-pole approximation

In a three-dimensional (3D) semiconductor material one has

$$V_q = 4\pi e^2/\epsilon_0 q^2 \qquad (3\text{-}1)$$

$$\omega_{pl}^2 = 4\pi e^2 n/\epsilon_0 m = 16\pi n a_0^3 [E_0/\hbar]^2 \qquad (3\text{-}2)$$

$$\omega_q^2 = \omega_{pl}^2 [1+(q^2/\kappa^2)] + (C/4)[\hbar q^2/2m]^2 \qquad (3\text{-}3)$$

where m is the reduced e-h mass $m_e m_h/(m_e+m_h)$, n is the plasma density, and C is a numerical constant. The last form of ω_{pl}^2 expresses the plasma frequency in terms of the exciton Bohr radius a_0 and the exciton Rydberg constant $E_0 = e^2/2\epsilon_0 a_0 = \hbar^2/2ma_0^2$. In an e-h plasma these units are the natural length and energy scales, respectively. The inverse screening length

$$\kappa^2 = [4\pi e^2/\epsilon_0] \sum_i \frac{\partial n}{\partial \mu_i}. \qquad (4)$$

The limiting cases of the Debye and Thomas-Fermi screening can easily be obtained from Eq. (4). Putting the numerical constant $C = 0$ would result in a simple Yukawa potential $V_s(q) = 4\pi e^2/\epsilon_0(q^2+\kappa^2)$. With finite C, ω_q reaches asymptotically the free-carrier dispersion. This q^4 terms is important in order to get good agreement with the RPA screening, Eq. (1).

An additional simplification is reached if one uses an expansion for the chemical potential $\mu_i(n)$, which is obtained[3] by a re-summation of the expansion of n in power of $\exp[\mu_i/k_B T]$,

$$\mu_i(n) = k_B T [\ln(x_i n a_0^3) + (1/2^{3/2})(x_i n a_0^3) + \{(3/16)-(1/2^{3/2})\}(x_i n a_0^3)^2 + \cdots], \quad (5)$$

where $x_i = 4[\pi(m/m_i)(E_0/k_B T)]^{3/2}$.

2. 2D plasmon pole approximation

In quantum wells in which the width is smaller than the exciton Bohr radius, the translation motion perpendicular to the well is quantized. If one can limit oneself to the lowest subband, the system is called quasi-two-dimensional (2D). In this case the physical parameters of the plasmon-pole are given by[2]

$$V_q = 2\pi e^2/\epsilon_0 q \qquad (6\text{-}1)$$

$$\omega_{pl}^2 = 2\pi e^2 nq/\epsilon_0 m = 8\pi n a_0^2 q [E_0/\hbar]^2 \qquad (6\text{-}2)$$

$$\omega_q^2 = \omega_{pl}^2 [1+(q/\kappa)] + (C/4)[\hbar q^2/2m]^2 \qquad (6\text{-}3)$$

and

$$\kappa^2 = [4\pi e^2/\epsilon_0] \sum_i \frac{\partial n}{\partial \mu_i} . \tag{7}$$

In Eqs. (6) and (7), n is the 2D plasma density. In two dimensions, one can analytically compute the density dependence of the chemical potential from the expression

$$n = V^{-1} \Sigma_{\mathbf{k}} f_{i,\mathbf{k}}. \tag{8}$$

The result is

$$\mu_i(n) = k_B T \{\ln[\exp(y_i n a_0{}^2) - 1]\}, \tag{9}$$

where $y_i = 2[\pi(m/m_i)(E_0/k_B T)]$.

B. Band-gap renormalization

The band gap shrinks with increasing plasma density because of the changes of the single-particle energies due to the presence of a plasma. The band-gap shift is given by[2,4]

$$\Delta E_g = [V_s(\mathbf{r} = 0) - V(\mathbf{r} = 0)] - V^{-1} \Sigma_{\mathbf{q}} V_s(\mathbf{q}) (f_{e,\mathbf{q}} + f_{h,\mathbf{q}})$$

$$= \Delta E_{gCH} + \Delta E_{gSX}. \tag{10}$$

The first contribution is the difference of the self-interaction of a particle with and without the presence of the plasma. Naturally, the two terms are both divergent, but the difference yields a finite reduction of the energy gap due to the self-avoiding correlation between equally charged particles. Therefore this term is called the Coulomb hole (CH) contribution to the band-gap reduction. The remaining term is the screened exchange (SX) self-energy, which also reduces the band gap. Given the screened Coulomb potentials (3) and (4) in 3D and (6) and (7) in 2D, one can calculate ΔE_{gCH} by taking into account that $V(\mathbf{r} = 0) = \Sigma_q V_q$.

One obtains in 3D the Coulomb hole contribution as

$$\Delta E_{gCH} = -\frac{2E_0 a_0 \kappa}{\left[1 + C^{1/2}\left[\frac{E_0}{\hbar\omega_{pl}}\right](a_0\kappa)^2\right]^{1/2}} . \tag{11}$$

In 2D one gets, approximately,

$$\Delta E_{g\,\mathrm{CH}} = -2E_0 a_0 \kappa \ln\left[1 + \left[\frac{32 E_0 n a_0^2}{C(a_0 \kappa)^3}\right]^{1/2}\right]. \tag{12}$$

The screened exchange term has to be integrated numerically.

In this laser theory, the renormalized single-particle energies $\varepsilon_{i,\mathbf{k}} = e_{i,\mathbf{k}} + \Sigma_i$, with $\Sigma_k = (1/2)\Delta E_{g\mathrm{CH}} + \Delta E_{g\mathrm{SX}}$, will also appear in the Fermi functions together with the renormalized quasichemical potential

$$f_{i,\mathbf{k}} = 1/[\exp\{(e_{i,\mathbf{k}} + \Sigma_i - [\mu_i + \Sigma_i])/k_\mathrm{B}T\} + 1] = 1/[\exp\{(e_{i,\mathbf{k}} - \mu_i)/k_\mathrm{B}T\} + 1],$$

expressing the fact that a change of the band gap does not change the number of electrons or holes in the conduction and valence band, respectively.

Furthermore, the renormalized e-h energies appears as the sum in the interband-polarization or the related susceptibility

$$\varepsilon_{e,\mathbf{k}} + \varepsilon_{h,\mathbf{k}} = e_{e,\mathbf{k}} + \Sigma_e + e_{h,\mathbf{k}} + \Sigma_h + E_\mathrm{g} = e_{e,\mathbf{k}} + e_{h,\mathbf{k}} + E'_\mathrm{g}.$$

Intraband scattering by polar optical phonons

Optical phonons in semiconductors typically have energies of the order of tens of meV. Hence at low temperature ($T < 100$ K) most electrons do not have sufficient energy to emit optical phonons. In addition, the thermal occupation number N_q of optical phonons is very low, and consequently the probability of an electron absorbing an optical phonon is also small. Thus, optical phonon scattering processes are negligible at low temperatures. On the other hand, at room temperature, where there are sufficient high-energy electrons to emit optical phonons, they tend to dominate over acoustic phonon scattering. This is particularly true in polar semiconductors, where the Fröhlich electron-phonon interaction can be very strong. The distribution of final electronic states after optical phonon scattering is shown schematically in Figure 1(a). While scattering by acoustic phonons relaxes mainly the electron momentum, scattering by optical phonons contributes to both momentum and energy relaxation.

7
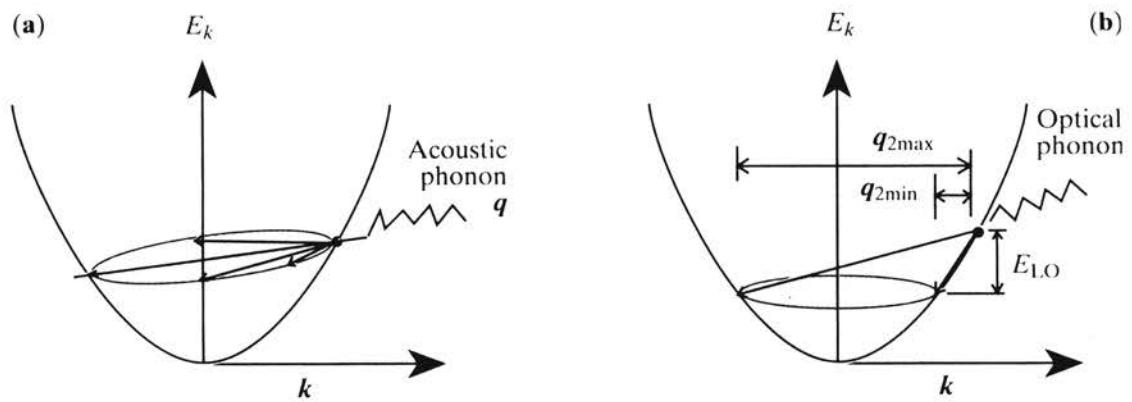
Figure 1. Schematic diagram for the scattering of an electron in a parabolic by emission of (a) an acoustic phonon and (b) a longitudinal phonon showing the final electronic states and also the range of phonon wave vectors allowed by wave vector conservation. Adapted from Ref. 5.

The longitudinal optical (LO) phonon scattering probability (P_{LO}) can be shown to be

$$P_{LO} \propto \int \left(\frac{q^2}{(q^2 + q_0{}^2)} \right) q^2 dq \int d(\cos\Theta) \{ N_{LO} \delta[E_{k'} - (E_k + E_{LO})]$$

$$+ (N_{LO} + 1)\delta[E_{k'} - (E_k - E_{LO})] \} \qquad (13)$$

where N_{LO} and E_{LO} are, respectively, the LO phonon occupation number and energy. For simplicity we assumed that the LO phonon is dispersionless, which is usually a good approximation since only phonons with $q \leq q_0$ contribute significantly to Eq. (13). The term inside the first set of parentheses comes from the Fröhlich matrix element, including screening. The terms proportional to N_{LO} and $N_{LO}+1$ are identical with phonon absorption and emission, respectively. As a result of wavevector conservation, Eq. (13) can be expressed as

$$P_{LO} \propto \int \left(\frac{q^4}{(q^2 + q_0{}^2)} \right) dq \int d(\cos\Theta) \{ N_{LO} \delta[(\hbar^2 q / 2m)(k\cos\Theta + q) - E_{LO}]$$

$$+ (N_{LO} + 1)\delta[(\hbar^2 q / 2m)(-k\cos\Theta + q) + E_{LO})] \} \qquad (14)$$

Integrating over Θ results in the following expression for P_{LO}:

$$P_{LO} \propto N_{LO} \int_{q_{1\min}}^{q_{1\max}} \left(\frac{q^3}{(q^2 + q_0{}^2)^2} \right) dq + (N_{LO} + 1) \int_{q_{2\min}}^{q_{2\max}} \left(\frac{q^3}{(q^2 + q_0{}^2)^2} \right) dq, \qquad (15)$$

where $q_{i\max}$ and $q_{i\min}$ are, respectively, the maximum and minimum values of the LO phonon wavevector for phonon absorption ($i = 1$) and phonon emission ($i = 2$). From Figure 1(b), one can easily identify the electron final states corresponding to the minimum and maximum values of q. Since $q_{i\max}$ is nonzero for optical phonons, the screening wavevector in Eq. (15) is not as important as for piezoelectric acoustic phonons, except in the case of highly doped semiconductors. If we neglect q_0 in Eq. (15), P_{LO} decreases as $1/q$ and scattering by small-q LO phonons is more likely than by large-q LO phonons. In contrast to the case of acoustic phonon scattering, scattering between electrons and LO phonons tends to relax the electron energy rather than its momentum.

The momentum relaxation time of an electron due to LO phonon scattering can be deduced from Eq. (15) using $\langle d\mathbf{k} / dt \rangle = \mathbf{k}(\tau_m)^{-1} = \sum (\mathbf{k'} - \mathbf{k}) P(\mathbf{k}, \mathbf{k'})$. The result is

$$\left(\frac{1}{\tau_{\mathrm{m}}}\right) \propto N_{\mathrm{LO}}\left(\frac{E_k + E_{\mathrm{LO}}}{E_k}\right)^{1/2} + (N_{\mathrm{LO}} + 1)\left(\frac{E_k - E_{\mathrm{LO}}}{E_k}\right)^{1/2} + \left(\frac{E_{\mathrm{LO}}}{E_k}\right)\left\{-N_{\mathrm{LO}}\sinh^{-1}\left(\frac{E_{\mathrm{LO}}}{E_k}\right)^{1/2}\right.$$

$$\left. + (N_{\mathrm{LO}} + 1)\sinh^{-1}\left(\frac{E_k - E_{\mathrm{LO}}}{E_k}\right)^{1/2}\right\}.$$

CHAPTER II

GENERAL PROPERTIES OF THE GROUP III NITRIDES

Because several reviews of the optical properties of the group III nitrides exist in the literature (see, for example Refs. 6 and 7) where interested readers can readily find the a good synopsis of known optical properties, only those properties that are pertinent to the contents of this monograph will be given here. Since the technologically important nitride-based materials are InGaN (for blue light emitting devices) and AlGaN (for solar blind UV detectors) with moderate to low indium and aluminum concentrations, respectively, we will concentrate on the optical properties of the base material, GaN. This is also made necessary because of the large band tailing that results from the incorporation of Al and In into GaN to form AlGaN and InGaN, making the observation of fundamental optical transitions very difficult, even in state-of-the-art high quality crystals.

Crystal Properties

Like most semiconductor materials, the group III nitrides have a tetrahedrally coordinated atomic arrangement that typically results in either a hexagonal (wurtzite) or cubic (zincblende) crystal structure. In all, there are three common crystal structures shared by the group III nitrides: The wurtzite, zincblende, and rocksalt structures. The thermodynamically stable structure for bulk AlN, GaN, and InN at ambient conditions is wurtzite, although the zincblende structure has been stabilized by epitaxial growth of thin

films on the (011) crystal planes of cubic crystal substrates such as Si, MgO, and GaAs. The rocksalt structure can only be induced at very high pressures. Only the structural and optical properties of the wurtzite form of the group III nitrides will be considered in this monograph. The wurtzite crystal structure has a hexagonal unit cell, and therefore two lattice constants, designated as a and c. It contains six atoms of each type and consists of two interpenetrating hexagonal close packed sublattices (each with one type of atom), offset along the c axis by 5/8 of the cell height (5/8 c). The stacking sequence of the (0001) diatomic planes is BABAB in the <0001> direction. The space grouping of the wurtzite structure is P6$_3$mc (C_{6V}^4). The wurtzite crystal structure is given in Figure 2. In its wurtzite form, AlN has a molar mass of 20.495 gm/mol. Reported lattice parameters range from 0.3111 to 0.3113 nm for a, and from 0.4978 to 0.4982 nm for c. The AlN linear thermal expansion coefficient are $a_\perp = 5.27 \times 10^{-6}$ K^{-1} for $T = 20 - 800$ °C, and $a_\parallel = 4.15 \times 10^{-6}$ K^{-1}. The thermal conductivity of AlN is $k = 2$ W/[cm °C] at room temperature. The dielectric constants of AlN are $\epsilon(0) = 9.14$ and $\epsilon(\infty) = 4.84$ at 300 K. GaN has a molecular eight of 83.728 gm/mol and room temperature lattice parameters of $a_0 = 0.31892 \pm 0.00009$ nm and $c_0 = 0.51850 \pm 0.00005$ nm. The GaN linear thermal expansion coefficient is $a_\parallel = 4.15 \times 10^{-6}$ K^{-1} along the a-axis. The thermal conductivity of GaN is $k = 1.3$ W/[cm °C] at room temperature, nearly equal to that of Si and about three times that of GaAs. The dielectric constant of GaN has been measured to be in the range $\epsilon(0) = 8.9$ to 9.5 at room temperature, just below that of SiC. Values reported for InN are varied due to the absence of good quality single crystal films. InN has a molar mass of 128.827 gm/mol and the lattice parameters reported in the literature range from 0.3530 to 0.4980 nm for a_0, and from 0.5960 to 0.574 nm for c_0. For a complete review of the structural properties of the group III nitrides, see, for example, Ref. 6. GaN is by far the most extensively studied of the group III nitrides, but is still in need of extensive investigation if it is to reach the level of understanding and technological status of Si and GaAs, especially in nonequilibrium carrier dynamics.
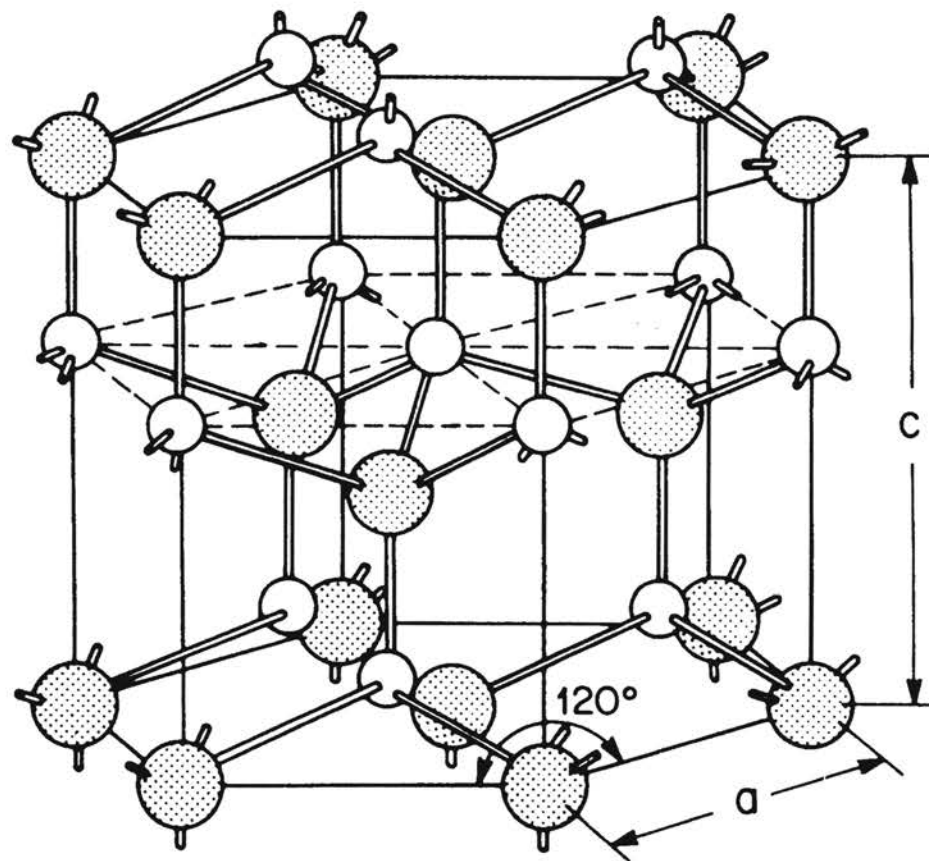
Figure 2. Schematic of the wurtzite crystal structure. Adapted from Ref. 8

Band structure

When GaN crystallizes in the wurtzite form, its conduction band minimum is located at the center of the Brillouin zone (Γ-point, $k = 0$) and has a Γ_7-symmetry with a quantum number $j_z = 1/2$. The valence band also has its maximum at the Γ-point, resulting in a direct fundamental band gap. The top of the valence band is split into three sub-bands as a result of crystal-field and spin-orbit coupling. These valence bands are conventionally referred to as the A, B, and C valence bands and are a direct result of GaN's wurtzite crystal structure. The A-band has Γ_9-symmetry, while the B and C bands have Γ_7-symmetry. Detailed reviews of the electronic band structure can be found in abundance in the literature. Because only the transitions associated with the lowest conduction band and uppermost valence bands in GaN near $k = 0$ are pertinent to this monograph, they are shown in detail in Figure 4. In GaN, each valence band generates a hydrogenic series of excitonic states. The free exciton states in GaN are adequately described by the Wannier-Mott approximation. Spontaneous emission in ternary compounds InGaN and AlGaN is dominated by recombination from band tail states, with the depth of band tailing dependent on the Al and In concentrations as well as the growth conditions. Because of this, we will concentrate in this section only on the optical properties of GaN. This allows us to gain a better understanding of the base material without the complications presented in the ternary compounds. The optical properties pf the ternary compounds will be introduced as needed later in the text with appropriate references.
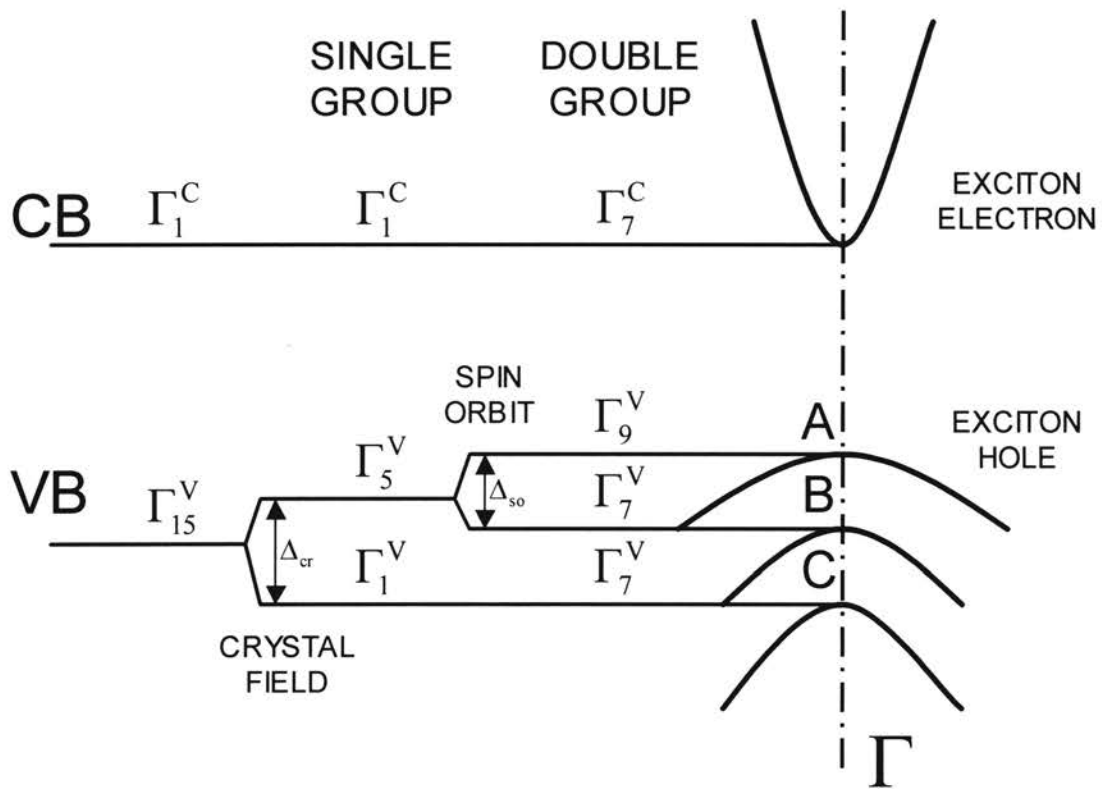
Figure 3. Structure and symmetries of the lowest conduction band and the uppermost valence bands in wurtzite GaN at the Γ point ($k \sim 0$). Adapted from Ref. 9.

CHAPTER III

ULTRAFAST CARRIER DYNAMICS IN GaN

Femtosecond pump-probe transmission spectroscopy was performed at 10 K to study the nonequilibrium carrier dynamics in a GaN thin film for carrier densities ranging from 4×10^{17} to 10^{19} cm^{-3}. Spectral hole burning was initially peaked roughly at the excitation energy for an estimated carrier density of 4×10^{18} cm^{-3} and gradually redshifted during the excitation. Because of hot phonon effects, a very slow energy relaxation of the hot carriers at these densities was observed. The hot carriers were strongly confined in a non-thermal distribution and they relaxed collectively to the band edge for about 1 ps. We also observed remarkable persistence of the excitonic resonances in GaN at carrier densities well above the Mott density at early time delays, indicating that the excitons do not strongly couple to the non-thermal electron-hole plasma.

Motivation

Developments in femtosecond laser technology have enabled fundamental studies of non-equilibrium, nonlinear, and transport properties of semiconductors.[10] Non-degenerate pump-probe (PP) spectroscopy is a powerful tool for studying the transient dynamics of hot carriers because it makes possible the observation of not only coherent phenomena occurring during excitation, but also the non-thermal carrier distribution reflecting the energy profile of the exciting pump pulse and its temporal evolution. Wurtzite GaN has a direct band gap of 3.50 eV at 10 K, a large exciton binding energy of

16

about 21 meV, and a large longitudinal optical (LO)-phonon energy of 92 meV. Also, GaN is mechanically and thermally robust and has a higher damage threshold making it a good candidate for investigating non-thermal carrier dynamics under strong excitation. There have been a few femtosecond PP spectroscopy reports on GaN.[11-13] However, there has been no direct experimental observation of the non-thermal carrier distributions during the pump-pulse duration and their relaxation.

We present a study of non-equilibrium carrier dynamics in a GaN epilayer photoexcited well above the bandgap using non-degenerate PP spectroscopy at 10 K with light pulses of a duration time of ~360 fs at excitation densities both above and below the Mott density (10^{18} cm^{-3} for GaN at 10 K).[14] We found that the photoexcited hot carriers are strongly confined in a non-thermal distribution and their relaxation toward the band edge is very slow, partially because of the hot phonon effect. By investigating the change of absorption spectra at the exciton resonances while the non-thermal carriers relax, we were able to evaluate the relative importance of long-range Coulomb screening and Pauli blocking on the bleaching of exciton resonances.

Sample and experimental setup

The sample used in this study is a high quality 0.38 µm uncoated GaN epilayer grown by metalorganic chemical vapor deposition (MOCVD) on (0001) sapphire. An excitonic resonance was clearly observed in this sample's absorption measurements above 300 K.[15] Femtosecond PP spectroscopy measurements were carried out using a 1 kHz regenerative amplifier (REGEN) to create 100 fs duration [full width at half maximum (FWHM)] pulses at a wavelength of 800 nm. These pulses were fed into an optical parametric amplifier to create pulses with a FWHM of 355 fs, measured by difference-frequency mixing in a BBO crystal, at 329 nm (3.766 eV) with a bandwidth of 22 meV. This beam was used as the pump source to excite carriers above the GaN bandgap. The leftover output from the REGEN was frequency doubled to 400 nm and then used to create a broad-band continuum probe source with a FWHM of 350 fs. The

pump and probe beams were orthogonally polarized, and the angle between them was 15°. Neutral density filters were used to attenuate the probe beam to a power sufficiently low so that it would not alter the optical properties of the sample. The probe beam was focused to a 150 μm diameter spot on the sample, and the transmitted light was collected and focused into a spectrometer with an attached charge coupled device (CCD) detector. The pump spot size was focused to 300 μm to minimize the variation in pump beam intensity across the probed region. The optical delay between the pump and probe was accurately controlled using a computerized step motor. All measurements were performed at 10 K.

Results and discussion

Differential transmission spectrum (DTS)[16] measures the difference between the probe transmission with and without the pump :

$$\text{DTS} = \Delta T / T_0 = (T - T_0)/T_0 = \exp\left(-\int_0^d \Delta\alpha(z)dz\right) - 1, \qquad (16)$$

where T, T_0, $\Delta\alpha(z)$, and d are the transmitted probe intensity with and without the pump, the pump-induced absorption change at depth z, and the sample thickness, respectively. Figure 4 shows the DTS at early time delays for a peak carrier density of (a) 1×10^{19} cm^{-3} and (b) 4×10^{18} cm^{-3}, respectively. The peak carrier densities are estimated based on theoretical modeling taking into account the band filling effect at zero time delay (see below). For the sample thickness of 0.38 μm with an absorption coefficient of 0.8×10^5 cm^{-1} at the excitation energy, this sample is optically thick, so the carrier density depends on the depth (z) from the sample surface, which leads to a depth-dependent absorption coefficient $\alpha(z)$. The pump spectrum is shown as a dashed line and centered at 3.766 eV (266 meV above the band gap of the excited GaN sample at 10 K). The inset in Figure 4(a) shows well resolved 1s A- and B- exciton resonances. The DTS value, which is larger than unity, does not indicate optical gain, but rather a large induced transparency by the strong laser excitation. Due to strong band filling effects, there is a large reduction

18

of about 10^4 cm^{-1} in absorption of the probe intensity. This makes T an order of magnitude larger than T_0, leading to a DTS value larger than one. We take the zero time delay to be at the approximate maximum of the pump pulse. For time delays of less than -200 fs , there were no significant band filling effects, which is characteristic of an unexcited sample. Coherent oscillation effects[17] around exciton resonances and in the vicinity of the excitation energy when the probe pulse precedes the pump were not observed in our experiment.

The DTS at a time delay of $t_d = -200$ fs shows a spectral hole burning[18] which is initially peaked roughly at the excitation energy. While the population of excited carriers increases during the pump duration (from -200 fs to 200 fs), the spectral hole burning shows fast broadening and distinct shifts of 47 meV [Figure 4(a)] and 38 meV [Figure 4(b)] toward the bandgap. The fast broadening of the non-equilibrium carrier distribution at this time scale is most likely caused by carrier-carrier scattering, such as electron-electron, electron-hole, and hole-hole collisions. Because the initial excess electron energy is about three times larger than the hole energy and because of the larger electron-to-hole effective mass ratio in GaN compared to GaAs, the transfer of energy to the colder hole system via electron-hole scattering could result in this fast broadening of the hole burning. The redshift of the spectral hole on this time scale of less than 200 fs cannot be ascribed to a relaxation of the carrier distribution through LO-phonon emission, because the redshift is much smaller than the LO-phonon energy of 92 meV, and the deformation-potential scattering is not strong enough to cause such a redshift at an early time delay. We neglect the carrier diffusion effect, because the diffusion constant for a GaN/AlGaN double heterostructure within 2 ps at 10 K was reported to be small.[19]
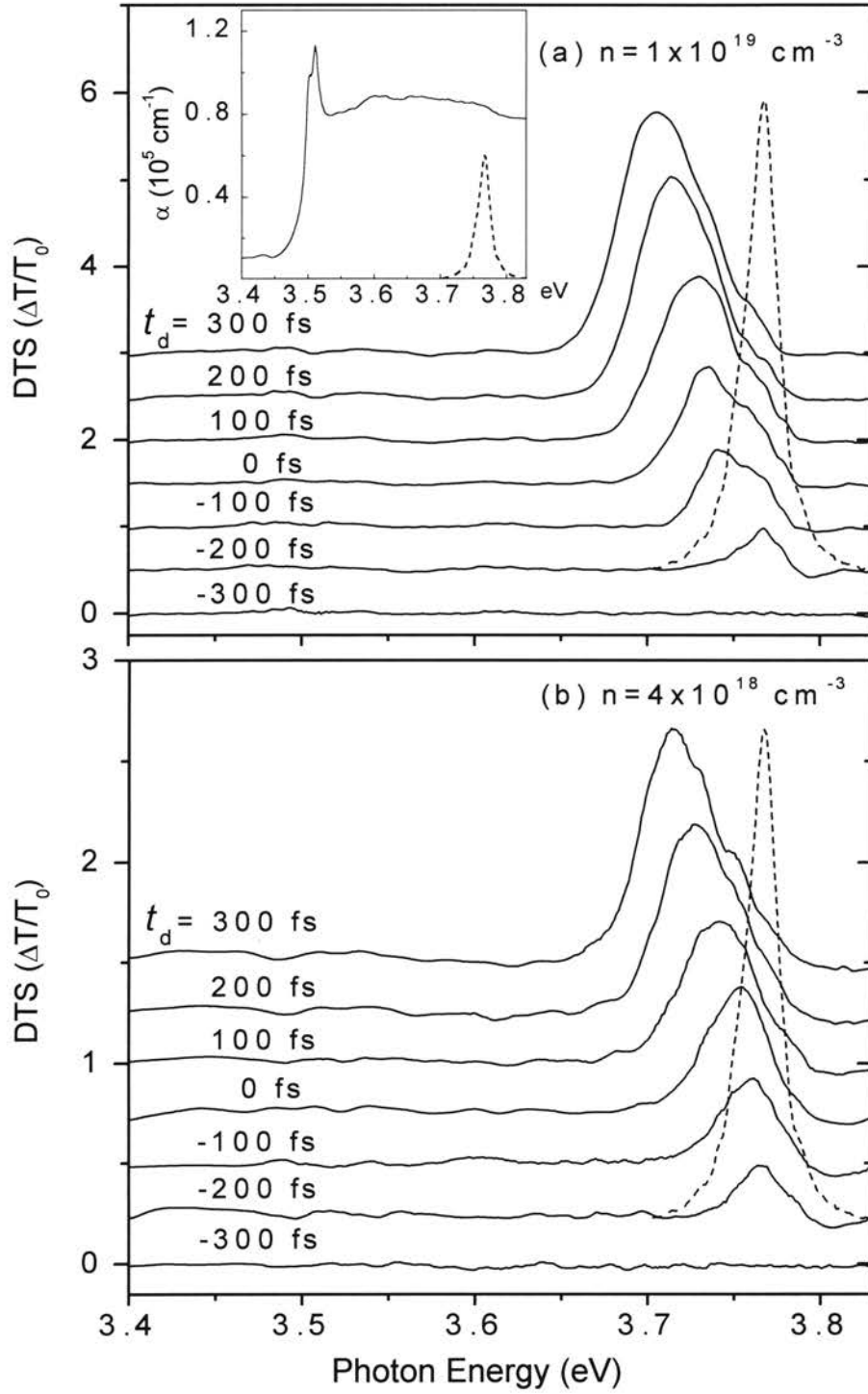
Figure 4. Differential transmission spectra (pump-induced transmission change $\Delta T/T_0$) in a 0.38 μm GaN/sapphire sample at 10 K for peak carrier densities of (a) 1×10^{19} cm^{-3} and (b) 4×10^{18} cm^{-3} showing ultrafast near-zero-delay dynamics. The dashed line shows the pump spectra. The DTS curves were displaced vertically for clarity. The inset in Figure 4(a) shows the absorption spectra for the sample at 10 K.

To investigate the carrier dynamics, we adopt a simplified model which takes into account the carrier-carrier scattering with static screening and various electron-phonon scattering processes. We have considered the electron-phonon scattering by both the Fröhlich and the deformation-potential mechanisms. We found that at a peak carrier density of n = 4×10^{18} cm^{-3}, for energies near the pumping energy, the carrier-carrier scattering rate is around 80 (460) ps^{-1} for electrons (holes), while the electron-LO phonon scattering rate is around 60 ps^{-1}. The hole-LO scattering rate is negligible, since the hole energies are smaller than the LO-phonon energy and therefore, no LO-phonon emission process is possible. At n = 1×10^{19} cm^{-3}, these rates change to 50 (300) ps^{-1} and 50 ps^{-1}, respectively. Thus, both mechanisms are important for the energy relaxation of carriers. The screening effect reduces both the carrier-carrier scattering and electron-LO phonon scattering, but not substantially. Without carrier screening, the electron-LO phonon scattering rate is around 80 ps^{-1}, which is consistent with the result reported in Ref. 20. Since the electron-LO phonon scattering rate is much higher than the decay rate of LO-phonons (around 0.2 ps^{-1})[21] even at the highest density considered here, we expect that a large number of non-equilibrium (hot) LO-phonons is generated during the carrier relaxation. It is well known that the presence of hot phonons substantially reduces the energy relaxation rate of electrons,[22-24] since the equivalent temperatures of the hot electrons and hot phonons are close to each other. Thus, it is not surprising that our electron energy relaxation is slow (around 100 meV/ps). In this study, we concentrate on the simulation of the PP spectra at early times during the carrier build up. For a time delay less than 100 fs, the carrier distribution remains peaked at the same position in momentum space, with a gradual broadening due to the carrier-carrier scattering.

The nonlinear transmission change cannot be readily interpreted in terms of band filling alone. The complex superposition of bandgap renormalization, band filling, and screening of the Coulomb interaction between correlated states (excitons) and uncorrelated electron-hole pairs must be taken into account.[25] We attribute the spectral hole redshift at early times to bandgap renormalization and exciton effects. A weak induced absorption at t_d = −200 fs in Figures 4(a) and 4(b) is seen just above the excitation energy. This could be due to Coulomb enhancement by exciton effects. The induced absorption disappears with increasing carrier density when electron-hole plasma

21

screening of the Coulomb potential overwhelms the attractive electron-hole interaction. There have been a few reports on induced absorption above the excitation energy for GaAs.[26,27] They attributed the induced absorption to many-body correlation from Coulomb interaction. In general, exciton effects result in a small redshift of the spectral hole to lower energies.[25-28] However, this effect alone does not explain our result, since the spectral hole moves toward the band edge during the pump duration, contrary to what is observed in GaAs.[26] We consider the momentum (k) dependence of the bandgap renormalization $\Delta E(k)$, taking into account the actual carrier distribution. The k-dependence of the bandgap renormalization is calculated first in the Hartree-Fock approximation and then with the addition of the Coulomb-hole effect.[29] We then have

$$\Delta E(k) = -\Sigma_q \, v_q \, f(k+q) \, / \, \epsilon(q) - \Sigma_q \, v_q \, (\epsilon(q)^{-1} - \epsilon_0^{-1}) \tag{17}$$

where $v_q = 4\pi e^2/q^2$, ϵ_0 is the low-frequency dielectric constant, $\epsilon(q)$ is the static dielectric function including the polarization due to free carriers, and $f(k)$ is the non-equilibrium carrier distribution function. The first term is the screened Hartree-Fock approximation and the second term is the Coulomb-hole correction. The dielectric screening in the static limit is approximately given by Lindhard's expression

$$\epsilon(q) = \epsilon_0 + 2V_q \sum_k \frac{f(k) - f(k+q)}{E(k+q) - E(k)}$$

$$= \epsilon_0 + \frac{2e^2 m^*}{\hbar^2 \pi q^3} \int \ln\left|\frac{q+2k}{q-2k}\right| f(k) \, k \, dk, \tag{18}$$

where, in the long-wavelength limit, we have

$$\epsilon(q) = \epsilon_0 \, (1 + q_0^2/q^2) \text{ with } q_0^2 = (2e^2 m^*/\hbar^2 \pi \epsilon_0) \int f(k) \, dk. \tag{19}$$

Note that q_0 reduces to the Thomas-Fermi wave vector in the degenerate limit when $f(k)$ becomes the Fermi distribution function at zero temperature.

We found that the non-equilibrium carrier distributions can be approximated by the Gaussian distribution

$$f_e(k) = A(z) \, [\exp\{-a(k^2 - k_1^2)^2\} + \exp\{-a(k^2 - k_2^2)^2\}], \tag{20}$$

$$f_{h1}(k) = A(z) \, [\exp\{-a(k^2 - k_1^2)^2\}], \tag{21}$$

$$f_{h2}(k) = A(z) \, [\exp\{-a(k^2 - k_2^2)^2\}], \tag{22}$$

where the subscripts e, h1, and h2 label the electrons, holes in the *A* band, and holes in the *B* band, respectively. The amplitude of the carrier distribution is assumed to be

22

proportional to the light intensity at depth z. Thus, we have the following form $A(z) = A_0 e^{-\alpha z}$, where α is the absorption coefficient at the pump energy. The peak carrier density which we used throughout this paper is given by $n = 2 \int f_e(k)dk/(2\pi)^3$ at a depth of $z = 0$. The centering positions k_1 and k_2 are determined by the relation

$$E_e(k_1) + E_{h1}(k_1) = E_e(k_2) + E_{h2}(k_2) = \hbar\omega, \qquad (23)$$

where $\hbar\omega$ is the absorbed photon energy. For illustration, we show in Figure 5 the k-dependent band renormalization for the A band transitions for a carrier density $n(z) = (4 \times 10^{18} \text{ cm}^{-3}) e^{-\alpha z}$ with the depth set at $z = d/4$.
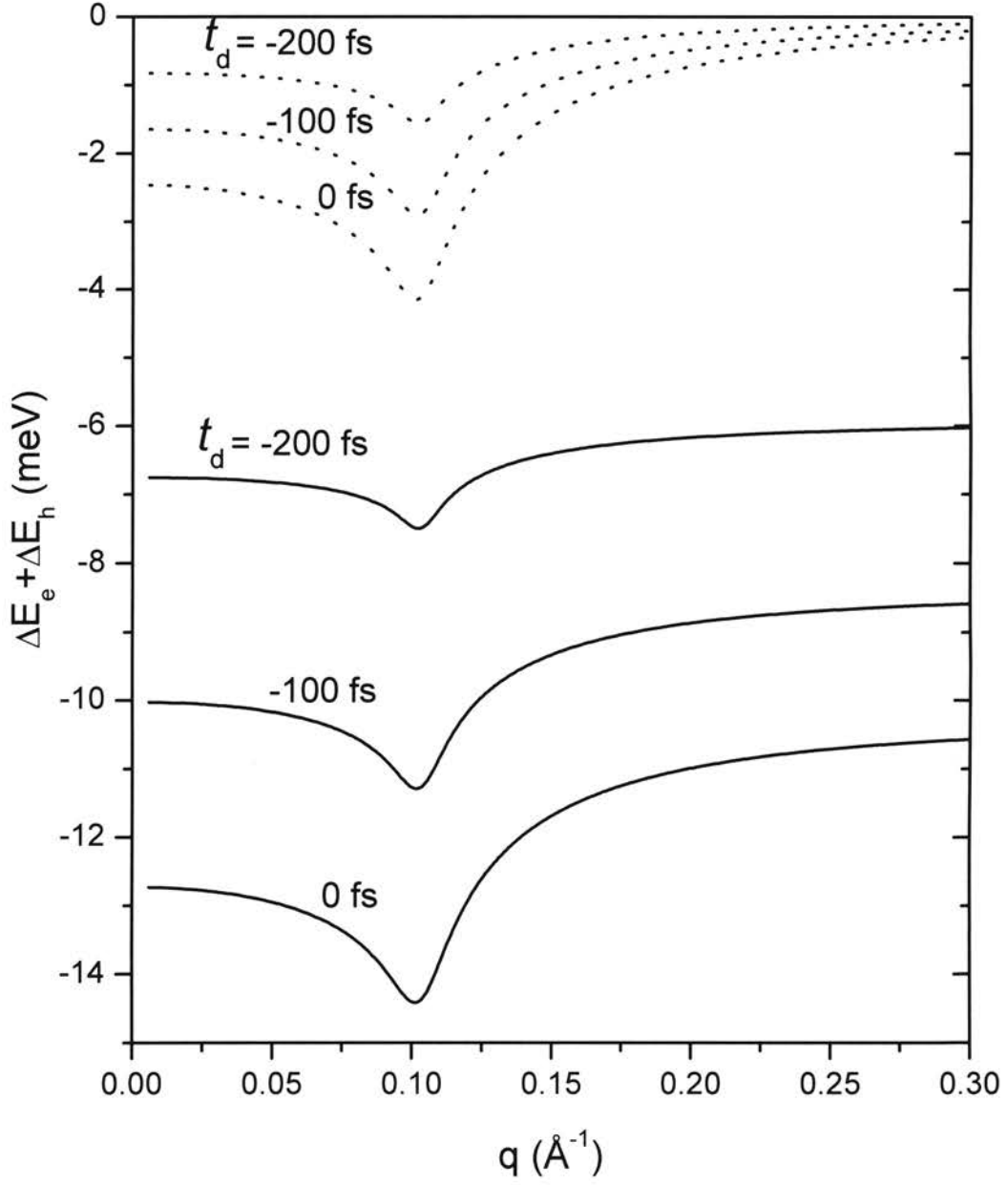
Figure 5. Calculated band renormalization for the *A* band transition due to non-equilibrium carrier distributions as a function of momentum at a depth $z = d/4$ for a peak carrier density of 4×10^{18} cm^{-3}, at time delays of $t_d = -200$, -100, and 0 fs. The dotted lines represent the screened Hartree-Fock approximation. The solid lines also include the Coulomb-hole correction.

The band renormalization for the *B* band transitions is quite similar to that of the *A* band transitions. Using the z-dependent band renormalization and non-equilibrium carrier distributions given above, we calculated the z-dependent absorption coefficient $\alpha(z)$ and DTS according to Eq. (16). The absorption coefficient for the *A*-band transitions, including phase-space filling and neglecting screening, is given by

$$\alpha(\hbar\omega) = (C/\hbar\omega) \left[\delta(\hbar\omega - E_g - E_X) + \delta(\hbar\omega - E_g - E_X/4)/8 \right.$$

$$\left. + \frac{2\pi^2 x}{1 - e^{-2x}} \Sigma_k (1 - f_e(k) - f_h(k)) \, \delta(\hbar\omega - E_e(k) - E_h(k) - \Delta E_e(k) - \Delta E_h(k)) \right] \quad (24)$$

where C is a constant, E_g is the energy gap between the renormalized valence band (*A* or *B* band) and the conduction band, E_X is the exciton binding energy, $x = [E_X/(\hbar\omega - E_g)]^{1/2}$. The z dependence for $f_e(k)$, $f_h(k)$, ΔE_e, ΔE_h, and α was kept implicit in the above equation. The absorption coefficient for the *B*-band transitions is given by the same expression, except that the band gap E_g is increased by the *A-B* splitting by spin-orbit interaction and the constant C is increased by 20% in order to reproduce the line-shape of the experimental spectrum near the exciton energy. Note that we included the contributions from the ground state, the first excited state, and the continuum states (with the phase-space filling effect). In our initial simulation, due to band renormalization, an appreciable DTS occurs near the exciton energy, in disagreement with our experiment. However, the DTS predicted near the pump energy is in reasonable agreement with experiment. This suggests that the band renormalization in the correlated exciton states is greatly suppressed due to the charge neutrality of the exciton. Since a full many-body theory is not available at the present, we introduce a phenomenological suppressing factor $\{1 - \exp[-(E_e(k) + E_h(k) - E_g)/4E_X]\}$. This factor greatly reduces the band renormalization for exciton continuum states with low energy, while the high energy states are unaffected. This is reasonable, since the high-energy exciton continuum states are much less correlated. With this correction, the final simulated absorption spectra averaged over the sample depth, $\left[\int_0^d \alpha(z)dz\right]/d$, and the DTS are shown in Figure 6, and are seen to be in reasonable agreement with experiment. For comparison, the DTS at $t_d =$

25

0 fs without including the correction factor is shown as the short-dotted curve, and is in poor agreement with experiment near the exciton transition energy.
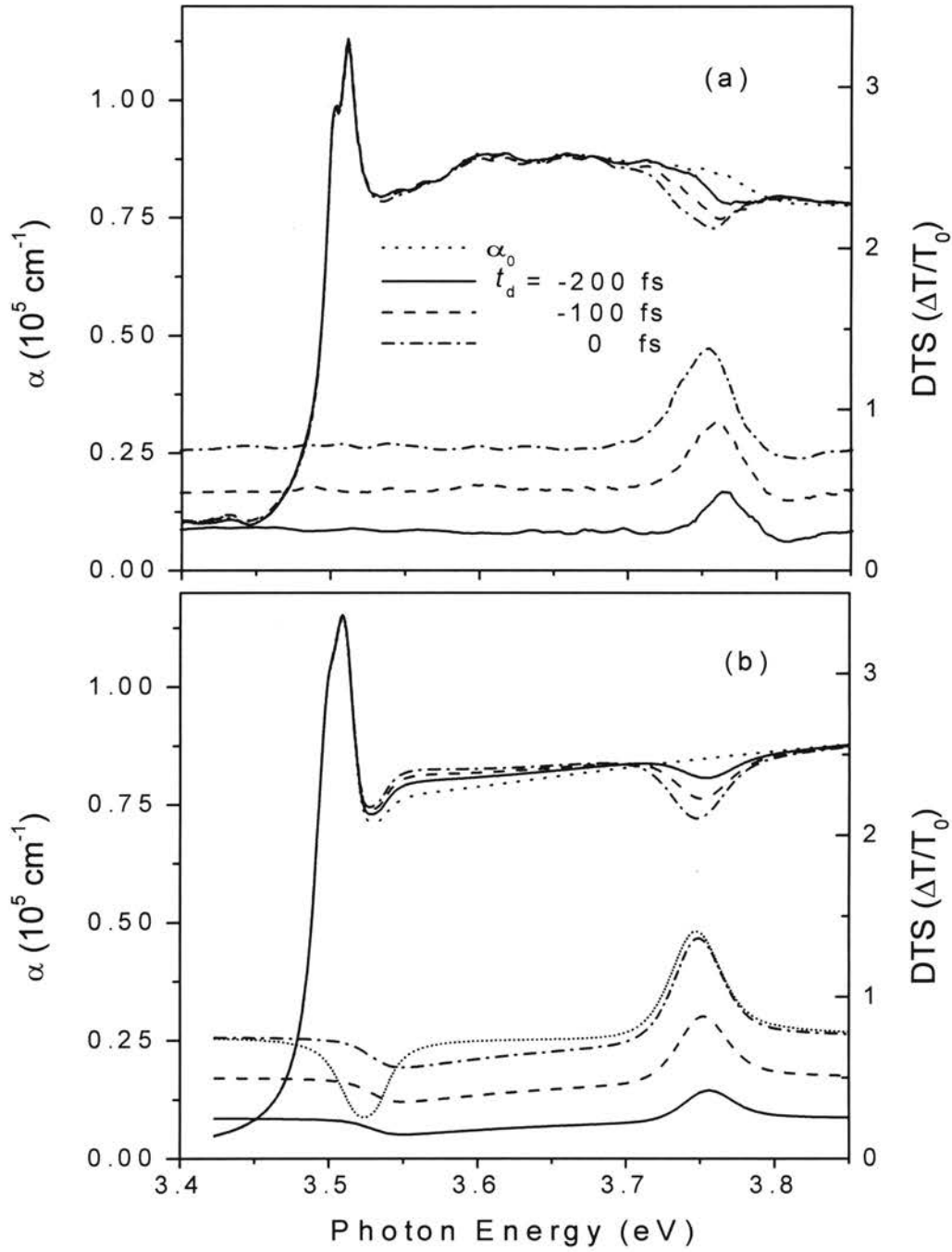
Figure 6. (a) Measured absorption and DTS at time delays of $t_d = -200$, -100, and 0 fs and at a peak carrier density of 4×10^{18} cm^{-3}. The dotted α_0 lines are the values taken without the pump beam. (b) The same as (a), except theoretically calculated (see text). The DTS curves are displaced vertically for clarity in both cases.

In contrast to GaAs, intervalley scattering does not occur in GaN for an excitation energy of 3.766 eV,[13] so electrons excited from the three valence bands into the conduction band reside in the Γ valley for all time delays. Compared to the rapid hot carrier redistribution in GaAs[30] and CdSe[31] over a wide energy range within 100 fs at much lower excitation density, Figure 7(a) shows that the hot carriers in GaN relax extremely slowly toward the band edge and are strongly restrained in a non-thermal distribution for ~ 0.7 ps, as shown by their rather narrow spectral peak. No LO phonon replica is observed for $t_d \leq 0.7$ ps, indicating a strong suppression of electron-LO phonon interaction. The detailed mechanism for this suppression remains unclear. One possible mechanism involves the anisotropy factor ($I_{kk'}$), which appears in the coupling matrix element and is proportional to the overlap of Bloch states of different wave vectors. This factor could be much less than 1 if the difference between k and k' is large. Assuming that electron-LO phonon scattering is blocked at early time delays, we can get insight into the role of carrier-carrier (CC) interaction in the initial thermalization through a comparison of our experimental results with a previous study of PP spectroscopy on bulk GaAs at 15 K, in which the carriers were excited well above the band gap similarly to our experimental conditions.[32] At a carrier density of 7×10^{17} cm^{-3}, the GaAs showed that the effective energy exchange among the carriers leads to an ultrafast thermalization by about 100 fs. At a high peak carrier density of 4×10^{18} cm^{-3} in GaN, our simulation results using screened CC interactions alone showed that the CC scattering already leads to a Fermi-Dirac distribution for the hot carriers (with a temperature consistent with the total kinetic energy of the carriers) at t_d = ~0.5 ps. Including the electron-LO phonon scattering clearly produces a LO phonon replica at 92 meV below the initial peak. This is inconsistent with our experimental result, which shows a non-thermal carrier distribution up to ~1 ps. This experiment suggests that there are other mechanisms that block the electron-LO phonon interaction and impede the carrier-carrier scattering. The mechanisms for such a surprisingly slow thermalization process is still unclear.
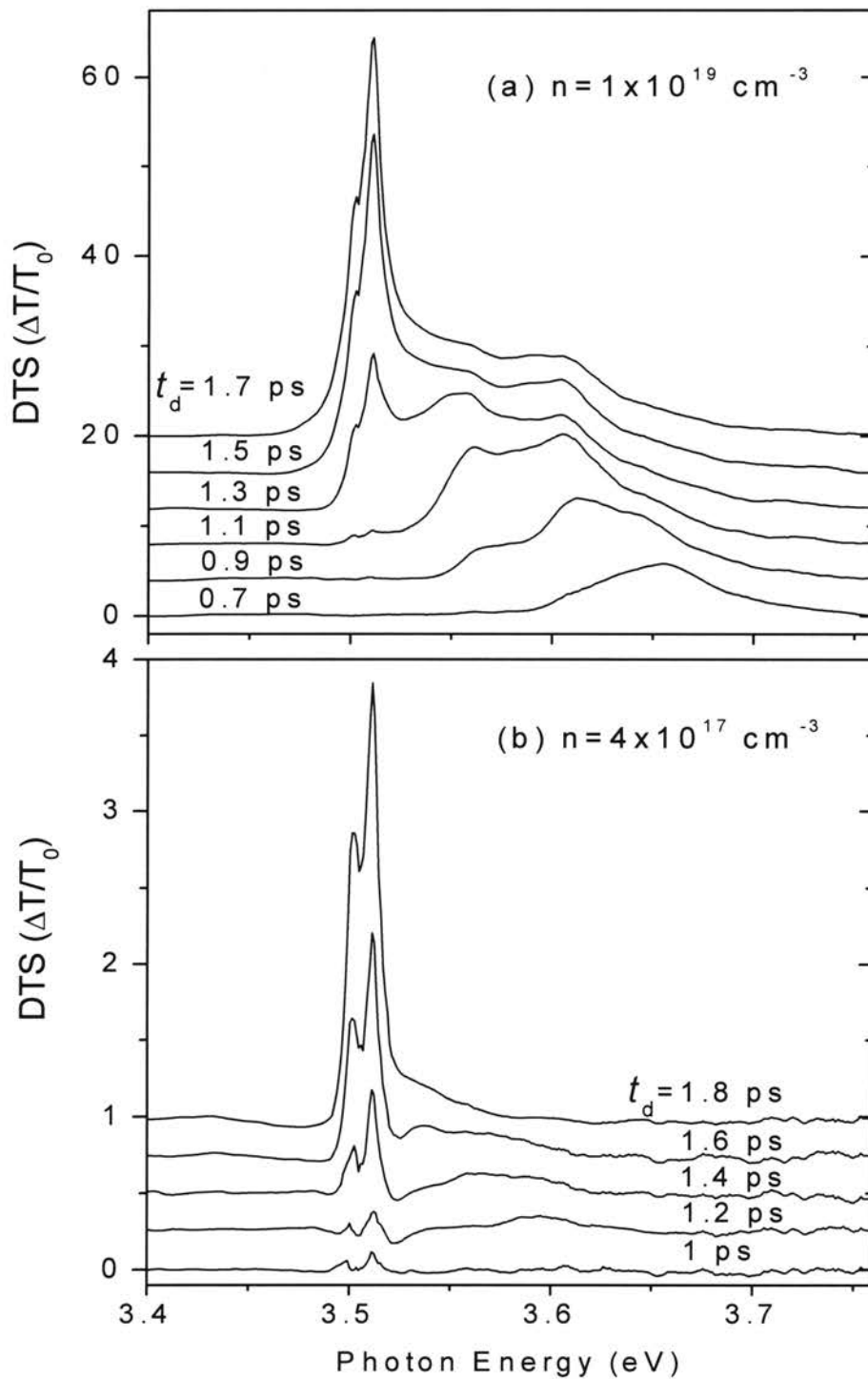
Figure 7. Spectrally resolved transmission changes as a function of time delay at peak carrier densities of (a) 1×10^{19} cm^{-3} and (b) 4×10^{17} cm^{-3}. The spectra were recorded 200 fs apart and displaced vertically for clarity.

We were able to clearly observe LO-phonon emission processes at time delays from 0.7 to 1.3 ps with a peak carrier density of 1×10^{19} cm^{-3}, as shown in Figure 7(a). At $t_d = 0.9$ ps, a shoulder arises at 3.56 eV because of the emission of single LO-phonons from the electron-hole plasma, which is peaked at 3.65 eV at $t_d = 0.7$ ps. With continuing LO-phonon emissions via the screened Fröhlich interactions, the shoulder grows and redshifts with increasing time delay. It is worth noting that the non-thermal carrier distribution at $t_d = 1.1$ ps in Figure 7(a), which appears as two separate peaks as a result of the LO-phonon emission, does not disappear very quickly. This indicates strong competition between the LO-phonon scattering process (including both emission and absorption) and the carrier-carrier scattering process, since they have comparable rates. At a peak carrier density of 4×10^{17} cm^{-3}, the carrier relaxation is almost completed at $t_d = 1.8$ ps, as shown in Figure 7(b). However, at a peak carrier density of 1×10^{19} cm^{-3}, many hot carriers are located at 3.60 eV at $t_d = 1.7$ ps, which means that the hot phonon effects are evident at high carrier density.

The presence of electrons and holes reduces the effective electron-hole attraction, not only through screening, but also through Pauli blocking (phase-space filling and short-range exchange effects). Both effects are always simultaneously present, but their relative importance changes with the dimensionality of the system.[33] Figure 8 shows absorption spectra near the band edge of GaN as a function of time delay at carrier densities both (a) above and (b) below the Mott density. Below the Mott density, as shown in Figure 8(b), exciton resonances saturate in a way which maintains the peak energy position through a balance between the reduction of the exciton binding energy and a redshift produced by the bandgap renormalization.[34] On the other hand, at a peak carrier density of 4×10^{18} cm^{-3} (higher than the Mott density), a redshift of 10 meV at $t_d = 1.6$ ps is seen in Figure 8(a), indicating that the redshift produced by the bandgap renormalization dominates over the reduction of the exciton binding energy. Using the long-wavelength approximation [$\epsilon(q)= \epsilon_0 (1+q_0^2/q^2)$] in Eq. (19), we estimate the long-range Coulomb screening effects by the non-thermal carriers on the exciton resonances. The screening length (q_0) at a peak carrier density of 4×10^{18} cm^{-3} decreases by only a factor of 2 from 200 fs to 1.8 ps. Further, we could not observe appreciable exciton bleaching effects, until 1 ps when the carriers began to fill the near-band-edge states,

indicating that long-range Coulomb screening by the non-equilibrium carriers does not provide the main contribution to the exciton bleaching. This could originate from the fact that the excitons do not strongly couple to non-thermal electron-hole plasma owing to overall charge neutrality. Similar delayed exciton bleaching was also observed in CuCl.[35]
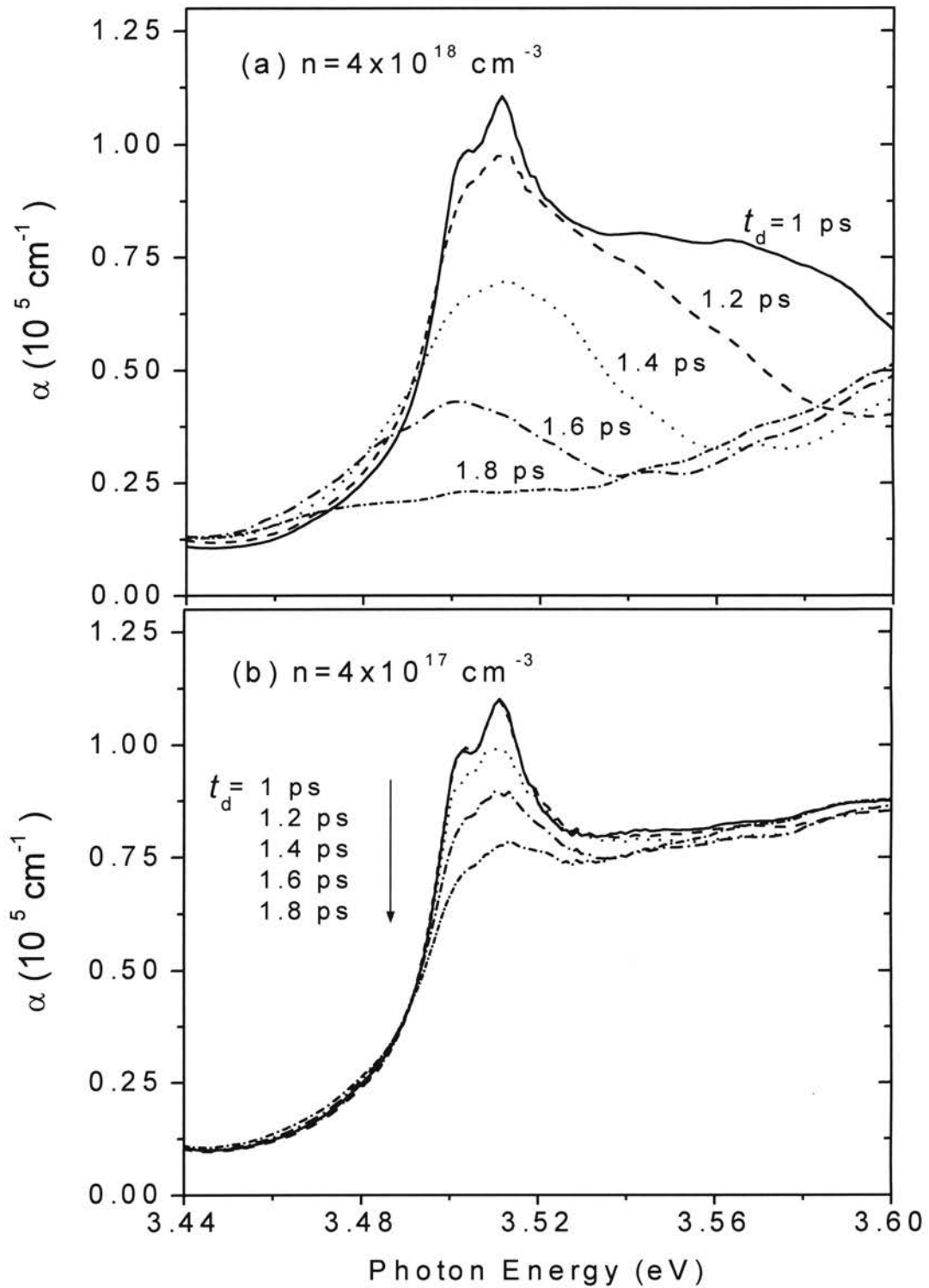
Figure 8. Absorption spectra near the band edge of GaN as a function of time delay for peak carrier densities of (a) 4×10^{18} cm^{-3} and (b) 4×10^{17} cm^{-3}. The spectra were recorded at 200 fs intervals from 1 ps to 1.8 ps. Note the induced absorption below the band edge.

Summary

In conclusion, we studied the hot carrier dynamics in a GaN epilayer excited well above the band edge at 10 K under high carrier densities. A spectral hole was initially peaked roughly at the excitation energy and gradually redshifted during the pump duration. We attributed the redshift of the hole to a combination of exciton effects and bandgap renormalization, which takes into account the non-equilibrium carrier distribution. Energy relaxation and thermalization of the hot carriers are extremely slow, due to blocking of the electron-LO phonon interaction and a large reduction in carrier-carrier scattering. At about 900 fs, LO-phonon emission processes via the screened Fröhlich mechanism were clearly observed at a peak carrier density of 1×10^{19} cm^{-3}. We found that phase-space filling and short-range exchange effects based on the Pauli exclusion principle play a more important role in the exciton bleaching than long-range Coulomb screening.

CHAPTER IV

THE EXCITONIC OPTICAL STARK EFFECT IN GaN

The dynamic Stark effect of excitons in GaN was studied using femtosecond pump-probe spectroscopy with various polarization configurations and pump detunings at 10 K. For high intensity pump pulses tuned well below the exciton resonances, a strong polarization dependence of the Stark effect on different pump and probe polarization configurations was observed. For the two different circular polarization configurations, the experimental results for GaN are qualitatively similar to those of GaAs/AlGaAs multiple quantum well structures (MQWS), due to similarities between the Bloch-state eigenfunctions of the MQWS heavy-hole (light-hole) subband and the GaN A (B) band Furthermore, similar to bulk GaAs, the dynamic Stark effect in GaN also depends on the relative linear pump and probe polarizations, which reflects 3-dimensional nature of bulk GaN.

Motivation

Since the pioneering observation of the resonant optical Stark effect (OSE) in bulk Cu_2O semiconductor,[36] the nonlinear interaction between a strongly oscillating electromagnetic field and optically saturable electronic transitions in semiconductors has been extensively studied, not only for physical interests, but also because of potential applications in optoelectronic devices. The various experiments have shown that the amount of the excitonic Stark shift, splitting, and bleaching depend sensitively on

34

excitation conditions, such as detuning, pulse duration, excitation intensity, relative pump-probe (PP) polarizations, and PP time delay.[37-43] According to Ref. 44, the excitonic optical nonlinearities result from anharmonicity in both the exciton-exciton and the exciton-photon interactions which depend directly on the excitation polarization and the density of virtual excitons. They showed that the photogenerated virtual excitons give rise to exactly the same physical processes as real ones, which allows for a physical interpretation of all the experimental observation. The dominant interaction is attributed to the fact that excitons are composite bosons made from fermions which obey the Pauli exclusion principle. Another approach to explain the Stark effect is based on a coupling between the exciton and all semi-virtual biexcitons. Each biexciton is made from one real electron-hole (e-h) pair by the probe and one virtual e-h pair by the pump.[45] This other approach gives the same result as Ref. 35 at a large pump detuning.

There has been tremendous interest in GaN and related materials, due to the fabrication of GaN-based blue laser diodes.[46] Many types of linear[47] and nonlinear[48] optical spectroscopy techniques have been used to study these wide-band-gap semiconductors. Recently, extremely slow energy relaxation and thermalization of the hot carriers in GaN, photoexcited well above the band gap, were observed by femtosecond PP spectroscopy.[49] Although there have been extensive studies of the excitonic OSE in other semiconductors,[36-39] to the best of our knowledge, no studies have been performed on GaN with excitation below the excitonic resonances.

We present a study of the OSE in a wurtzite GaN photoexcited well below the excitonic resonances with various polarization configurations, using non-degenerate PP spectroscopy at 10 K. We found a pronounced polarization dependence of the excitonic Stark effect on different circular pump and probe polarization configurations. By investigating the change of absorption spectra at the exciton resonances for σ^+ and σ^- polarized probe beams, while keeping a constant σ^+ pump polarization and intensity, we were able to evaluate the splitting of a degenerate exciton hidden inside the exciton linewidth, as a function of polarization. We also observed a distinct difference in the excitonic absorption for the co- and cross-linearly polarized pump and probe beams, indicating the 3-dimensional (3D) nature of bulk GaN.

Sample and experimental setup

The sample used in this study is a high quality 0.38 μm-thick wurtzite GaN epilayer grown by metalorganic chemical vapor deposition on a *c*-plane sapphire. An excitonic resonance was clearly observed in this sample's absorption above 300 K.[6] Our experimental setup is based on a 1 kHz regenerative amplifier (REGEN) to create 100 fs duration (FWHM) pulses at a wavelength of 800 nm. These pulses were fed into an optical parametric amplifier to create tunable excitation pulses below the excitonic resonances in GaN. This beam was used as the pump source with a FWHM of 260 fs and a bandwidth of 13 meV. The leftover output from the REGEN was frequency doubled to 400 nm and then focused onto a quartz crystal to create a broad-band continuum probe source with a FWHM of 200 fs. Neutral density filters were used to attenuate the probe beam to a sufficiently low intensity, so that it would not alter the optical properties of the sample. The pump and probe beam were, in turn, co-linearly (*xx*), cross-linearly (*xy*), co-circularly ($\sigma^+\sigma^+$), and opposite-circularly ($\sigma^+\sigma^-$) polarized. The probe beam was focused to a 100 μm diameter spot on the sample, and the transmitted probe was collected and focused into a spectrometer with an attached charge-coupled device detector. The pump spot size was focused to 250 μm to minimize the variation in the pump beam intensity across the probed region. The optical delay between the pump and the probe was accurately controlled using a computerized step motor. All measurements were performed at 10 K.

Results and discussion

Differential absorption ($\Delta\alpha$) measures the difference between the probe absorption with and without the pump:

36

$$\Delta\alpha(\omega)=\alpha(\omega)-\alpha_0(\omega)=\Sigma\eta_i\alpha_0(\omega-\Delta_i)\omega-\alpha_0(\omega)=-[\Sigma\eta_i\Delta_i](d\alpha_0(\omega)/d\omega) \qquad (25)$$

where Δ_i, η_i, and $\alpha_0(\omega)$ are the Stark shifts induced by the pump, and the relative interband transition weights depending on the pump and probe polarizations, and the unperturbed linear absorption, respectively.[39] The solid line in Figure 9(a) is the unperturbed linear absorption spectrum of GaN at 10 K. The valence band in GaN is split into three sub-bands by the crystal field and spin-orbit coupling, giving rise to three excitonic levels labeled A, B, and C, respectively. All experiments were performed with the probe beam wavevector along the c-axis of the GaN, so the C-exciton transition was theoretically forbidden and was not observed in the absorption spectrum. On the other hand, the A- and B-excitons appear fully with the same binding energy of ~21 meV.[47] Note that the B-exciton oscillator strength is about 1.2 times larger than that of the A-exciton in this GaN sample. This can be partially attributed to the compressive biaxial strain resulting from lattice and thermal-expansion mismatches between the GaN epilayer and the sapphire substrate.[47,50] Another contribution to the B-exciton oscillator strength comes primarily from an overlapping of the B-exciton transition with the A-exciton excited states and the A band absorption tail,[47] due to the small energy separation (~9 meV) between the A- and B-exciton transitions and their relatively broad absorption linewidths (~11 meV) for this sample.

Because of a large reduced mass in GaN, which leads to a broad exciton envelope function, we observed a substantial one-photon carrier generation with pump pulses of a few μJ, even at 50 meV detuning from the A-exciton resonance. To minimize one-photon carrier generation by the pump pulses and to study the true optical Stark effect, we used large detunings. We took the zero time delay to be at the approximate maximum of the pump pulse. As seen in Figure 9(a), the amount of the B-exciton oscillator strength reduces with increasing pump intensity, and the B-exciton resonance blueshifts linearly at 0 ps time delay (Δt_d). This is consistent with theoretical predictions that the Stark shift is proportional to the pump intensity and inversely proportional to the pump detuning for a large detuning.[44,45] Physically, this Stark shift is predominantly caused by the nonlinear exciton-photon interaction since the effect of exciton-exciton interaction on the Stark shift plays a minor role in bulk semiconductors.[51] We note that CuCl has an exciton redshift when the pump is detuned just below the bi-excitonic resonance and is polarized

the same as the probe.[42] This CuCl transient excitonic redshift was attributed to the large molecular biexciton binding energy of 28 meV[52] and the Coulomb interaction between excitons and virtual biexcitons. However, the GaN biexciton binding is only 5.7 meV[53] and the pump detunings used here are far from the bi-excitonic resonance, so the Coulomb interaction between the excitons and the virtual biexcitons is not strong enough to cause such a redshift. While a pure excitonic Stark shift of exciton, i.e., a shift of the absorption spectrum without any loss of oscillator strength, has been reported for GaAs/AlGaAs MQWS at a low excitation intensity and moderate detuning, Figure 9(b) shows a large and transient exciton bleaching in GaN as a result of phase space filling (PSF) and screening effects by pump-generated virtual excitons. The bleaching and shift exist during an intense pulse, except for a small and long-lived component that is mainly caused by a large two-photon absorption (TPA) in GaN.[54,55] This transient bleaching indicates that, in our experimental conditions, PSF and screening effects due to the virtual exciton populations dominate over an increased exciton binding energy, which causes an increased exciton oscillator strength and is due to a larger blueshift in the exciton continuum states than in the bound states, in the presence of virtual excitons. According to Refs. 56 and 57, the amount of exciton bleaching increases almost linearly with decreasing pump duration at a constant energy per pulse, while the blueshift of the excitonic resonance is nearly independent of the pump duration. Therefore, the large exciton bleaching in Figure 9(b) also indicates that the pump duration is shorter than the exciton dephasing time of 300 fs in GaN.[48] This is in agreement with a coherent oscillatory structure[17] in the differential absorption around the excitonic resonances at Δt_d = −0.3 ps, when the probe precedes the pump.
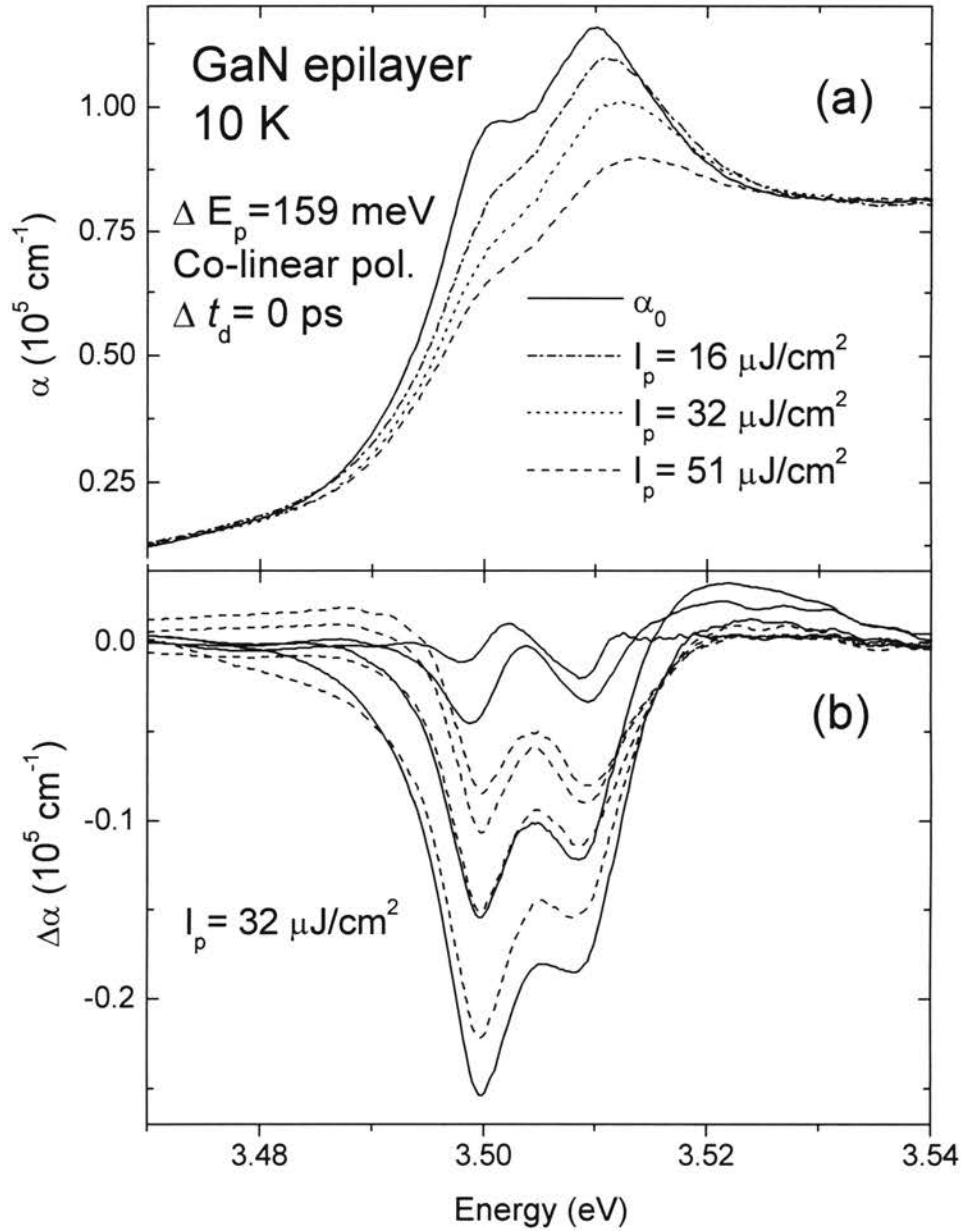
Figure 9. (a) Absorption spectra of a 0.38 μm-thick GaN sample near the *A*- and *B*-exciton resonances at a time delay of 0 ps at 10 K with co-linearly polarized pump and probe pulses for different indicated pump intensities. The pump is detuned from the *A*-exciton resonance by 159 meV, and the pump pulse has a FWHM of 12.7 meV. The solid line is the absorption spectrum without the pump. (b) Time-resolved differential absorption spectra (Δ*α*) for co-linear polarization at a pump intensity of 32 μJ/cm². The Δ*α* at first decrease with time due to bleaching, as shown by the solid curves with time delays of Δ*t*ₐ = -0.3, -0.2, -0.1, and 0 ps. Then, the spectra recovery, as shown by the dashed curves with at Δ*t*ₐ = 0.1, 0.2, 0.3, and 0.5 ps.

Under irradiation of a resonant (nonperturbative) or off-resonant (perturbative) electromagnetic field, semiconductor excitons (which are degenerate states when made from the bare conduction and valence bands) not only shift but also split due to different optical Stark shifts in the various conduction and valence levels. Although excitonic Stark splitting has been clearly observed in a single quantum well in the nonpertubative regime,[43] the GaN Stark shifts are very small compared to the broad exciton linewidth in the perturbative regime, so it is difficult to directly observe the splitting in GaN. To investigate the GaN excitonic splitting hidden inside the exciton linewidth, we used various pump and probe polarization configurations to separately identify conduction and valence band exciton shifts, as was done in bulk GaAs and GaAs/AlGaAs MQWS.[39] Figure 10 shows a pronounced dependence of the OSE on the relative linear pump and probe polarization configurations at $\Delta t_d = 0$ ps. The fact that $\Delta\alpha$ is nearly same for the xx and the xy configurations at $\Delta t_d = 0.5$ ps, when the pump is completely off, indicates that the pump intensity was the same for both cases, since the long decay component of $\Delta\alpha$ is mainly due to TPA. The xx to xy signal ratio at the A (B)-exciton resonance is about 1.5 (1.8) and does not depend sensitively on pump intensity. With the same virtual exciton population (i.e., a completely degenerate and radiation-broaden Fermi distribution at zero temperature)[44] in the xx and xy configurations, this polarization dependent exciton bleaching results from the different blueshifted A- and B- excitonic transition weights for x- and y-polarized probe beams on the basis of perturbation theory.[39,45] In 2D GaAs/AlGaAs MQWS, which has Bloch-state eigenfunctions similar to those of GaN, the OSE does not depend on the relative linear pump and probe polarizations.[37] On the other hand, in 3D bulk GaAs, a similar behavior of the OSE has been reported,[39] indicating that this dependence originates from the 3D nature of bulk GaN.
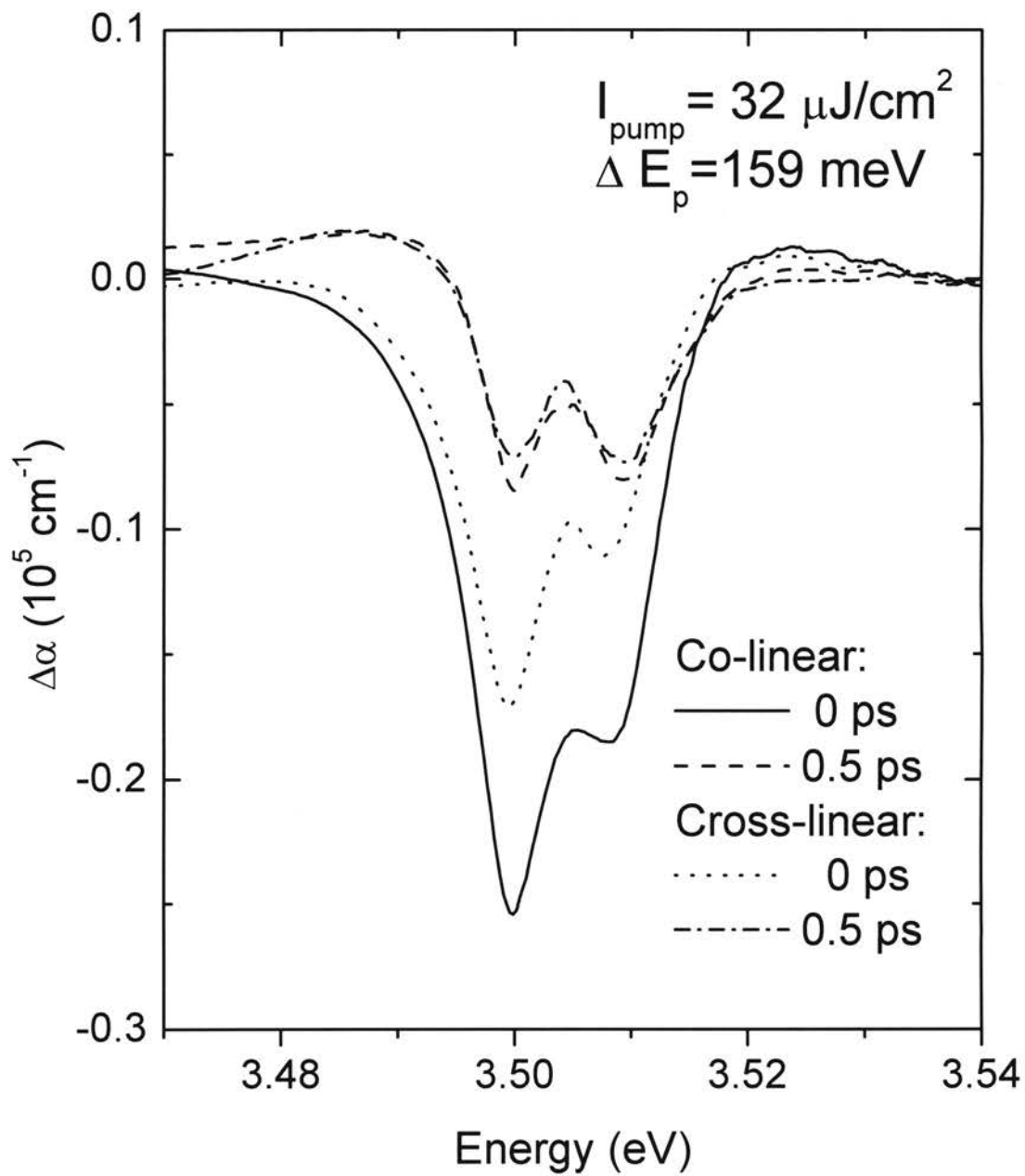
Figure 10. Differential absorption spectra for co- and cross-linear pump and probe polarizations at $\Delta t_d = 0$ and 0.5 ps. The pump located at 3.343 eV has a spectral width of 12.7 meV.

Figure 11 shows $\Delta\alpha$ for $\sigma^+\sigma^+$ and $\sigma^+\sigma^-$ polarization configurations at a pump detuning of 140 meV below the A exciton resonance. A distinctive $\Delta\alpha$ difference between the $\sigma^+\sigma^+$ and $\sigma^+\sigma^-$ configurations indicates the excitonic Stark splitting of degenerate exciton states by the σ^+-polarized pump, as illustrated in Figure 12. Wurtzite GaN Bloch-state eigenfunctions near the Brillouin zone center are designated $|l=0, s=\pm 1/2\rangle$ for the s-like conduction band, $|j=3/2, m=\pm 3/2\rangle = |l=\pm 1; s=\pm 1/2\rangle$ for the A valence band, $|3/2, \pm 1/2\rangle = [(E^0_B - \lambda_\epsilon)/(E^0_B - E^0_C)]^{1/2} |\pm 1; \mp 1/2\rangle + [(E^0_C - \lambda_\epsilon)/(E^0_C - E^0_B)]^{1/2} |0; \pm 1/2\rangle$ for the B valence band, and $|1/2, \pm 1/2\rangle = -[(E^0_B - \lambda_\epsilon)/(E^0_B - E^0_C)]^{1/2} |0; \pm 1/2\rangle + [(E^0_C - \lambda_\epsilon)/(E^0_C - E^0_B)]^{1/2} |\pm 1; \mp 1/2\rangle$ for the C valence band.[58] Here, E^0_B (E^0_C) is the optical transition energy at the zone center from the B (C) valence band to the conduction band and λ_ϵ depends on the deformation potentials and the strain tensors.[58] Except for the interband transition amplitudes for the B and C valence bands, the above GaN eigenfunctions are the same as those of GaAs MQWS. In the $\sigma^+\sigma^-$ configuration, the larger bleaching of the B-exciton resonance is due to (i) a larger number of pump-excited σ^+ A-excitons than σ^+ B-excitons and (ii) a stronger B-exciton oscillator strength than that of the A-exciton, as shown in Figure 9(a). For a σ^+ or σ^--polarized probe beam, the ratio of A- to B-excitonic oscillator strength in GaN is found to be $(E^0_B - E^0_C)/(E^0_B - \lambda_\epsilon)$, using typical selection rules. According to Ref. 50, this value at zero strain is slightly larger than 1 and gradually increases with increasing compressive biaxial strain. Compared to the excitonic Stark effect in GaAs/AlGaAs MQWS with the same co- and opposite-circular pump and probe polarizations,[37] Figure 11 shows much larger bleaching at the B-exciton resonance. Considering the 3 : 1 ratio of the heavy and light hole oscillator strengths in 2D GaAs/AlGaAs MQWS, this difference between the material systems is expected. As seen in Figure 7, with σ^+ pumping, a σ^+ probe with a kinetic angular momentum of $+1$ can detect both conduction and valence band Stark shifts induced by the pump, but a σ^- probe with a kinetic momentum of -1 can only detect conduction band Stark shifts. From Figure 11, we can sketch the relative Stark shifts shown in Figure 12. The conduction band Stark shifts are larger than the valence band

Stark shifts, and the $|l = 0; s = +1/2\rangle$ conduction band Stark shift is larger than the sum of the $|l = 0; s = -1/2\rangle$ conduction and $|j = 0; m = -1/2\rangle$ valence band Stark shifts.
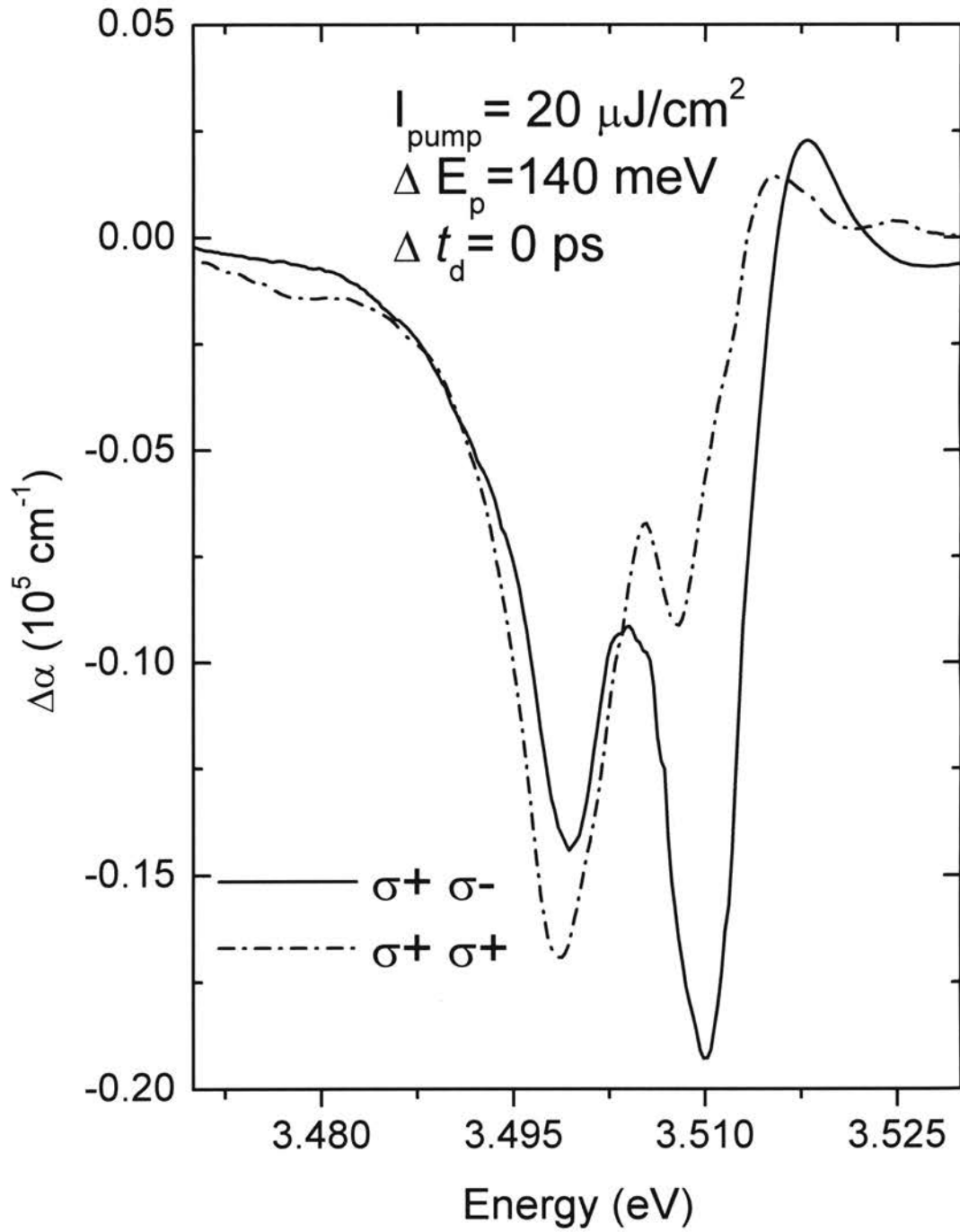
Figure 11. Differential absorption spectra at $\Delta t_d = 0$ ps for opposite- (σ^+ and σ^- for the pump and probe, respectively) and co-circular (σ^+ for both the pump and probe beams) polarizations. The pump pulse is detuned 140 meV below the A-exciton resonance with an intensity of 20 $\mu J/cm^2$.
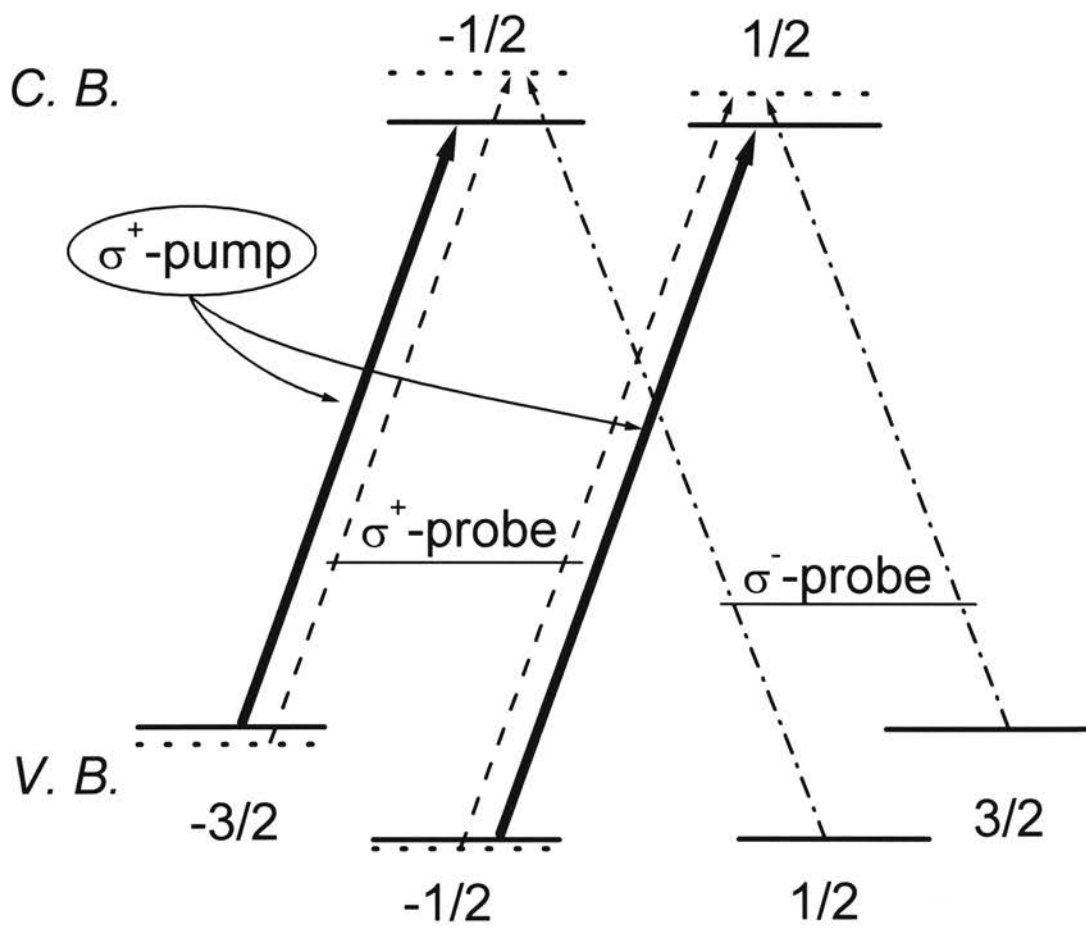
Figure 12. Optical selection rules of the *A* and *B* excitonic transitions.

Summary

In conclusion, we studied the dynamic excitonic Stark effect in GaN at 10 K with various pump and probe polarization configurations in the nonperturbative regime. For the linear polarization configurations, the differential absorption spectra clearly show the 3-dimensional nature of bulk GaN. We also observed a pronounced difference in the excitonic absorption for co- and opposite-circularly polarized pump and probe beams, evidencing the splitting of degenerate excitonic states in GaN as well as their blueshifts under irradiation of a non-resonant pump field, similar to 2-dimenional GaAs/AlGaAs multiple quantum wells.

CHAPTER V

FEMTOSECOND PUMP-PROBE SPECTROSCOPY AND TIME-RESOLVED
PHOTOLUMINESCENCE OF AN InGaN/GaN
DOUBLE HETEROSTRUCTURE

In this chapter a study of the carrier dynamics in an $In_{0.18}Ga_{0.82}N$ thin film photoexcited well above the band gap using non-degenerate pump-probe spectroscopy and time-resolved photoluminescence (TRPL) for carrier densities ranging from 10^{17} to 10^{19} cm^{-3} at 10 K is presented. At carrier densities greater than 4×10^{18} cm^{-3}, optical gain occurs across the entire band tail region after ~2.5 ps time delay, when the hot carriers completely fill these states. From TRPL measurements performed in the surface emission geometry, we observed stimulated emission (SE) with a ~28 ps decay time. Since this SE has a threshold density of 1×10^{18} cm^{-3}, which is larger than the total density of localized states, and the SE spectra at early time delays are quite different from the spontaneous emission spectra, we attribute the stimulated emission to the recombination of an electron-hole plasma from renormalized band-to-band transitions.

Motivation

The desire for ever higher resolution printing, read-write laser sources for high-density information storage on magnetic and optical media, and sources for secure inter-satellite communications has fueled an interest in semiconductor lasers operating at shorter wavelengths. A long-lived continuous-wave blue InGaN quantum well (QW)

47

diode laser grown on a sapphire substrate was recently demonstrated at room temperature.[59] Despite extensive studies on the optical properties of $In_xGa_{1-x}N$ ternary alloys as the active light-emitting medium, the optical gain and stimulated emission (SE) mechanisms in these technologically promising new sources are still unclear. A major issue related to carrier dynamics is the many-body Coulomb interaction among electrically injected or photogenerated carriers in localized and extended states, given the high carrier densities (larger than 10^{19} cm^{-3})[59] required to achieve lasing in present devices.

In this chapter, we report a study of the carrier dynamics in an InGaN thin film for carrier densities varying from 10^{17} to 10^{19} cm^{-3} photoexcited well above the band edge, using femtosecond non-degenerate pump-probe (PP) spectroscopy and time-resolved photoluminescence (TRPL) measurements at 10 K. Through these measurements, we explored not only the early-stage thermalization processes of the hot carriers, but also the spectral and temporal properties of the recombination processes, both as functions of carrier density.

Sample and experimental setup

The sample used in this study is a nominally undoped 0.1 μm-thick $In_{0.18}Ga_{0.82}N$ epilayer grown by metalorganic chemical vapor deposition at 800 °C. The structure consists of a 20 nm GaN buffer layer grown on c-plane sapphire followed by a 1.8 μm GaN layer, a 50 nm GaN:Si (Si ~10^{18} cm^{-3}) layer, the 0.1 μm $In_{0.18}Ga_{0.82}N$ layer, and a 50 nm GaN:Si (Si ~10^{19} cm^{-3}) cap layer. The average In composition was measured using high-resolution x-ray diffraction, assuming Vegard's law. We note that the actual InN fraction could be smaller due to systematic overestimation when using Vegard's law for this strained material system.[60]

Since the $In_{0.18}Ga_{0.82}N$ conduction band edge lies at a lower energy than the GaN:Si donor states, electrons from the donors will move into the $In_{0.18}Ga_{0.82}N$ region. The self-consistent potential seen by an electron in the double heterostructure can be

modeled by an effective mass theory that takes into account the exchange-correlation potential within the local density approximation. We use the same numerical method described in Ref. 61 for modeling heavily doped semiconductor multiple quantum wells (MQWs). At low temperature (T≈10 K), most of the carriers remain trapped at the GaN:Si donor sites with only a small fraction migrating into the InGaN layer. The amount of charge transfer is determined by requiring the Fermi level to be the same across the GaN and InGaN layers (about 30 meV below the GaN conduction band minimum, which is taken to be zero in this calculation). The resulting self-consistent potential (solid curve) and carrier density (dashed curve) are shown in Figure 13. For the heavily doped GaN cap layer, donor electrons within 2.2 nm from the front GaN/InGaN interface are depleted, contributing to the 2-dimensional (2D) carrier density of 1.1×10^{12} cm^{-2} in the left triangular InGaN QW. For the less heavily doped GaN layer under the InGaN layer, donor electrons within 15 nm from the back InGaN/GaN interface are depleted, contributing to the 2D carrier density of 7.5×10^{11} cm^{-2} in the right triangular InGaN QW. The total 2D carrier density in the InGaN layer is 1.85×10^{12} cm^{-2}, which is not enough to substantially screen the Coulomb interaction among photo-excited carriers.

Femtosecond PP spectroscopy measurements were carried out with a 1 kHz regenerative amplifier (REGEN) used to create pulses with a full width at half maximum (FWHM) of 100 fs at a wavelength of 800 nm. These pulses were fed into an optical parametric amplifier to create pulses with a FWHM of 355 fs (measured by difference-frequency mixing in a BBO crystal) at 3.345 eV (295 meV above the absorption edge of the excited InGaN sample at 10 K) with a bandwidth of 25 meV. This beam was used as the pump source to excite carriers above the $In_{0.18}Ga_{0.82}N$ band gap. The leftover output from the REGEN was frequency doubled to 400 nm and then used to create a broad-band continuum probe source with a FWHM of 350 fs. The pump and probe beams were orthogonally polarized, and the angle between them was 15°. Neutral density filters were used to attenuate the probe beam so it would not alter the optical properties of the sample. The probe beam was focused to a 150 μm diameter spot on the sample, and the transmitted light was collected and focused into a spectrometer with an attached CCD detector. A pump spot size of 300 μm was chosen to minimize the variations in pump beam intensity and to average out the effect of In compositional fluctuations across the

49

probed region. The optical delay between the pump and probe was controlled using a computerized stepper motor. TRPL measurements were also performed in the surface emission geometry using a streak camera with a monochromator. The pump spot size was 150 μm in diameter and the overall time resolution for TRPL measurements was about 60 ps. For consistency, the same excitation energy was used for PP and TRPL experiments.
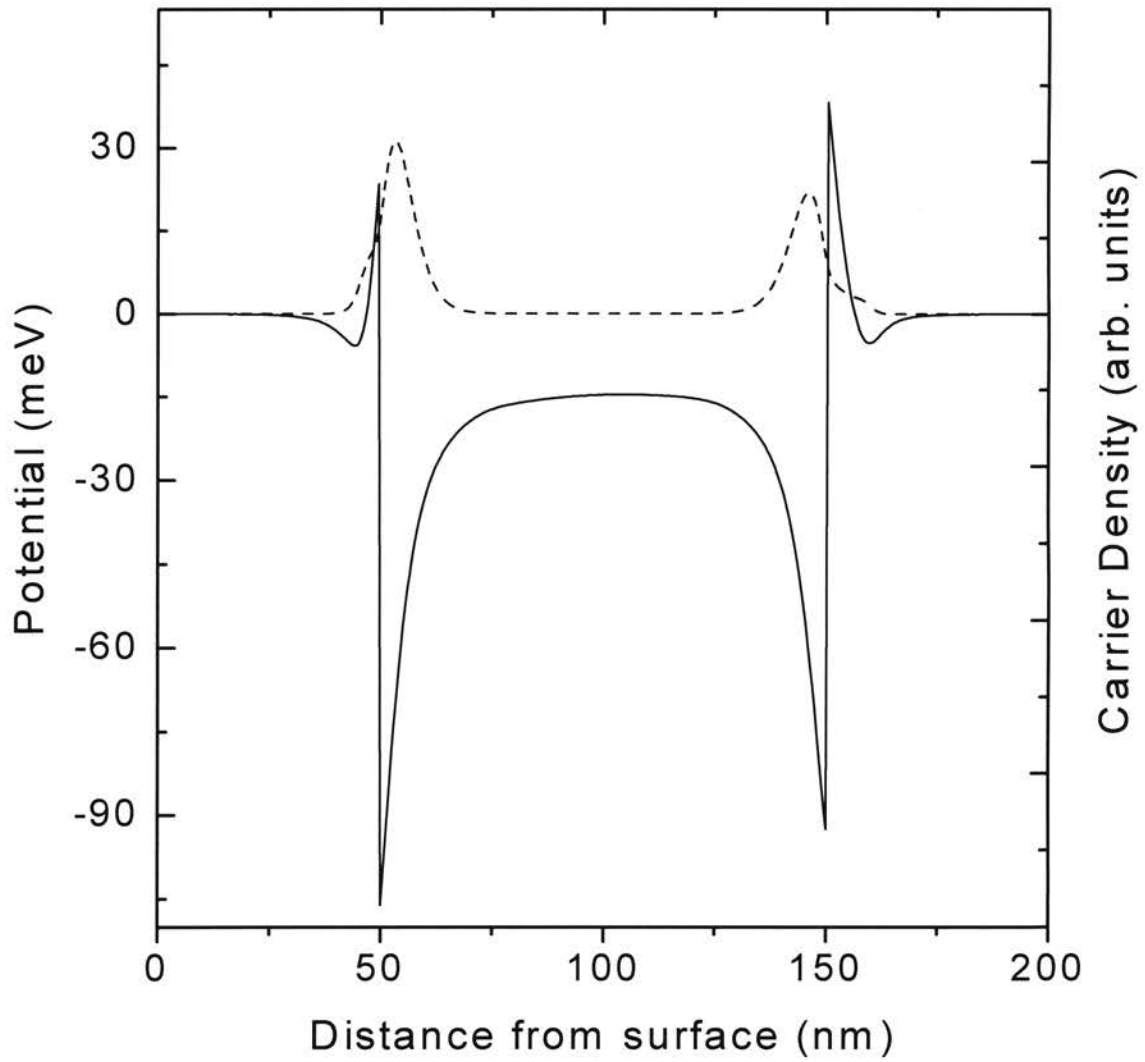
Figure 13. Self-consistent potential profile seen by an electron across the InGaN layer (solid line). Also shown is the carrier distribution (dashed line).

Results and discussion

Differential transmission spectra (DTS)[10] measure the difference between the probe transmission with and without the pump:

$$\text{DTS} = \Delta T / T_0 = (T - T_0) / T_0 = [\exp(-\int_0^d \Delta\alpha(z)\,dz)] - 1,$$

where T, T_0, $\Delta\alpha(z)$, and d are the transmitted probe intensity with and without the pump, the pump-induced absorption change at depth z (measured from the front side interface), and the sample thickness, respectively. For an active layer thickness of 0.1 μm with an absorption coefficient of 1.5×10^5 cm^{-1} at the excitation energy, our sample is optically thick, so the photo-generated carrier density depends on the depth z, which leads to a depth-dependent absorption coefficient $\alpha(z)$. Figure 14 shows the DTS at early time delays for an average carrier density of 3×10^{18} cm^{-3} in the active layer, as estimated from band filling.$^{£}$ Using this average carrier density and assuming an exponential decrease in the photo-generated carrier density with depth, we estimate the carrier density at the front side interface ($z = 0$ nm) and at the back side interface ($z = 100$ nm) to be 5.7×10^{18} cm^{-3} and 1.3×10^{18} cm^{-3}, respectively. We see in the inset that the low-density photoluminescence (PL) peak (dotted line) is significantly Stokes shifted (~58 meV) with respect to the fundamental absorption edge. This behavior arises from the combined effects of the large band bending near the interfaces and In compositional fluctuations[62-65] in this mixed semiconductor alloy. We take zero time delay to be at the approximate maximum of the pump pulse. For time delays of less than -200 fs, no significant band filling effects were observed.

$^{£}$ Because of a large uncertainty in the quantum efficiency of the electron-hole pair generation and experimental difficulties in measuring the reflectance and transmittance of sample, we calculated the carrier density using the band filling factor $[1-f_e-f_h]$ (see p. 22 in Ref. 10), assuming a simple parabolic band structure and equal occupation probabilities $[f_e = f_h]$ of electrons and holes. In both PP and TRPL measurements, we measured nominal excitation energy densities. After comparison between the calculated carrier density from the band filling factor and the measured nominal excitation energy density, we obtained a calibration factor. Then, carrier densities in TRPL measurements were determined with the calibration factor.
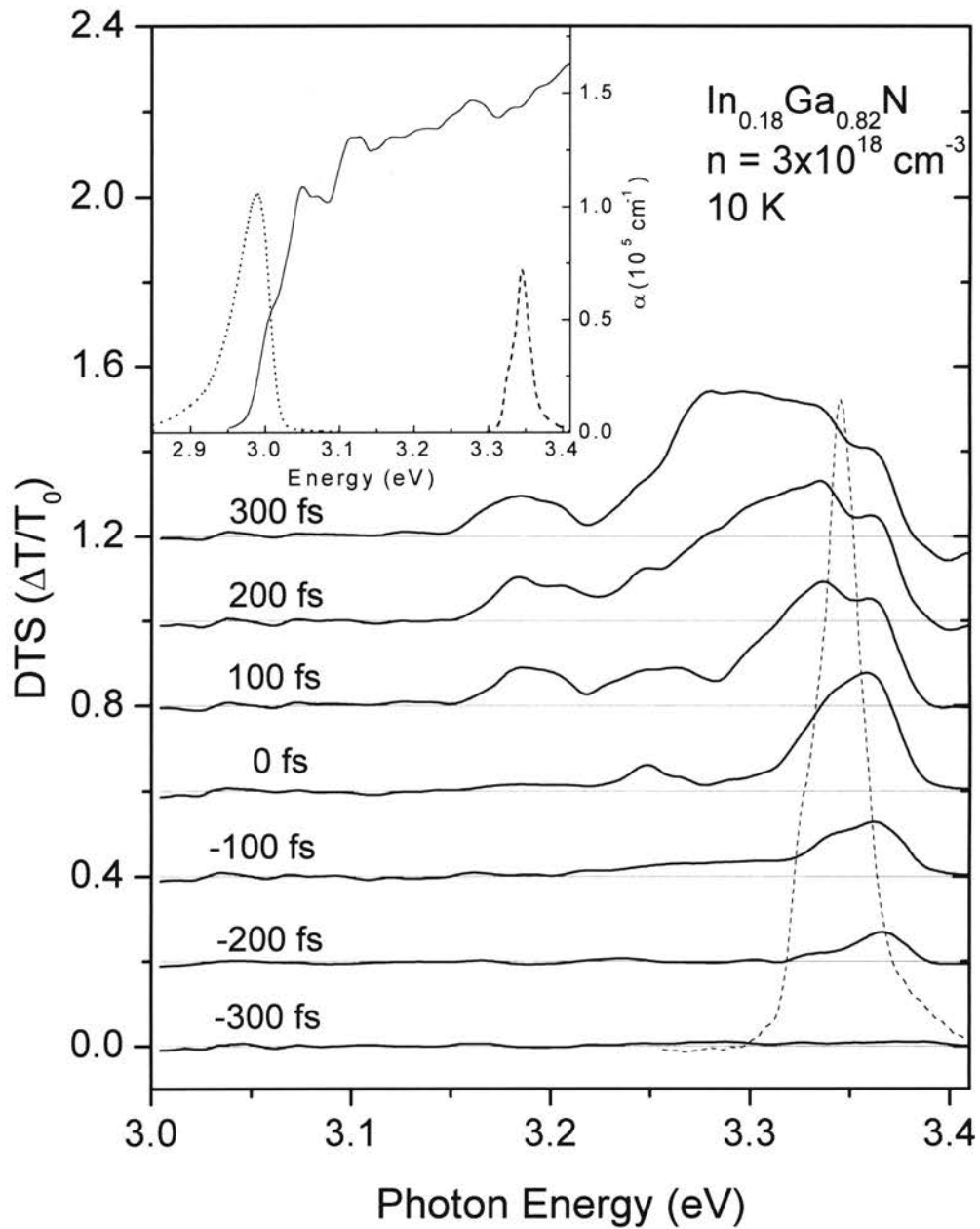
Figure 14. Differential transmission spectra (pump-induced transmission change $\Delta T/T_0$) of a 0.1 μm $In_{0.18}Ga_{0.82}N$ active layer at 10 K for an average carrier density of 3×10^{18} cm^{-3} showing the ultrafast near-zero-delay dynamics. The dashed line shows the pump spectrum. The DTS curves are displaced vertically for clarity. The inset shows the absorption (solid line), PL (dotted line), and pump spectra for the pump-probe spectroscopy (dashed line).

The DTS at -200 fs shows a spectral hole burning[18] which is initially peaked at the high-energy tail of the pump pulse. At -100 fs, a broad low energy tail arises from the fast interaction of photoexcited carriers with the previously existing electrons, as shown in Figure 14. We clearly observed two successive LO-phonon emission processes via the Fröhlich interaction at 0 and 100 fs time delays. At 0 fs, a broad peak at 3.25 eV arises from the emission of single LO-phonons, and at 100 fs, another broad peak occurs at 3.18 eV because of two successive LO-phonon emissions. The spacing is approximately equal to the expected $In_{0.18}Ga_{0.82}N$ LO-phonon energy of 89 meV, which is estimated by a linear interpolation of the values of 92 meV[66] and 74 meV[67] for GaN and InN, respectively. However, the successive LO-phonon emission does not necessarily mean that relaxation processes of the hot carriers can be explained by a simple LO-phonon cascade model. Considering the non-thermal carrier distribution on this time scale of less than 100 fs, and the decrease in the joint density of states with decreasing photon energy (which causes the DTS values to increase), only a small fraction of the hot carriers should be involved in the successive LO-phonon emissions. Similarly observed LO-phonon replicas during the pump duration was previously reported in GaAs at a carrier density of 8×10^{14} cm^{-3}.[27]

As shown in Figure 14, the cooling processes of most of the carriers begin after the initial buildup of carriers by the pump. Carrier-carrier interactions which cause the gradual broadening of the non-thermal carrier distribution and electron-phonon scattering by both the Fröhlich and the deformation-potential mechanisms provide the most relevant relaxation processes. Compared to the rapid hot carrier redistribution in GaAs[30] over a wide energy range within 100 fs at a lower excitation density, Figure 14 shows that the hot carriers relax very slowly toward the band edge. This is mainly caused by the hot phonon effect,[22] since the electrons lose energy to LO-phonons very slowly when the LO-phonons are as hot as the electrons. Previously, a slow hot carrier relaxation in this material due to the hot phonon effect has been reported at 300 K.[68]

The carrier dynamics near the absorption edge of the sample is shown Figure 15 as a function of time delay for average carrier densities of (a) 4×10^{18} cm^{-3} and (b) 4×10^{17} cm^{-3}. The arrows indicate the effective mobility edge[69] (E_{em}) of the sample, which was determined by the excitation energy dependence of the PL peak position as detailed in

Ref. 70. For an average carrier density of 4×10^{18} cm^{-3}, the average inter-particle distance is about 3 nm, which is approximately equal to the exciton Bohr radius in GaN. Thus, the hot carriers of Figure 15(a) form an electron-hole plasma (EHP), while a coexistence of correlated states (excitons) and uncorrelated electron-hole pairs is possible at the average carrier density of Figure 15(b). As the hot carriers relax toward the band edge, the band gap reduces, leading to induced absorption near and below the absorption edge appearing after ~1.3 ps, as shown in Figures 15(a) and (b). Subsequently, the induced absorption reduces and turns into optical gain (or induced transparency) due to band filling by the hot carriers. The weak modulation in the resulting gain spectra comes from the Fabry-Perot modes of the sample structure. As shown in Figure 15(a), optical gain across the entire band tail is evident at an average carrier density of 4×10^{18} cm^{-3}, and has a maximum value of ~1.2×10^4 cm^{-1} at 2.5 ps. Previous studies of PP spectroscopy on bulk GaAs[71], GaAs/AlGaAs MQWs[72], and InGaN/GaN MQWs[73] also showed optical gain near the band edge. Assuming that a single round-trip condition in the sample growth direction is satisfied and that there is no loss due to absorption in the InGaN active layer, a threshold gain for vertical-cavity SE was found to be 10^5 cm^{-1} for 20 % reflectivity at both side interfaces and a gain length (active layer thickness) of 0.1 μm.[74] Since this threshold gain value is one order of magnitude larger than the experimentally observed optical value of ~1.2×10^4 cm^{-1} at an average carrier density of 4×10^{18} cm^{-3}, it may not be possible to achieve vertical-cavity SE from optical pumping except under extremely high excitation densities. At 3 ps in Figure 15(b), there are still available states below E_{em}, but most of the carriers are situated at energies above 3.04 eV. This means that the total density of localized states due to In compositional fluctuation is less than 4×10^{17} cm^{-3}. To be consistent, the TRPL measurements seen below show that the PL peak position does not shift up to an average carrier density of 1×10^{17} cm^{-3}, but it has a significant blueshift at an average carrier density of 5×10^{17} cm^{-3} due to band filling of the localized states. Therefore, we estimate the total density of localized states in this sample to be between 1×10^{17} cm^{-3} and 4×10^{17} cm^{-3}.
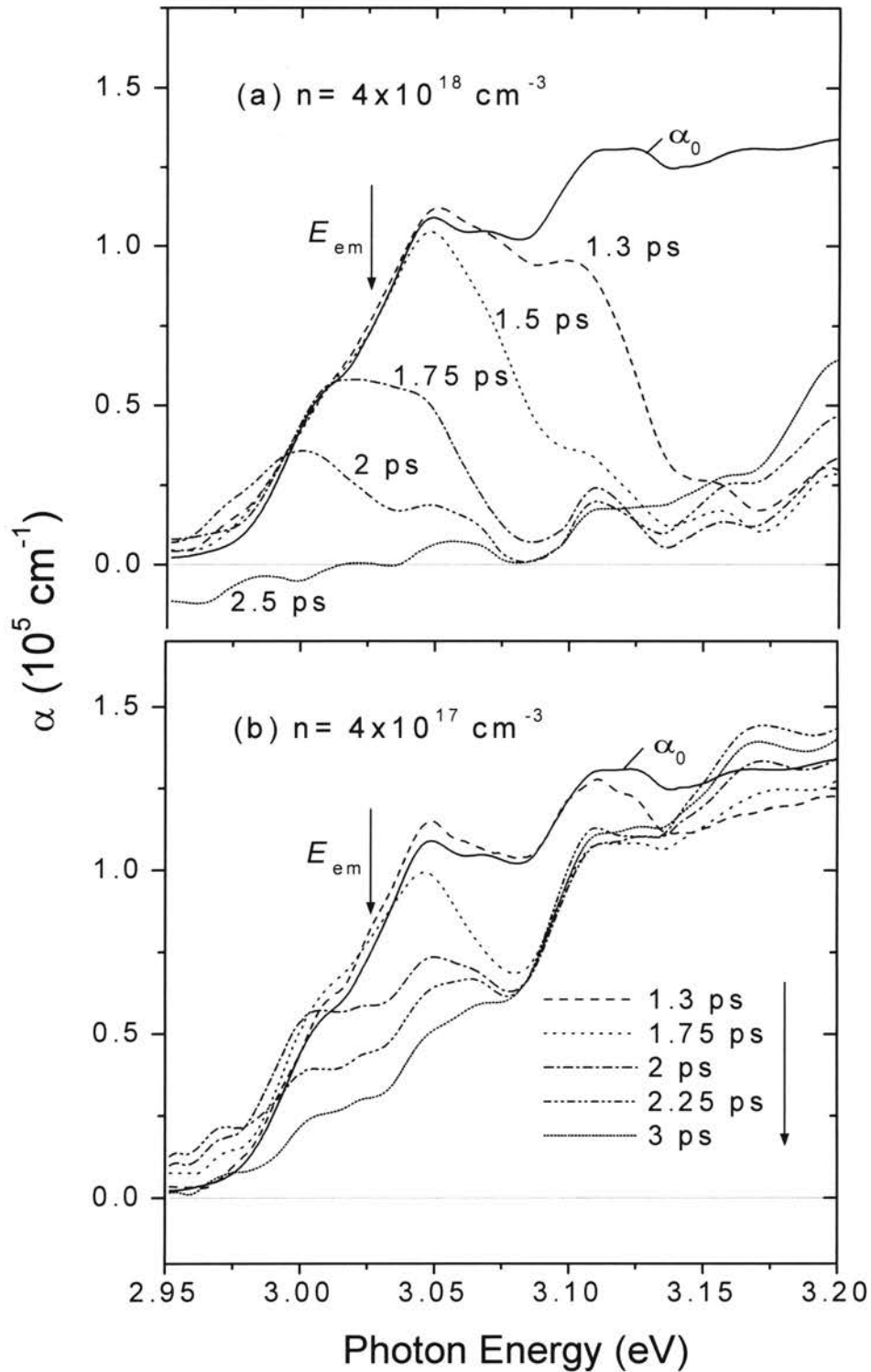
Figure 15. Absorption spectra near the fundamental absorption edge of an $In_{0.18}Ga_{0.82}N$ active layer as a function of time delay for average carrier densities of (a) 4×10^{18} cm^{-3} and (b) 4×10^{17} cm^{-3}. The solid lines represent the values taken without the pump (α_0). The arrows indicate the effective mobility edge (see text).

The energy relaxation rate of hot carriers depends strongly on the number of available lower energy states and decreases quickly with decreasing energy within the band tail due to the reduced density of the final states. Absorption spectra and their corresponding DTS near the band tail region at time delays from 10 to 50 ps are shown in Figure 16. The recovery from bleaching effects at an average carrier density of 1×10^{17} cm^{-3} is much slower than at 3×10^{18} cm^{-3} [note the bleaching across the entire tail region at 2.5 ps in Figure 15(a)]. This indicates that a very fast and efficient carrier depopulation process, i.e. SE, exists at an average carrier density of 3×10^{18} cm^{-3}. At average carrier densities greater than 1×10^{18} cm^{-3}, our TRPL measurement results show that most of carriers disappear through SE with a ~28 ps decay time, as seen below. On the other hand, it takes about 1.8 ps for the hot carriers to relax to the absorption edge, as shown in Figure 12. Compared to this time scale, the relaxation processes shown in Figure 16 are very slow. In fact, we see in Figure 16(d) a clamping of carrier relaxation near E_{em} at an average carrier density of 1×10^{17} cm^{-3}, which indicates that the localized states below E_{em} are able to accommodate most electron-hole pairs produced at this density. This may be evidence for an analogous mobility edge in the Mott-Anderson picture of localization[75] in view of hot carrier relaxation.
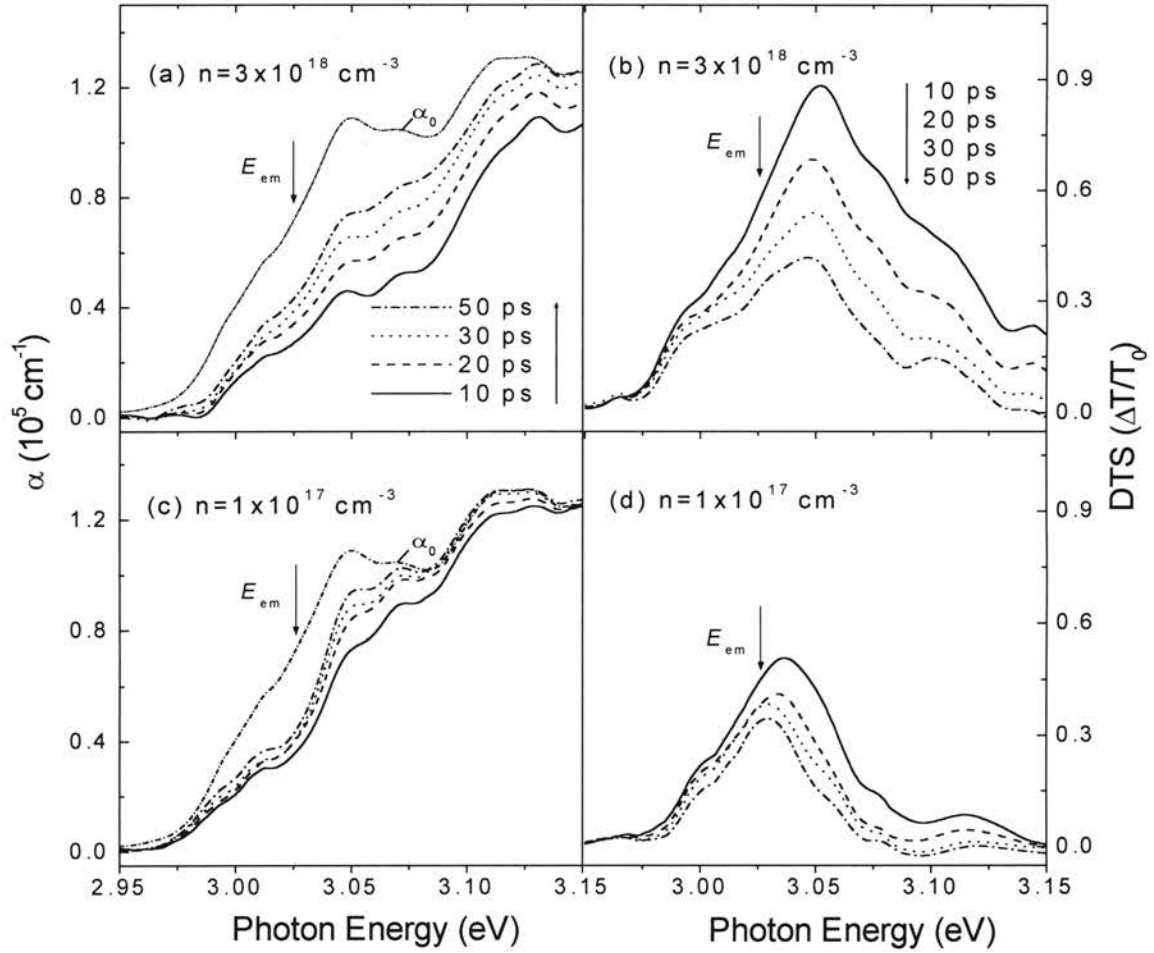
Figure 16. Absorption spectra and their corresponding differential transmission spectra near the band tail region of an $In_{0.18}Ga_{0.82}N$ active layer as a function of time delay for average carrier densities of (a, b) 3×10^{18} cm^{-3} and (c, d) 1×10^{17} cm^{-3}. The arrows indicate the effective mobility edge.

Figure 17 shows (a) the carrier density dependence of the time-integrated PL spectra and (b) their corresponding temporal responses. The effective PL lifetimes (τ_0 and τ_1) as determined by single (for average carrier densities 2×10^{16}, 1×10^{17}, and 5×10^{17} cm^{-3}) and double (for 2×10^{18} and 1×10^{19} cm^{-3}) exponential fittings are indicated in Figure 17(b). We observed SE above an average carrier density of 1×10^{18} cm^{-3}. Above the SE threshold density, the integrated PL intensity exhibits a super-linear growth as the carrier density increases. Compared to other III-V semiconductors, the observed SE threshold density is rather large, but this can be easily attributed to the large effective masses in this system, which make it difficult to reach population inversion.[76] According to Ref. 77, the filling of localized band-edge states is a prerequisite for achieving lasing in InGaN QW laser diodes. Because the SE lifetimes are less than our system resolution of ~60 ps, we obtained the decay constants using a de-convolution technique. The spontaneous emission peak position does not shift up to an average carrier density of 1×10^{17} cm^{-3}, but it has a significant blueshift at an average carrier density of 5×10^{17} cm^{-3} due to band filling of the localized states.
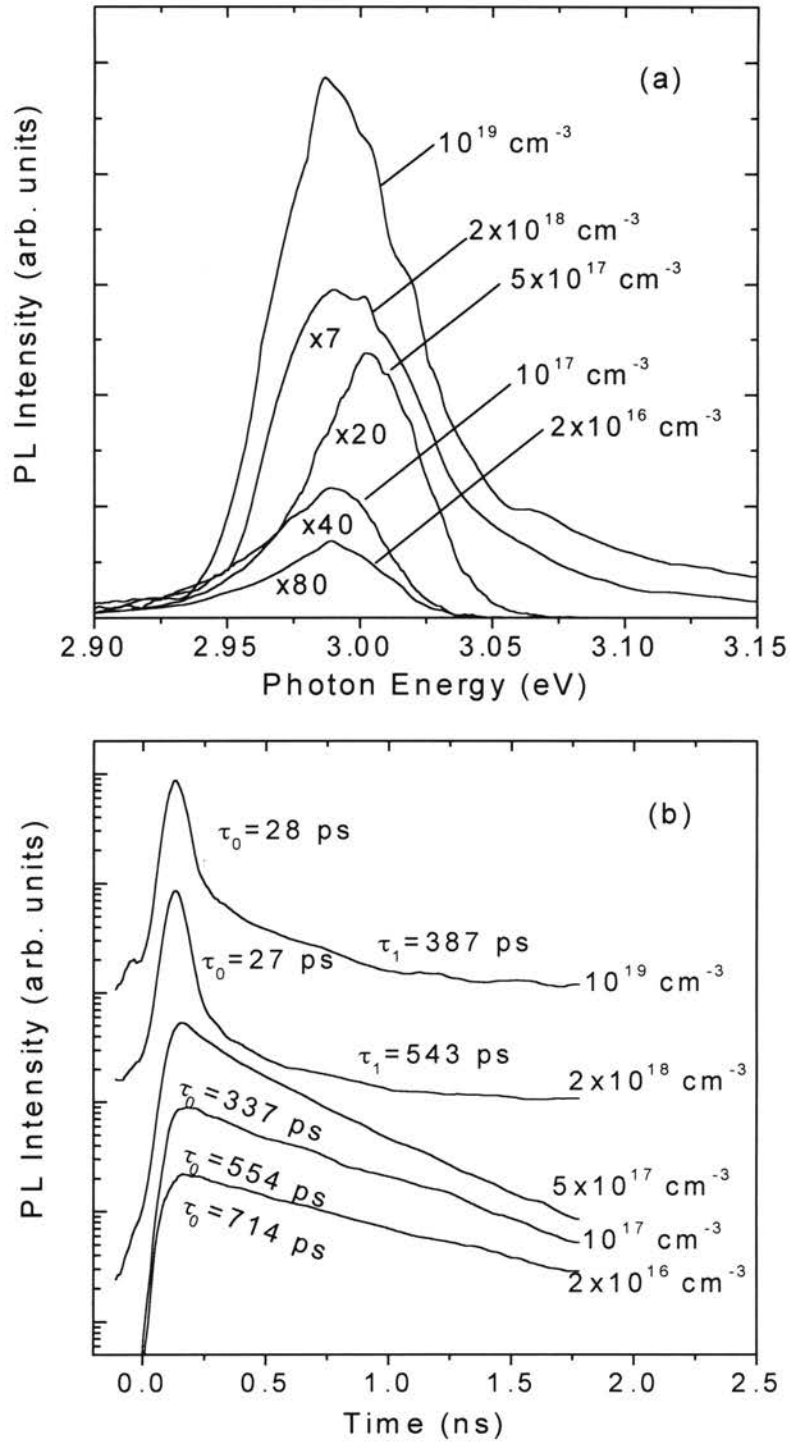
Figure 17. (a) Time-integrated PL spectra and (b) their time-resolved PL intensities at various carrier densities. The PL spectra at different carrier densities in Fig. 14(a) have been rescaled as indicated. The average threshold carrier density for stimulated emission was found to be 1×10^{18} cm^{-3}.

Spontaneous emission can be attributed to the well-known phenomenon of recombination of localized carriers (or excitons) in random potential wells induced by In compositional fluctuations,[62-65] since the strain-induced piezoelectric effect[78] in bulk InGaN is much smaller than in an InGaN/GaN MQW.[79] Figure 18 shows time-integrated four wave mixing on this sample at low excitation powers with the laser tuned to the absorption edge of 3.05 eV shown in Figure 15. We found that the signal at 10 K is not sensitive to detuning, which results from In compositional fluctuation, and it has a polarization dephasing time of 150 fs assuming a homogenous broadening similar to GaN.[48] This indicates that the absorption enhancement near the band edge is due to the excitonic ground state. The dephasing time of excitonic continuum states is expected to be much smaller. For instance, the dephasing time in pure GaAs was found to be less than 11 fs.[80] Therefore, piezoelectric fields should play only a minor role in this bulk material system. According to a simple model,[69] the density of states in the band tail quickly decreases with increasing activation energy, resulting in a lower density of final states for acoustic phonon-assisted relaxation or tunneling.[81,82] Thus, the average spatial separation between sites with deeper potential wells increases.[83] This causes a smaller tunneling probability per available site, and hence a longer effective PL lifetime at lower energy. For carriers with energies above E_{em}, the decay is most likely dominated by the rapid nonradiative transfer to lower localized states. As a result, the time-resolved spectrum shifts toward lower energy with increasing time delay, as shown in Figures 19(a) and (b).
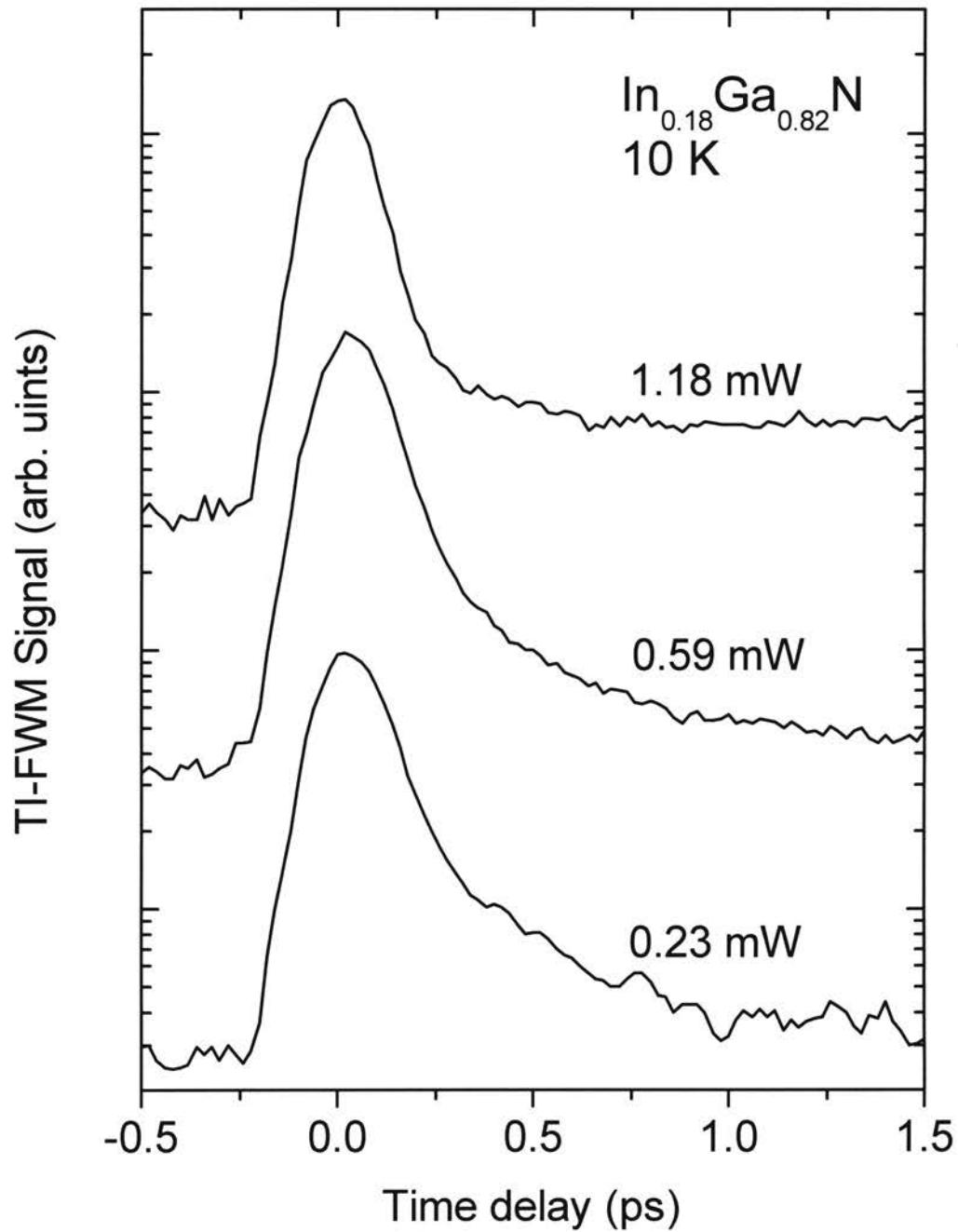
Figure 18. Time-integrated four-wave mixing signal in the reflection geometry near the absorption edge of the $In_{0.18}Ga_{0.82}N$ active layer for three excitation powers.
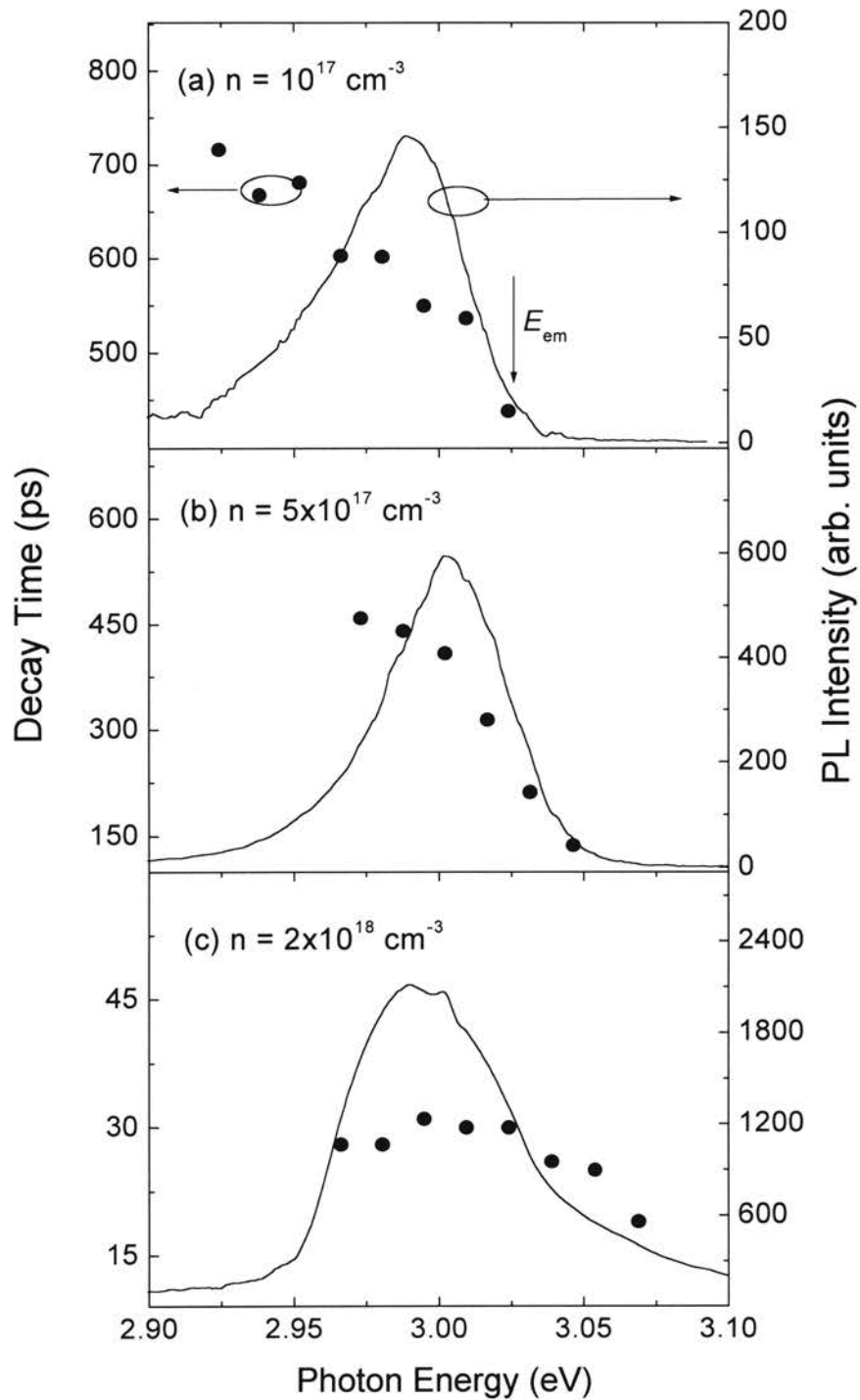
Figure 19. The effective recombination lifetime (determined by curve fitting to exponential decay) as a function of emission energy for average carrier densities of (a) 1×10^{17}, (b) 5×10^{17}, and (c) 2×10^{18} cm^{-3}. The solid lines are the corresponding time-integrated PL spectra. The arrow indicates the effective mobility edge.

The temporal PL traces for carrier densities above the SE threshold density show in Figure 17(b) two distinct decay constants: a short component for fast SE and a long component for subsequent spontaneous emission. Consistent with the occurrence of optical gain over a wide spectral region and the fast recovery from bleaching effects above the SE threshold density seen in PP spectroscopy, SE occurs from 2.95 eV to well above the absorption edge with decay constants of 27-28 ps, as shown in Figure 19(c). Figure 20 shows the detailed temporal evolution of the both (a) SE and (b) spontaneous emission. The top curve on each graph is taken at the peak of the TRPL decay curve. The maximum PL intensity in the TRPL decay curve at an average carrier density of 1×10^{19} cm^{-3} occurs about 28 ps faster than at an average carrier density of 5×10^{17} cm^{-3}. Considering our system resolution, the actual temporal evolution of the SE can be faster than the time delays in the Figure 20(a). If the spontaneous emission and SE originate from the same mechanism, they should have similar spectral shapes. However, the SE spectra at early time delays and the spontaneous emission spectra shown in Figure 20 are quite different, indicating that the SE does not result from recombination of carriers in localized states. The temporal behavior of the SE peak shown in Figure 20(a) can be well understood in terms of an EHP recombination from renormalized band-to-band transitions, where one expects such a blueshift as the number of carriers decreases through the SE with increasing time delay. This is consistent with our previous conclusion that the total density of localized states is less than 4×10^{17} cm^{-3}, and thus, SE must be dominated by carriers in extended states at these high densities.
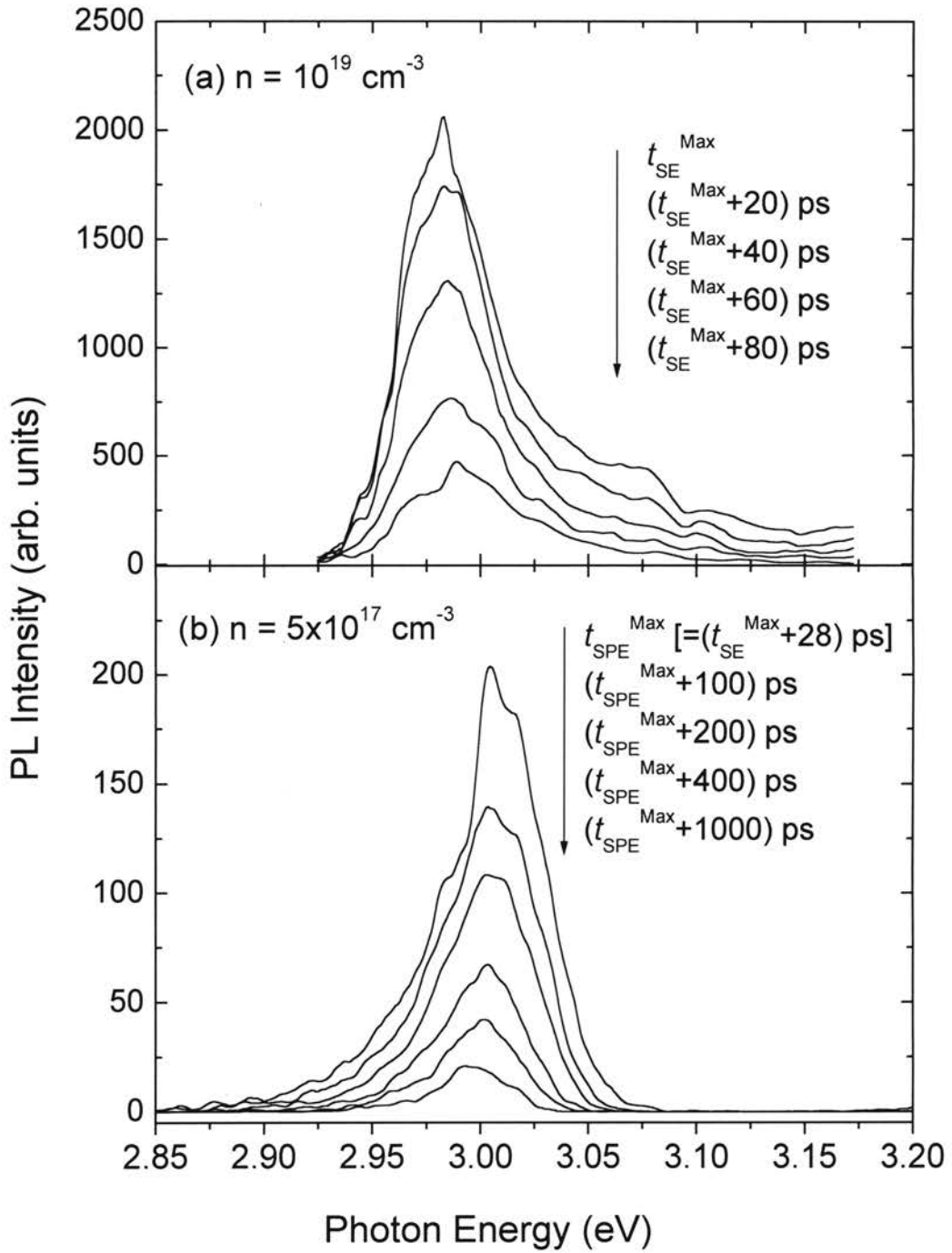
Figure 20. Temporal evolution of (a) stimulated emission at an average carrier density of 1×10^{19} cm^{-3} and (b) spontaneous emission at an average carrier density of 5×10^{17} cm^{-3}. The top curve on each graph is taken at the peak of the time-resolved PL decay curve.

We note that a previous study of SE as a function of excitation length for an InGaN/GaN MQW by nanosecond pulse excitation in the side pumping geometry was performed in Ref. 56, where the SE was shown to result from the recombination of carriers in localized states. Ref. 56 also shows that the SE threshold density quickly decreases and the peak position redshifts with increasing excitation length (from 500 to 2500 μm) due to reabsorption in the photoexcited region. Since the experimentally observed optical gain value of $\sim 10^4$ cm^{-1} shown in Figure 12(a) is not enough to allow SE in the sample growth direction, we consider the SE observed in this study to be in-plane traveling light which is scattered vertically by unintentionally formed crystal imperfections. The degree of localization in InGaN active layers depends very much on the mean In molar fraction and the growth conditions. For the same InGaN/GaN double heterostructure (DH) used in this study and an InGaN/GaN MQW sample which has the same InN fraction and similar Si doping concentration in the barriers, Ref. 25 shows that the band tail states are significantly larger in the InGaN/GaN MQW than in the InGaN/GaN DH. This is most likely due to the increased number of interfaces in the MQW compared to the DH, which leads to larger potential fluctuations. Therefore, both a small total density of localized states and a high SE threshold density resulted from a much small optical gain length by the crystal imperfections contribute to the fact that an EHP recombination from the renormalized band-to-band transition is responsible for SE in the InGaN/GaN DH discussed in this work.

Summary

In conclusion, we studied the hot carrier dynamics in an InGaN thin film photoexcited well above the band edge at 10 K under high carrier densities. At a carrier density of 3×10^{18} cm^{-3}, we clearly observed two successive LO-phonon emission processes via the Fröhlich interaction at 0 and 100 fs time delays. As the hot carriers relax, optical gain across the entire band tail and even above the absorption edge occurs at 2.5 ps time delay. This gain results in stimulated emission which has a ~28 ps decay time constant and a threshold density of 1×10^{18} cm^{-3}, which is larger than the total density of localized states induced by In compositional fluctuations. We attribute the stimulated emission to the recombination of an electron-hole plasma from renormalized band-to-band transitions.

CHAPTER VI

TIME-RESOLVED PHOTOLUMINESCENCE OF InGaN/GaN MUTIPLE
QUANTUM WELL STRUCTURES: EFFECT OF Si DOPING
IN THE BARRIERS

The carrier recombination dynamics in a series of $In_xGa_{1-x}N$/GaN multiple quantum wells, nominally identical apart from different Si doping concentrations in the GaN barriers, was studied by time resolved photoluminescence (PL) with excitation densities ranging from 220 nJ/cm^2 to 28 $\mu J/cm^2$ at 10 K and 300 K. At early time delays and with excitation densities greater than 5 $\mu J/cm^2$, at which the strain-induced piezoelectric field is screened by both photogenerated carriers and electrons from the GaN barriers, we observe a strong InGaN PL peak initially located 60 meV below the absorption edge and well above an effective mobility edge. This peak decays quickly with an effective lifetime less than 70 ps and disappears into the extended states while it gradually redshifts. The amount of this PL peak redshift decreases with increasing Si doping in the GaN barriers, suggesting that the peak is due to radiative recombination of free excitons in the screened piezoelectric field.

Motivation

Recent progress in the fabrication of InGaN/GaN multiple quantum well (MQW) devices has led to the blue laser diode with a lifetime of more than 10,000 hours under continuous wave operation at room temperature.[46] One characteristic property of this

material system is a large Stokes shift between the absorption edge and the photoluminescence (PL) emission. This large Stokes shift has been attributed to (i) carrier localization due to potential fluctuations associated with the formation of In-rich areas or islands[62-65,70,84] and (ii) the presence of a strain-induced piezoelectric (PZ) field which leads to the quantum-confined Stark effect (QCSE).[78,79,85,86] It is of great interest to examine the electronic states and carrier recombination dynamics in samples free from the influence of the PZ effect. The PZ field can be screened out by both photogenerated carriers and extrinsic carriers in the InGaN active layer and/or the barriers. In the latter case, the extrinsic carriers originate from barrier impurity doping and move into the active layer to satisfy the requirement of a constant Fermi level across the layers. Compared to the case of impurity doping both in the well and the barriers, we expect a lower impurity-related PL emission in the barrier-only case. While the dependence of the optical, electrical, and structural properties of strained InGaN/GaN MQW structures on Si doping concentration has been extensively studied,[87-92] to the best of our knowledge, little information is known about the intrinsic excitonic recombination dynamics.

In this chapter, a set of $In_{0.18}Ga_{0.82}N$/GaN MQW structures with Si doping concentrations in the range of $1\times10^{17} - 3\times10^{19}$ cm^{-3} in the GaN carriers has been studied by means of PL, PL excitation (PLE), and time-resolved PL (TRPL) to examine in detail the effect of Si doping on the optical properties. Special attention is paid to the recombination of free excitons in the InGaN active layers which is control ed by the screening of the PZ field.

Samples and experimental setup

The $In_{0.18}Ga_{0.82}N$/GaN MQW samples used in this work were grown on c-plane sapphire substrates by metalorganic chemical vapor deposition (MOCVD). A set of samples, nominally identical apart from deliberate variations in the Si doping concentration (n_{Si}), were grown specifically to study the influence of Si doping in the GaN barriers. The samples consist of a 1.8 μm thick GaN base layer and a 12 period

MQW region with 3 nm thick InGaN wells and 4.5 nm thick GaN barriers, followed by a $Al_{0.07}Ga_{0.93}N$ capping layer. A detailed description of the growth conditions has been published elsewhere.[93] The Si doping concentrations, which were obtained from secondary-ion mass spectroscopy and Hall measurements, are 1×10^{17}, 2×10^{18}, and 3×10^{19} cm^{-3} for the different samples studied. A nominally undoped $In_{0.18}Ga_{0.82}N$ epilayer sample used for comparison was grown by MOCVD at 800 °C. The structure consists of a 1.8 μm GaN layer on c-plane sapphire, a 50 nm thick GaN:Si ($n_{Si} \sim 10^{18}$ cm^{-3}) layer, followed by the 0.1 μm InGaN epilayer, and a 50 nm GaN:Si ($n_{Si} \sim 10^{19}$ cm^{-3}) layer. To evaluate the interface quality and structural parameters, the samples were analyzed with 4-crystal high resolution x-ray diffraction (HRXRD) using Cu $K\alpha_1$ radiation. The average InN molar fraction was measured by HRXRD, assuming Vegard's law. The angular distances between the satellite superlattice diffraction peaks and the GaN (0002) reflections were obtained by $\omega-2\theta$ scans. The spectra clearly showed higher-order satellite peaks, indicating high interface quality and good layer uniformity. The details of this x-ray analysis were reported elsewhere.[94]

The PL and PLE experiments were performed using quasi-monochromatic light from a xenon lamp dispersed by a 0.5 m monochromator. TRPL spectroscopy was carried out in the surface emission geometry with a 1 kHz tunable femtosecond pulsed laser system for sample excitation and a streak camera for detection. The pulse duration time and output wavelength from the laser system were 355 fs (full width at half maximum) and 371 nm (3.342 eV), respectively. This allowed direct excitation of the InGaN QWs at 10 K and 300 K. The pump spot size was 150 μm in diameter and the overall time resolution for TRPL measurements was about 60 ps.

Results and discussion

Figure 21 shows 10 K PL and PLE spectra of the main InGaN-related emission. The PLE detection energy was set at the main PL peak energy. For the nominally undoped (1×10^{17} cm^{-3}) sample, a large Stokes shift of 360 meV with respect to the band

70

edge measured by PLE is observed. This Stokes shift decreases with increasing density of electrons from the Si donors in the GaN barriers and is found to be 250 meV for the heavily doped (3×10^{19} cm^{-3}) sample, in which a large screening of the PZ field is expected by the electrons even at low temperature. This indicates that the large Stokes shifts are mainly due to large potential variations, which result from In composition fluctuations, strain fluctuations, interface roughness, crystal dislocations, and other defects. The HRXRD measurements for these InGaN/GaN MQWs show that the Si doping in the GaN barriers significantly improves the structural and interface quality, although it does not change the overall strain state (i.e., it does not cause a relaxation of the lattice-mismatch induced strain).[94] Consistently, the reduced Stokes shift with increasing doping concentration results mainly from the band-filling of localized states and better interface quality. The band edge of an InGaN/GaN MQW with Si doping in the GaN barriers is determined by a competition between the screening of the QCSE due to electrons from the GaN barriers and the 2-dimensional (2D) band gap renormalization (BGR) caused by the same electrons. Compared to the undoped MQW, the band edge of the heavily doped MQW is blueshifted by ~20 meV, indicating that the reduction of the QCSE is slightly larger than the BGR at $n_{Si} = 3 \times 10^{19}$ cm^{-3}.
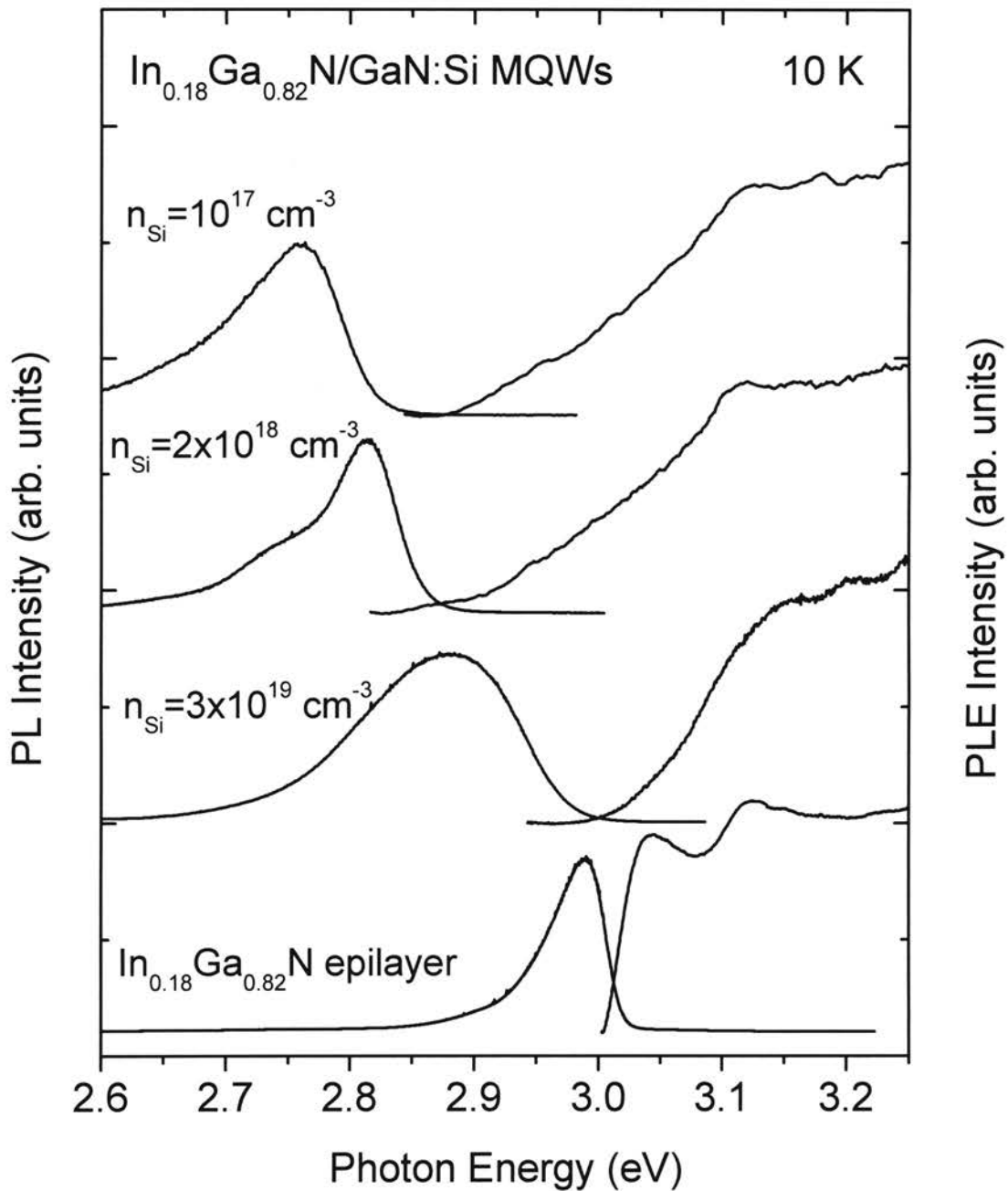
Figure 21. PL and PLE spectra of a series of $In_{0.18}Ga_{0.82}N$/GaN MQWs and an $In_{0.18}Ga_{0.82}N$ epilayer at 10 K. The Si doping concentration in the GaN barriers of the MQWs ranged from 1×10^{17} to 3×10^{19} cm^{-3}. The Stokes shift of the PL peak with respect to the PLE band edge is seen to decrease with increasing Si doping concentration.

Neglecting the PZ field, alloy potential fluctuations, and spontaneous polarization we estimated the confinement energy levels in the $In_{0.18}Ga_{0.82}N$ QWs by a finite potential well model. The electron and hole effective masses for the $In_{0.18}Ga_{0.82}N$ QWs are 0.2 m_e and 0.75 m_e, respectively, as estimated by a linear interpolation between the effective masses of 0.22 m_e and 0.8 m_e for GaN,[95,96] and 0.12 m_e and 0.5 m_e for InN.[97] With a band gap energy difference of 450 meV between the GaN barrier (3.5 eV)[6] and the $In_{0.18}Ga_{0.82}N$ epilayer (3.05 eV in Figure 21) at 10 K and a band-offset ratio of 3 : 7 for the conduction and valence bands (measured by a x-ray photoemission spectroscopy on the wurtzite crystal structure),[98] only the lowest confinement level ($n = 1$) exists in the conduction band for the 3 nm thick well layers. The transition energy between the $n = 1$ conduction and $n = 1$ A-valence band levels at 10 K is estimated to be 3.14 eV, which is the same as the PLE band edge of the heavily doped MQW sample and 20 meV larger than that of the undoped sample, as shown in Figure 21. Considering the lowest quantum-confined level redshift caused by the PZ field,[99] this energy difference is reasonable and agrees well with theoretically calculated results for the 3 nm thick InGaN/GaN.[79] However, we could not observe clear quantized state transitions in these MQW samples' photo-reflection measurements, most likely because of the large bandgap inhomogeneity.

Figure 22 shows (a) the optical excitation density dependence of the time-integrated PL spectra for the moderately doped MQW and (b) the spectral dependence of the PL decay time at an excitation density of 5.5 $\mu J/cm^2$ at 10 K. At excitation densities less than 5.5 $\mu J/cm^2$, the main PL peak blueshifts with increasing excitation density, mostly due to the band filling of localized states by the photogenerated carriers. For excitation densities higher than 5.5 $\mu J/cm^2$, this PL peak slightly redshifts and narrows. A large increase in the effective recombination lifetime with decreasing energy across the main PL peak is shown in Figure 22(b). This behavior can be well understood in terms of carrier (exciton) localization[68,81] where the carrier decay is by radiative recombination and also by nonradiative transfer to deeper localized states through acoustic phonon-assisted relaxation or tunneling. Assuming the radiative decay time is independent of energy and the density of localized states is proportional to $[exp(-E/E_0)]$ (E is the localization energy), we fit the experimental decay time data to $\tau^{-1}(E) =$

73

$\tau_{rad}^{-1}\{1+\exp[(E-E_{me})/E_0]\}$,[81] where τ_{rad} is the radiative lifetime, E_{me} is the energy analogous to a mobility edge,[82] and E_0 is the characteristic energy describing the energy dependence of the density of states. The best fit was obtained for $\tau_{rad}= 0.53$ ns, $E_{me} = 2.97$ eV, and $E_0 = 43$ meV. For the undoped and heavily doped MQWs at the same excitation density, we obtained τ_{rad} values of 1.95 and 0.57 ns, E_{me} values of 2.90 and 2.99 eV, and E_0 values of 35 and 45 meV, respectively. The blueshift of the mobility edge with increasing Si doping concentration is consistent with the reduction of the Stokes shift.
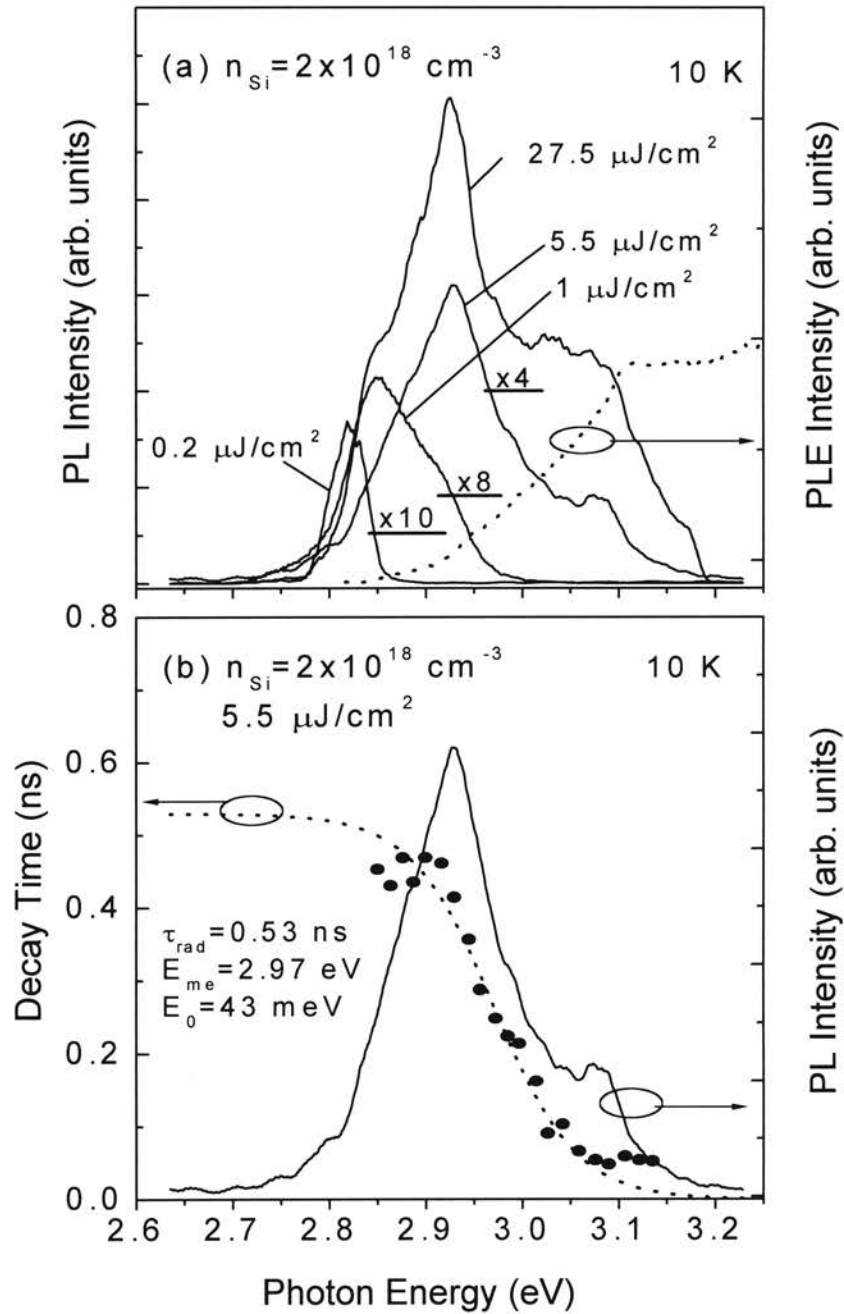
Figure 22. (a) 10 K time-integrated PL spectra at various excitation densities for an $In_{0.18}Ga_{0.82}N/GaN$ MQW with a Si doping concentration of 2×10^{18} cm^{-3} in the GaN barriers. The 10 K PLE spectrum is shown with a dashed line. (b) The effective recombination lifetime as a function of emission energy at an optical excitation density of 5.5 $\mu J/cm^2$ for the same sample at 10 K. The solid and dotted curves are the corresponding time-integrated PL spectrum and the best fit to the equation $\tau^{-1}(E) = \tau_{rad}^{-1}\{1 + \exp[(E - E_{me})/E_0]\}$, respectively.

We note that at higher excitation densities, the time-integrated spectra of Figure 22(a) contain two peaks. As the excitation density is increased from 5.5 μJ/cm^2 to 27.5 μJ/cm^2, the higher energy peak, which occurs 60 meV below the estimated lowest quantum-confined transition energy of 3.14 eV, rises much faster than the lower energy main PL peak and decays fast with a recombination lifetime of 70 ps, as shown in Figure 22(b). At early time delays for the three different Si doping concentrations in the GaN barriers, the temporal evolution of this high energy PL peak at an excitation density of 27.5 μJ/cm^2 is shown in Figure 23. The second curve from the bottom on the each graph is taken at the peak of the TRPL decay curve. The bottom curve is at the time delay which has an intensity 1/e times the peak intensity. For the heavily and moderately doped MQWs, the high energy peak initially occurs at 3.08 eV, and then redshifts 6 and 16 meV, respectively, by the time the TRPL decay curve reaches its maximum intensity. On the other hand, for the undoped MQW, the high energy peak initially occurs at 3.04 eV, and then redshifts 37 meV by the time the TRPL reaches maximum intensity. For all three MQWs, the high energy peak does not gradually redshift to the main PL peak, which is located below the mobility edge. Rather, this high energy peak disappears into the extended states, leaving only a shoulder on the main PL peak, as shown in the bottom curve on each graph in Figure 23. This behavior indicates that the high energy peak is related to radiative recombination of an intrinsic bound state controlled by the QCSE.
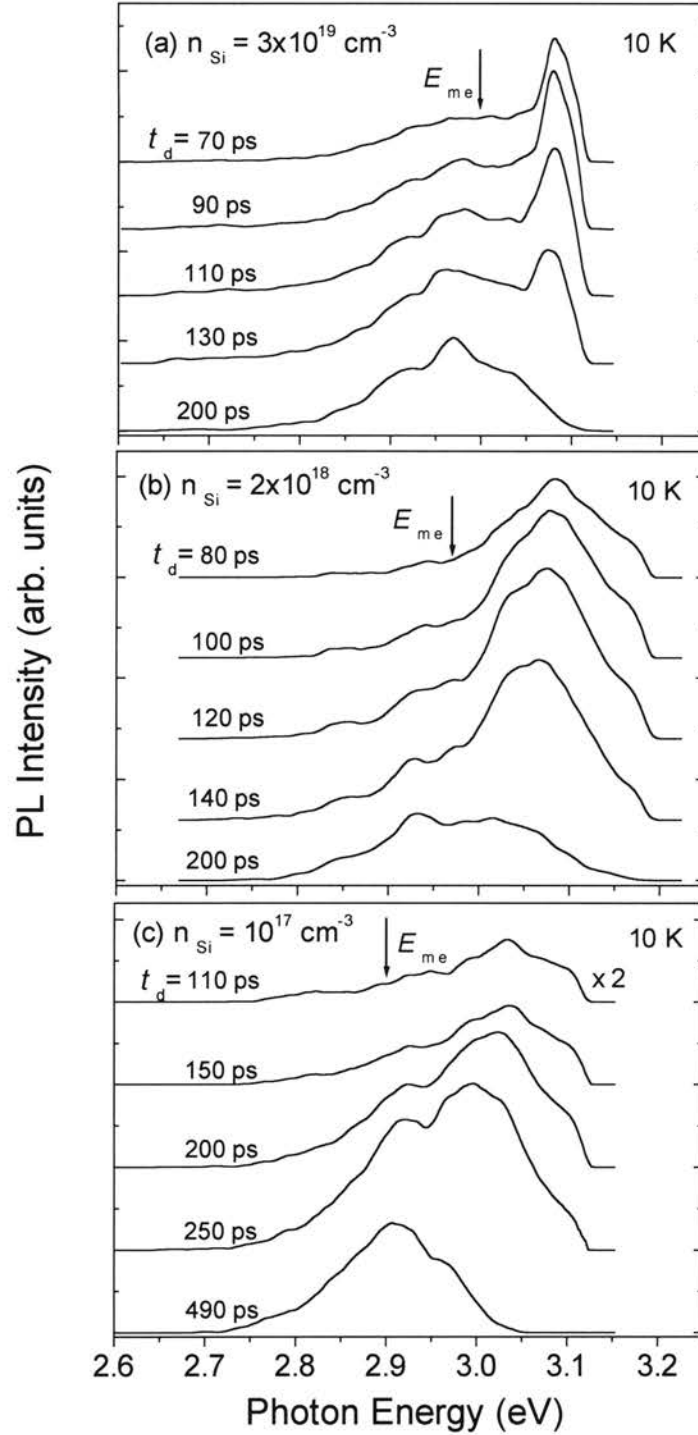
Figure 23. Time-resolved PL spectra of $In_{0.18}Ga_{0.82}N/GaN$ MQWs with GaN barrier Si doping concentrations of (a) 3×10^{19}, (b) 2×10^{18}, and (c) 1×10^{17} cm^{-3} at an excitation density of 27.5 $\mu J/cm^2$ and 10 K, showing the screening of the piezoelectric field by electrons from Si donors in the GaN barrier and by photogenerated carriers. The arrows indicate the effective mobility edge for each sample. The PL curves are displaced vertically for clarity.

This high energy peak is attributed to the recombination of the $n = 1$ A and B excitons, which are related to the $\Gamma^V_9 - \Gamma^C_7$ and Γ^V_7 (upper band) $- \Gamma^C_7$ interband transitions in the InGaN layer, respectively. The large strain-induced PZ field perpendicular to the QW layers (~1.2 MV/cm for a similar undoped sample, according to Ref. 100) is much larger than the classical exciton ionization field of 6.5×10^4 V/cm (= E_B/ea_B, where E_B is the zero-field exciton binding energy of 22 meV and a_B is the excitonic Bohr radius of 3.4 nm in GaN[15]). Therefore, the PZ field separates the electron-hole pairs and drastically reduces their overlap integral at low carrier densities. The average areal carrier density at an excitation power density of 27.5 μJ/cm^2 is estimated to be 1.4×10^{12} cm^{-2} [7×10^{18} cm^{-3} in 3D]. This value is below the Mott density in GaN, which is given in the first approximation by $n_M = 1/\pi(a_B^{2D})^2 = 1.1 \times 10^{13}$ cm^{-2}, where $a_B^{2D}(= a_B/2)$ is the 2D Bohr radius of the exciton. Immediately after excitation, a large number of photogenerated excitons and the electrons from the GaN barriers screen the PZ field. As radiative recombination proceeds, the screening effect is reduced and the transition energies as well as the oscillator strength of excitons are lowered. When the field ionization is dominant over the screening effect, the excitons cannot exist any longer. Thus, the temporal behavior of the high energy PL peak shown in Figure 23 may be understood as QCSE-controlled excitonic recombination. Previously, an electric field applied perpendicular to the plane of a GaAs/AlGaAs QW sample was shown to redshift the excitonic absorption peak by up to 2.5 times the zero-field binding energy. This redshift was observed for an applied field strength of 50 times the ionization field – the maximum field at which the excitons could still be resolved.[99] Compared to the exciton peak position in the moderately and heavily doped MQWs, the exciton peak in the undoped MQW is redshifted by 40 meV. With an estimated carrier density of 7×10^{18} cm^{-3}, the PZ field still exists in the undoped sample and causes a redshift of its excitonic transition. It has been reported that the exciton binding energy in GaAs/AlGaAs QWs increases with decreasing well thickness and is only about 2 times the 3D value when the well thickness is the same as the 3D Bohr radius,[101,102] since the InGaN/GaN MQW samples studied here have a 3 nm well thickness, which is less than the GaN exciton

78

Bohr radius, an exciton binding energy of 60 meV in the well at zero PZ field is reasonable for our InGaN/GaN MQWs.

Although the temporal behavior of the excitonic PL peak can be well explained in terms of the PZ field-induced QCSE, the time-integrated PL of InGaN/GaN MQWs is quite different from that of GaAs/A1GaAs MQWs. Since the band tail states are much larger in an InGaN ternary alloy than in pure GaAs, the excitons in InGaN/GaN QWs nonradiatively transfer to the deeper localized states. As seen in Figure 22(a), even at an excitation density of 27.5 $\mu J/cm^2$, most of the photoexcited carriers radiatively recombine from deep localized states with a transition energy of 2.92 eV instead of from the exciton levels with a transition energy of ~3.08 eV. The much shorter effective lifetime of the excitonic transition shows that the exciton recombination lifetime of 70 ps is dominated by a short non-radiative component.

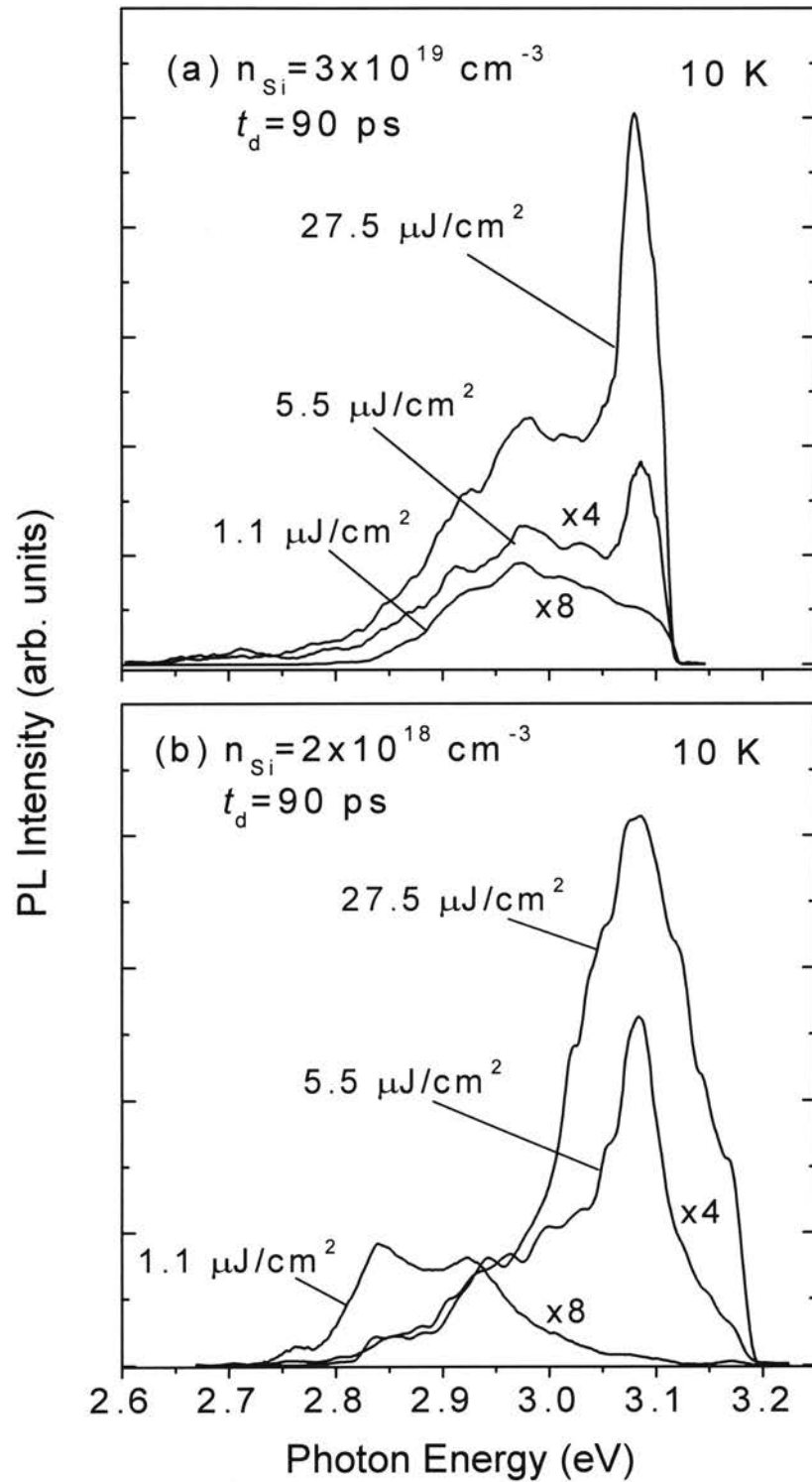**Figure 24.** PL spectra at a time delay of t_d = 90 ps for the In$_{0.18}$Ga$_{0.82}$N/GaN MQWs with Si doping concentrations of (a) 3×10^{19} and (b) 2×10^{18} cm^{-3} in the GaN barriers at the indicated optical excitation densities and at 10 K.

The excitation power density dependence of the PL spectra for the (a) heavily and (b) moderately doped samples at 10 K and 90 ps time delay is shown in Figure 24. With decreasing excitation density, a rapid reduction in the excitonic transition intensity is observed in both cases as a result of field ionization. At the lowest excitation density of 1.1 μJ/cm^2 in Figure 24(a) for the heavily doped sample, we cannot see an appreciable PL peak from excitonic recombination. Thus, the InGaN carrier density is too low at this excitation density to screen the PZ field, which significantly reduces the oscillator strength of excitons. This indicates that most of the electrons remain trapped at the GaN:Si donor sites with only a small fraction migrating into the InGaN active layer at 10 K, even for a Si doping concentration of 3×10^{19} cm^{-3} in the GaN barriers. The excitonic PL peak linewidth at an excitation density of 27.5 μJ/cm^2 in Figure 23(b) is much broader than in Figure 23(a). At this excitation density in both samples, we expect the PZ field to be screened out by the photogenerated carriers and the electrons from the GaN barriers. The maximum luminescence intensity and the lowest stimulated emission threshold by nanosecond pulse excitation in the side pumping geometry were observed for the moderately doped sample, which means it possesses the highest quantum efficiency among the three samples studied here.[65] Thus, at the same excitation density, the broader exciton PL linewidth in the moderately doped sample is mainly due to the substantially larger number of photo-generated electron-hole pairs. The broadening of the exciton PL peak in Figure 24(b) is also ascribed to the larger alloy and layer thickness fluctuations in the moderately doped MQW than the heavily doped one, which is consistent with HRXRD measurements for these MQWs.[94]

Figure 25 shows the temporal response of the PL intensities with the indicated effective lifetimes which were determined by single (for an excitation density of 1.1 μJ/cm^2) and double (for 5.5 and 27.5 μJ/cm^2) exponential fittings for the (a) moderately and (b) undoped InGaN/GaN MQWs. For the 5.5 and 27.5 μJ/cm^2 excitation densities, the first decay component results from fast exciton recombination, while the second component corresponds to localized carrier recombination which results in the main PL peak. Compared to Figure 25(a), the longer effective exciton lifetimes in Figure 25(b) result from a reduction in oscillator strength caused by the PZ effect, as shown in Figure

23. The undoped MQW has a much longer localized carrier lifetime than the moderately doped MQW. This can be attributed to less potential fluctuations and a smaller density of electrons from the Si donors in the GaN barriers.
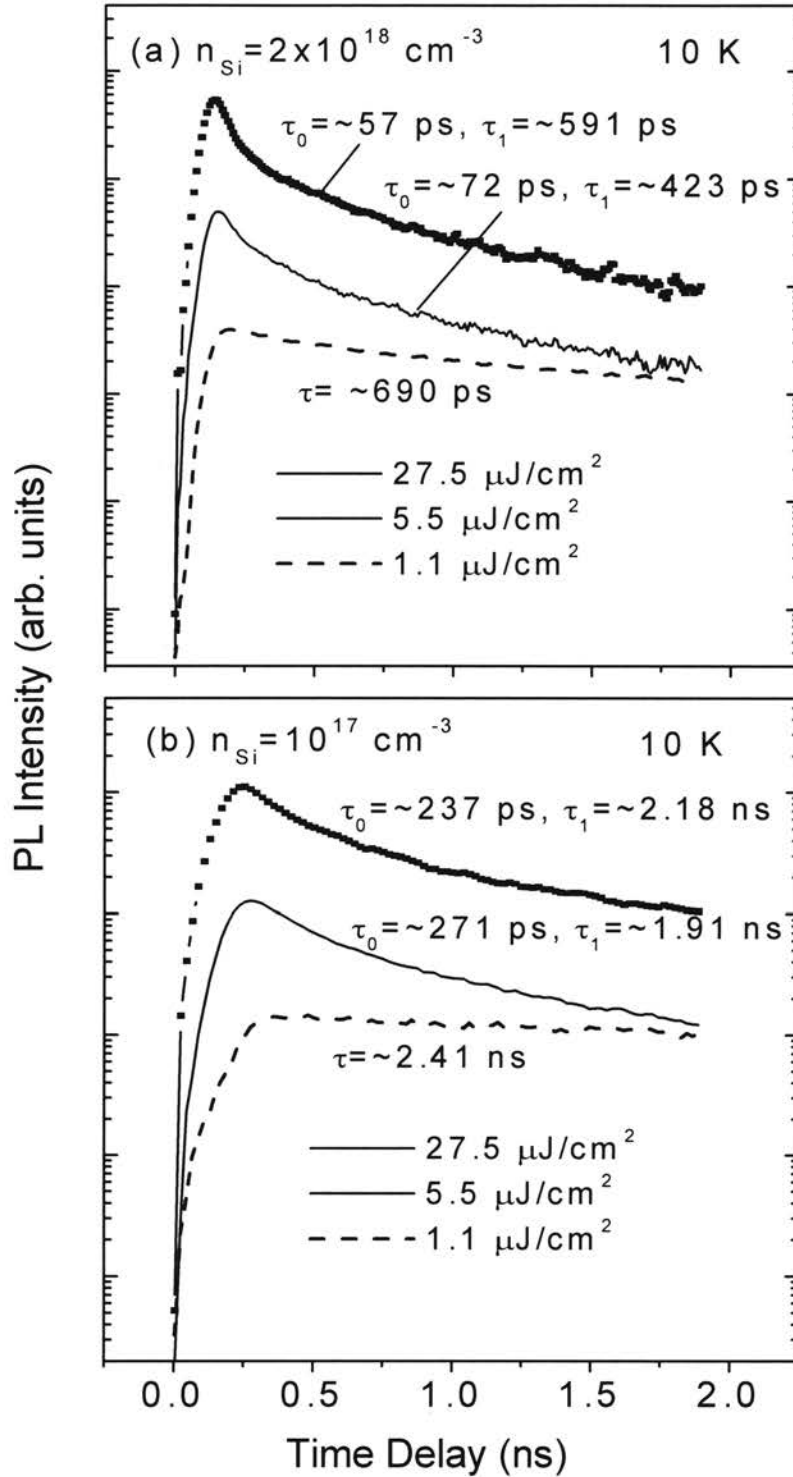
Figure 25. Time-resolved PL intensities of In$_{0.18}$Ga$_{0.82}$N/GaN MQWs with Si doping concentrations of (a) 2×10^{18} and (b) 1×10^{17} cm^{-3} in the GaN barriers at the indicated excitation densities. The indicated effective recombination lifetimes were obtained by curve fitting to double (for excitation densities of 27.5 and 5.5 μJ/cm^2) and single (for 1.1 μJ/cm^2) exponential decays.

Because the Si shallow donor level has an ionization of energy of only 22 meV,[103] at room temperature (RT), a large number of thermally activated electrons in the GaN barriers migrate into the InGaN active layer to satisfy the requirement of a constant Fermi level across the layers, especially for the heavily doped MQWs. In the TRPL measurement of the heavily doped MQW at RT, we could not observe the pronounced excitonic PL peak shown in Figure 23(a), because strong screening by the migrated electrons would prohibit the formation of the excitons. We found that the optical properties of the samples studied here are not consistent with their structural quality. While better interface quality was shown with increasing Si doping in the barriers, the stimulated emission threshold density of the heavily doped MQW sample was 3 times larger than that of the undoped and moderately doped MQWs with nanosecond pulse excitations in the side pumping geometry at RT.

The exciton recombination behavior at RT and at an excitation density of 27.5 $\mu J/cm^2$ is shown in Figure 26 for the (a) moderately doped and (b) undoped MQWs, and is similar to the behavior at 10 K shown in Figures 26(b) and (c). By the same method used for 10 K, the lowest transition energy between the $n = 1$ conduction and $n = 1$ A-valence band levels at RT is estimated to be 3.07 eV, which is 40 meV larger than the exciton PL peak in Figure 26(a). The RT exciton PL peak intensity is relatively weaker than that at 10 K, at the same excitation density, most likely due to thermal dissociation.
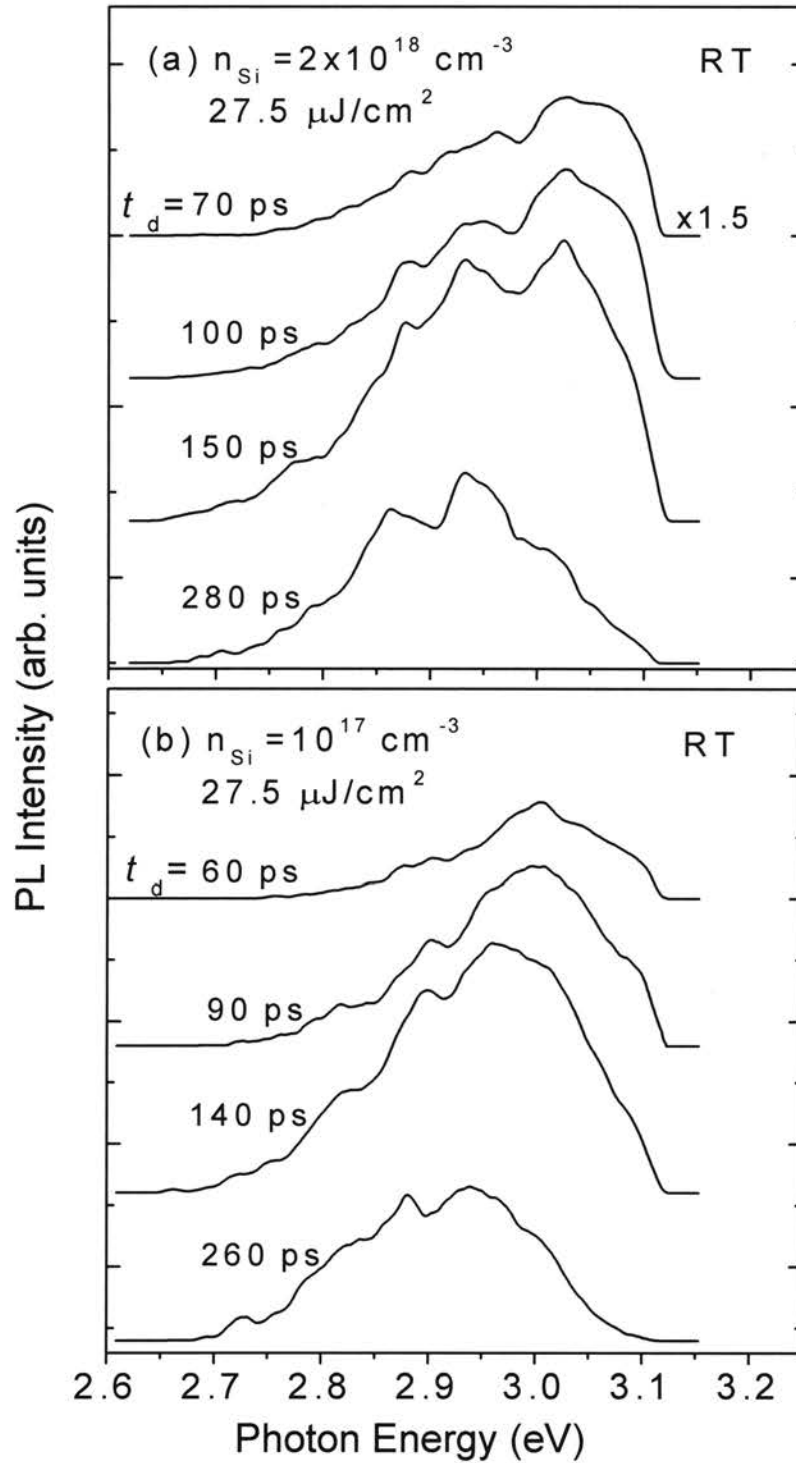
Figure 26. Time-resolved PL spectra of the $In_{0.18}Ga_{0.82}N/GaN$ MQWs with Si doping concentrations of (a) 2×10^{18} and (c) 1×10^{17} cm^{-3} in the GaN barriers at an optical excitation density of 27.5 μJ/cm^2 at room temperature. The PL curves are displaced vertically for clarity.

Summary

In conclusion, we systematically investigated the carrier recombination properties of a series of $In_{0.18}Ga_{0.82}N/GaN$:Si MQW structures with different Si doping concentrations in the GaN barriers, using TRPL at various excitation power densities. At excitation densities greater than 5 $\mu J/cm^2$, a strong excitonic PL peak in the extended states is observed for all three MQWs and its temporal evolution as a function of the GaN barrier Si doping is well described by a QCSE−controlled excitonic recombination mechanism. When the PZ field is almost screened by photogenerated carriers and by the electrons from the Si donors in the GaN barriers, the excitonic PL peak at 10 K is located 60 meV below the band edge determined by PLE measurements for the $In_{0.18}Ga_{0.82}N$ (3 nm)/GaN (4.5 nm) MQWs studied here.

CHAPTER VII

SUMMARY

The wide bandgap group III nitride semiconductors are technologically important materials due to their applications as green/blue light emitting devices and cw blue laser diodes. Although blue laser diodes based on the InGaN ternary alloy are commercially available, very little information exists on ultrafast carrier dynamics of these material systems. Understanding of various non-equilibrium, nonlinear, and transport properties of theses semiconductors becomes critically important in high speed optoelectronic device fabrication. This thesis serves to considerably extend the knowledge base of the optical properties of these semiconductors under strong optical excitation densities.

This thesis contains the first direct observation of the non-equilibrium carrier distributions during the pump duration and their relaxation in GaN photoexcited well above the bandgap. A spectral hole was initially peaked roughly at the excitation energy and gradually redshifted during the pump duration. We attributed the redshift of the hole to a combination of exciton effects and bandgap renormalization, which takes into account the non-equilibrium carrier distribution. Extremely slow energy relaxation and thermalization of the hot carriers in GaN were found at 10 K, due to blocking of the electron-LO phonon interaction and a large reduction in carrier-carrier scattering. It also includes a study of the excitonic optical Stark effect in GaN photoexcited well below the excitonic resonances with various pump and probe polarization configuration and provides comprehensive knowledge of it through a comparison with bulk GaAs and 2-dimensional GaAs/AlGaAs multiple quantum well structure cases.

The content of this thesis also include a study of the carrier dynamics in an InGaN thin film for carrier densities varying from 10^{17} to 10^{19} cm^{-3} photoexcited well above the

band edge, using femtosecond non-degenerate pump-probe spectroscopy and time-resolved photoluminescence measurements at 10 K. Through these measurements, we explored not only the early-stage thermalization processes of the hot carriers, but also the spectral and temporal properties of the recombination processes, both as functions of carrier density. Based on an experimentally observed optical gain value in pump-probe transmission measurement, we concluded that it may not possible to achieve vertical-cavity stimulated emission from optical pumping expect under extremely high excitation densities.

Finally, we addressed free excitonic recombination dynamics in a series of InGaN/GaN multiple quantum wells, nominally identical apart from different Si doping concentrations in the GaN barriers, using time-resolved photoluminescence with excitation densities ranging from 220 nJ/cm^2 to 28 μJ/cm^2 at 10 K and room temperature. At excitation densities greater than 5 μJ/cm^2, a strong photoluminescence peak in the extended states observed for all three multiple quantum wells and its temporal evolution as a function of the GaN barrier Si doping were well described by a quantum-confined Stark effect −controlled excitonic recombination mechanism. Although the temporal behavior of the excitonic photoluminescence peak can be well explained in terms of the piezoelectric field-induced quantum-confined Stark effect, the time-integrated photoluminescence of InGaN/GaN MQWs is quite different from that of GaAs/AlGaAs multiple quantum wells. Since the band tail states are much larger in an InGaN ternary alloy than in pure GaAs, the excitons in InGaN/GaN multiple quantum wells non-radiatively transfer to the deeper localized states.

BIBLIOGRAPHY

1. See, e.g., the articles in *Optical Nonlinear and Instabilities in Semiconductors*, edited by H. Haug (Academic, New York, 1988).

2. H. Haug and S. Schmitt-Rink, Prog. Quantum Electron. **9**, 3 (1984); J. Opt. Soc. Am. B **2**, 1135 (1985); S. Schmitt-Rink, C. Ell, and H. Haug, Phys. Rev. B **33**, 1183 (1986).

3. W. B. Joyce and R. W. Dixon, Appl. Phys. Lett. **31**, 354 (1977).

4. M. Lindberg and S. W. Koch, Phys. Rev. B **38**, 3342 (1988).

5. P. Y. Yu and M. Gardona, *Fundamental of Semiconductors* (Springer-Verlag, Berlin, 1996).

6. S. N. Mohammad and H. Morkoç, Prog. Quantum Electron. **20**, 361 (1996).

7. *Group III Semiconductor Compounds: Physics and Applications*, edited by B. Gil (Oxford Univ. Press, New York, 1998).

8. S. Sze, *Physics of Semiconductor Devices*, 2nd edition, (Wiley, New York, 1981).

9. J. J. Song and W. Shan, in *Group III Nitride semiconductor compounds: physics and applications*, edited by B. Gil, (Clarendon Press, Oxford, 1998).

10. J. Shah, *Ultrafast Spectroscopy of Semiconductors and Semiconductor Nanostructures* (Springer-Verlag, Berlin, 1996).

11. S. Hess, F. Walraet, R. A. Taylor, J. F. Ryan, B. Beaumont, and P. Gibart, Phys. Rev. B **58**, 15973 (1998).

12. Hong Ye, G. W. Wicks, and P. M. Fauchet, Appl. Phys. Lett. **74**, 711 (1999).

13. C. -K. Sun, Y. -L. Huang, S. Keller, U. K. Mishra, and S. P. DenBaars, Phys. Rev. B **59**, 13535 (1999).

14. F. Binet, J. Y. Duboz, J. Off, and F. Scholz, Phys. Rev. B **60**, 4715 (1999).

15. A. J. Fischer, W. Shan, J. J. Song, Y. C. Chang, R. Horning, and B. Goldenberg, Appl. Phys. Lett. **71**, 1981 (1997).

16. N. Peyghambarian, S. W. Koch, and A. Mysyrowicz, *Introduction to Semiconductor Optics* (Prentice-Hall, New Jersey, 1993), p. 384.

17. B. Fluegel, N. Peyghambarian, G. Olbright, M. Lindberg, S. W. Koch, M. Joffre, D. Hulin, A. Migus, and A. Antonetti, Phys. Rev. Lett. **59**, 2588 (1987).

18. J. L. Oudar, D. Hulin, A. Migus, A. Antonetti, and F. Alexandre, Phys. Rev. Lett. **55**, 2074 (1985).

19. W. Shan, S. Xu, B. D. Little, X. C. Xie, J. J. Song, G. E. Bulman, H. S. Hong, M. T. Leonard, and S. Krishnankutty, J. Appl. Phys. **82**, 3158 (1997).

20. C. Y. Tsai, C. H. Chen, T. L. Sung, C. Y. Tsai, and J. M. Rorison, J. Appl. Phys. **85**, 1475 (1999).

21. K. T. Tsen, R. P. Joshi, D. K. Ferry, A. Botchkarev, B. Sverdlov, A. Salvador, and H. Morkoç, Appl. Phys. Lett. **68,** 2990 (1996).

22. J. Shah, A. Pinczuk, A. C. Gossard, and W. Wiegmann, Phys. Rev. Lett. **54**, 2045 (1985).

23. P. Lugli, Solid State Electron. **31**, 667 (1988).

24. D. S. Kim and P. Y. Yu, Phys. Rev. B **43**, 4158 (1991).

25. J. Nunnenkamp, J. H. Collet, J. Klebniczki, J. Kuhl, and K. Ploog, Phys. Rev. B **43**, 14047 (1991).

26. J. -P. Foing, D. Hulin, M. Joffre, M. K. Jackson, J. -L. Oudar, C. Tanguy, and M. Combescot, Phys. Rev. Lett. **68**, 110 (1992).

27. C. Fürst, A. Leitenstorfer, A. Laubereau, and R. Zimmermann, Phys. Rev. Lett. **78**, 3733 (1997).

28. S. Hunsche, H. Heesel, A. Ewertz, H. Kurz, and J. H. Collet, Phys. Rev. B **48**, 17818 (1993).

29. G. B. Ren and P. Blood, Phys. Rev. B **60**, 16675 (1999).

30. T. Elsaesser, J. Shah, L. Rota, and P. Lugli, Phys. Rev. Lett. **66**, 1757 (1991).

31. B. D. Fluegel, A. Paul, K. Meissner, R. Binder, S. W. Koch, N. Peyghambarian, F. Sasaki, T. Mishina, and Y. Masumoto, Solid State Commun. **83**, 17 (1992).

32. A. Alexandrou, V. Berger, D. Hulin, and V. Thierry-Mieg, Phys. Status Sol. (b) **188**, 335 (1995).

33. T. Ando, A. B. Fowler, and F. Stern, Rev. Mod. Phys. **54**, 437 (1982).

34. R. Zimmermann, Phys. Stat. Sol. (b) **146**, 371 (1988).

35. A. Antonetti, D. Hulin, A. Migus, A. Mysyrowicz, and L. L. Chase, J. Opt. Soc. Am. B **2**, 1197 (1985).

36. D. Fröhlich, A. Nöthe, and K. Reimann, Phys. Rev. Lett. **55**, 1335 (1985).

37. A. Mysyrowicz, D. Hulin, A. Antonetti, A. Migus, W. T. Masselink, and H. Morkoç, Phys. Rev. Lett. **56**, 2748 (1986); A. Von Lehman, D. S. Chemla, J. E. Zucker, and J. P. Heritage, Opt. Lett. **11**, 609 (1986).

38. D. Fröhlich, R. Wille, W. Schlapp, and C. Weimann, Phys. Rev. Lett. **59**, 1748 (1987).

39. M. Joffre, D. Hulin, A. Migus, and M. Combescot, Phys. Rev. Lett. **62**, 74 (1989).

40. N. Peyghambarian, S. W. Koch, M. Lindberg, B. Fluegel, and M. Joffre, Phys. Rev. Lett. **62**, 1185 (1989).

41. W. H. Knox, D. S. Chemla, D. A. B. Miller, J. B. Stark, and S. Schmitt-Rink, Phys. Rev. Lett. **62**, 1189 (1989).

42. D. Hulin and M. Joffre, Phys. Rev. Lett. **65**, 3425 (1999).

43. M. Saba, F. Quochi, C. Ciuti, D. Martin, J.-L. Staehli, B. Deveaud, A. Mura, and C. Bongiovanni, Phys. Rev. B **62**, 16322 (2000).

44. S. Schmitt-Rink arid D. S. Chemla, Phys. Rev. Lett. **57**, 2752 (1986); S. Schmitt-Rink, D. S. Chemla, and H. Hang, Phys. Rev. B **37,** 941 (1988).

45. M. Combescot and R. Combescot, Phys. Rev. Lett. **61**, 117 (1988).

46. S. Nakamura, M. Senoh, S. Nagaliarna, N. Iwasa, T. Yamada, T. Matsushita, H. Kiyoku, Y. Sugimoto, T. Kozaki, H. Umemoto, M. Sano, and K. Chocho, Appl. Phys. Lett. **72**, 211 (1998).

47. W. Shan, B. D. Little, A. J. Fischer, J. J. Song, B. Goldenberg, W. C. Perry, M. D. Bremser, and R. F. Davis, Phys. Rev. B **54**, 16369 (1996); W. Shan, A. J. Fischer, S. J. Hwang, B. D. Little, R. J. Hauenstein, X. C. Xie, J. J. Song, D. S. Kim, B. Goldenberg, R. Horning, S. Krishnankutty, W. C. Perry, M. D. Bremser, and R. F. Davis, J. Appl. Phys. **83**, 455 (1998).

48. A. J. Fischer, W. Shan, G. H. Park, J. J. Song, D. S. Kim, D. S. Yee, R. Horning, and B. Goldenberg, Phys. Rev. B **56**, 1077 (1997).

49. C. K. Choi, Y. H. Kwon, J. S. Krasinski, C. H. Park, C. Setlur, J. J. Song, and Y. C. Chang, Phys. Rev. B **63**, 115315 (2001).

50. B. Gil and O. Briot, Phys. Rev. B **55**, 2530 (1997).

51. L. Schultheis, J. Kuhl, A. Honold, and C. W. Tu, Phys. Rev. Lett. **57**, 1635 (1986).

52. C. Klingshirn and H. Hang, Phys. Rep. **70**, 315 (1981).

53. Y. Kawakami, Z. C. Peng, Y. Narukawa, Sz. Fujita, Sg. Fujita, and S. Nakamura, Appl. Phys. Lett. **69**, 1414 (1996).

54. D. Kim, I. H. Libon, C. Voelkmann, Y, R. Shen, and V. Petrova-Koch, Phys. Rev. B **55**, 4907 (1997).

55. C.-K. Sun, J.-C. Liang, J.-C. Wang, F.-J. Kao, S. Keller, M. P. Mack, U. Mishra, and S. P. DenBaars, Appl. Phys. Lett. **76**, 439 (2000).

56. W. Schäfer, K.-H. Shuldt, and R. Binder, Phys. Stat. Sol. (b) **150**, 407 (1988).

57. R. Binder, S. W. Koch, M. Lindberg, W. Schäfer, and F. Jahnke, Phys. Rev. B **43**, 6520 (1991).

58. L. Chuang and C. S. Chang, Phys. Rev. B **54**, 2491 (1996).

59. S. Nakamura, MRS Internet J. Nitride Semicond. Res. **2**, 5 (1997).

60. W. R. L. Lambrecht, Solid State Electron. **41**, 195 (1997); T. Takeuchi, H. Takeuchi, S. Sota, H. Sakai, H. Amano, and I. Akasaki, Jpn. J. Appl. Phys. **36**, L177 (1997); C. Wetzel, T. Takeuchi, S. Yamaguchi, H. Katoh, H. Amano, and I. Akasaki, Appl. Phys. Lett. **73**, 1994 (1998).

61. Y. C. Chang and H. Yao, Phys. Rev. B **54**, 11517 (1996).

62. S. Chichibu, T. Azuhata, T. Soda, and S. Nakamura, Appl. Phys. Lett. **69**, 4188 (1996).

63. Y. Narukawa, Y. Kawakami, Sz. Fujita, Sg. Fujita, and S. Nakamura, Phys. Rev. B **55**, 1938 (1997).

64. M. Smith, G. D. Chen, J. Y. Lin, H. X. Jiang, M. A. Khan, and Q. Chen, Appl. Phys. Lett. **69**, 2837 (1996).

65. Y.-H. Cho, T. J. Schmidt, S. Bidnyk, G. H. Gainer, J. J. Song, S. Keller, U. K. Mishra, and S. P. DenBaars, Phys. Rev. B. **61**, 7571 (2000).

66. K. T. Tsen, D. K. Ferry, A. Botchkarev, B. Sverdlov, A. Salvador, and H. Morkoc, Appl. Phys. Lett. **72**, 2132 (1998).

67. V. Yu. Davydov, V. V. Emtsev, I. N. Goncharuk, A. N. Smirnov, V. D. Petrikov, V. V. Mamutin, V. A. Vekshin, S. V. Ivanov, M. B. Smirnov, and T. Inushirma, Appl. Phys. Lett. **75**, 3297 (1999).

68. C. K. Sun, F. Vallée, S. Keller, J. E. Bowers, and S. P. DenBaars, Appl. Phys. Lett **70**, 2004 (1997).

69. E. Cohen and M. D. Sturge, Phys. Rev. B **25**, 3828 (1982); S. Permogorov and A. Reznitsky, J. Lum. **52**, 201 (1992).

70. A. Satake, Y. Masumoto, T. Miyajima, T. Asatsuma, F. Nakamura, and M. Ikeda, Phys. Rev. B **57**, 2041 (1998).

71. T. Gong, P. M. Fauchet, J. F. Young, and P. J. Kelly, Phys. Rev. B **44**, 6542 (1991).

72. C. V. Shank, R. L. Fork, R. Yen, J. Shah, B. I. Greene, A. C. Gossard, and C. Weisbuch, Solid State Commun. **47**, 981 (1983).

73. Y. Kawakami, Y. Narukawa, K. Omae, S. Fujita, and S. Nakamura, Appl. Phys. Lett. **77**, 2151 (2000).

74. D. M. Bagnall and K. P. O'Donnell, Appl. Phys. Lett. **68**, 3197 (1996).

75. N. F. Mott and E. A. Davis, *Electronic Processes in Non-Crystalline Materials*, 2nd ed. (Oxford University, England, 1979).

76. W. Fang and S. L. Chuang, Appl. Phys. Lett. **67**, 751 (1995).

77. Y.-K. Song, M. Kuball, A. V. Nurmikko, G. E. Bulman, K. Doverspike, S. T. Sheppard, T. W. Weeks, and M. Leonard, Appl. Phys. Lett. **72**, 1418 (1998).

78. T. Takeuchi, S. Sota, M. Katsuragawa, M. Komori, H. Takeuchi, H. Amano, and I. Akasaki, Jpn. J. Appl. Phys. Part 2 **36**, L382 (1997).

79. E. Berkowicz, D. Gershoni, G. Bahir, E. Lakin, D. Shilo, E. Zolotoyabko, A. C. Abare, S. P. DenBaars, and L. A. Coldren, Phys. Rev. B **61**, 10994 (2000).

80. P. C. Becker, H. L. Fragnito, C. H. Brito Crutz, R. F. Fork, J. E. Cunningham, J. E. Henry, and C. V. Shank, Phys. Rev. Lett. **61**, 1647 (1988).

81. C. Gourdon and P. Lavallard, Phys. Stat. Sol. (b) **153**, 641 (1989).

82. M. Oueslati, C. Benoit à la Guillaume, and M. Zouaghi, Phys. Rev. B **37**, 3037 (1988).

83. J. A. Kash, A. Ron, E. Cohen, Phys. Rev. B **28**, 6147 (1983).

84. K. P. O'Donnell, R. W. Martin, and P. G. Middleton, Phys. Rev. Lett. **82**, 237 (1999).

85. S. F. Chichibu, A. C. Abare, N. S. Minsky, S. Keller, S. B. Fleischer, J. E. Bowers, E. Hu, U. K. Mishra, L. A. Coldren, and S. P. DenBaars, Appl. Phys. Lett. **73**, 2006 (1998).

86. A. Hangleiter, J. S. Im, H. Kolhmner, S. Heppel, J. Off, and F. Scholz, MRS Internet J. Nitride Semicond. Res. **3**, 15 (1998).

87. T. Deguchi, A. Shikanai, K. Toni, T. Sota, S. Chichibu, and S. Nakamura, Appl. Phys. Lett. **72**, 3329 (1998).

88. Chichibu, D. A. Cohen, M. P. Mack, A. C. Abare, P. Kozodoy, M. Minsky, S. B. Fleischer, S. Keller, J. E. Bowers, U. K. Mishra, L. A. Coldren, D. R. Clarke, and S. P. DenBaars, Appl. Phys. Lett. **73**, 496 (1998).

89. Y. Yamada, T. Taguchi, F. Sasaki, S. Kobayashi, and T. Tani, J. Crystal Growth **189/190**, 611 (1998).

90. Y.-H. Cho, J. J. Song, S. Keller, M. S. Minsky, E. Hu, U. K. Mishra, and S. P. DenBaars, Appl. Phys. Lett. **73**, 1128 (1998).

91. J. Dalfors, J. P. Bergman, P. O. Holtz, B. E. Sernelius, B. Monemar, H. Amano, and I. Akasaki, Appl. Phys. Lett. **74**, 3299 (1999).

92. T. Wang, H. Saeki, J. Bai, T. Shirahama, M. Lachab, S. Sakai, and P. Eliseev, Appl. Phys. Lett. **76**, 1737 (2000).

93. Keller, A. C. Abare, M. S. Minsky, X. H. Wu, M. P. Mack, J. S. Speck, E. Hu, L. A. Coldren, U. K. Mishra, and S. P. DenBaars, Mater. Sci. Forum **264-268**, 1157 (1998); B. P. Keller, S. Keller, D. Kapoinek, W. N. Jiang, X. -F. Wu, H. Masui, X. H. Wu, B. Heying, J. S. Speck, U. K. Mishra, and S. P. DenBaars, J. Electron. Mater. **24**, 1707 (1995).

94. Y.-H. Cho, F. Fedler, R. J. Hauenstein, G. H. Park, S. Keller, U. K. Mishra, and S. P. DenBaars, J. Appl. Phys. **85**, 3006 (1999).

95. A. M. Witowski, K. Pakula, J. M. Baranowski, M. L. Sadowski, and P. Wyder, Appl. Phys. Lett. **75**, 4154 (1999).

96. J. I. Pankove, S. Bloom, and G. Harbeke, RCA Rev. **36**, 163 (1975).

97. C. P. Foley and T. L. Tansley, Phys. Rev. B **33**, 1430 (1986).

98. G. Martin, A. Botchkarev, A. Rockott, and H. Morkoc, Appl. Phys. Lett. **68**, 2541 (1996).

99. D. A. B. Miller, D. S. Chemla, T. C. Damen, A. C. Gossard, W. Wiegmann, T. H. Wood, and C. A. Burrus, Phys. Rev. B. **32**, 1043 (1985).

100. T. Takeuchi, C. Wetzel, S. Yamaguchi, H. Sakai, H. Amano, I. Akasaki, Y. Kaneko, S. Nakagawa, Y. Yamaoka, and N. Yamada, Appl. Phys. Lett. **73**, 1691 (1998).

101. R. C. Miller, D. A. Kleinman, W. T. Tsang, and A. C. Gossard, Phys. Rev. B **24**, 1134 (1981).

102. G. Bastard, E. E. Mendez, L. L. Chang, and L. Esaki, Phys. Rev. B **26**, 1974 (1982).

103. W. Götz, N. M. Johnson, C. Chen, H. Liu, C. Kuo, and W. Imler, Appl. Phys. Lett. **68**, 3144 (1996).

APPENDIX

PUBLICATIONS

The following refereed scientific publications were generated from the material contained in this thesis:

- "Polarization dependence of the excitonic optical Stark effect in GaN," <u>C. K. Choi</u>, J. B. Lam, G. H. Gainer, S. K. Shee, J. S. Krasinski, J. J. Song, and Y. C. Chang, (submitted to Phys. Rev. B in June, 2001).

- "Time-resolved photoluminescence study of InGaN/GaN multiple quantum well structures: Effect of Si doping in the barriers," <u>C. K. Choi</u>, Y. H. Kwon, B. D. Little, J. J. Song, Y. C. Chang, S. Keller, U. K. Mishra, and S. P. DenBaars, (submitted to Phys. Rev. B on March 27, 2001).

- "Femtosecond pump-probe spectroscopy and time-resolved photoluminescence of an InGaN/GaN double heterostructure," <u>C. K. Choi</u>, B. D. Little, Y. H. Kwon, J. B. Lam, J. J. Song, Y. C. Chang, S. Keller, U. K. Mishra, and S. P. DenBaars, Phys. Rev. B **63**, 195302 (2001).

- "Ultrafast carrier dynamics in a highly excited GaN epilayer, " <u>C. K. Choi</u>, Y. H. Kwon, J. S. Krasinski, G. H. Park, G. Setlur, J. J. Song, and Y. C. Chang, Phys. Rev. B **63**, 115315 (2001).

∂

VITA

ChanKyung Choi

Candidate for the Degree of

Doctor of Philosophy

Thesis: ULTRAFAST CARRIER DYNAMICS IN HIGHLY EXCITED GAN
EPILAYER, INGAN/GAN DOUBLE HETEROSTRUCTURE, AND
INGAN/GAN MULTIPLE QUANTUM WELL STRUCTURES

Major Field: Physics

Biographical:

Personal Data: Born in Sacheon, Kyung-Nam, Republic of Korea, on November 1,
1968

Education: Received Bachelor of Science degree in Astronomy from Seoul National
University, Seoul, Korea, in February 1990; obtained a Master of Science
Degree in Physics from Seoul National University, Seoul, Korea, in February
1997. Completed the requirements for the Doctor of Philosophy Degree with
a major in Physics at Oklahoma State University in August 2001.

Professional Experience: Employed by Oklahoma State University, Center for Laser
and Photonics Research and Department of Physics as a graduate research
assistant, August 1997 to July 2001.

Professional Memberships: American Physical Society, SPIE-International Society
for Optical Engineering.